

AFRL-ML-WP-TR-2001-4177

**MATERIALS PROCESSING RESEARCH
AND DEVELOPMENT**

**Douglas R. Barker
Robert L. Goetz**

**UES, Inc.
4401 Dayton-Xenia Rd.
Dayton, OH 45432-1894**



NOVEMBER 2001

Final Report for 23 August 1996 – 23 January 2001

Approved for public release; distribution is unlimited.

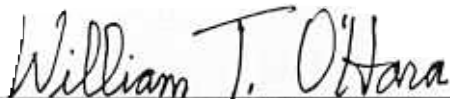
**MATERIALS AND MANUFACTURING DIRECTORATE
AIR FORCE RESEARCH LABORATORY
AIR FORCE MATERIEL COMMAND
WRIGHT-PATTERSON AIR FORCE BASE, OH 45433-7750**

NOTICE

WHEN GOVERNMENT DRAWINGS, SPECIFICATIONS, OR OTHER DATA ARE USED FOR ANY PURPOSE OTHER THAN IN CONNECTION WITH A DEFINITELY GOVERNMENT-RELATED PROCUREMENT, THE UNITED STATES GOVERNMENT INCURS NO RESPONSIBILITY OR ANY OBLIGATION WHATSOEVER. THE FACT THAT THE GOVERNMENT MAY HAVE FORMULATED OR IN ANY WAY SUPPLIED THE SAID DRAWINGS, SPECIFICATIONS, OR OTHER DATA, IS NOT TO BE REGARDED BY IMPLICATION OR OTHERWISE IN ANY MANNER CONSTRUED, AS LICENSING THE HOLDER OR ANY OTHER PERSON OR CORPORATION, OR AS CONVEYING ANY RIGHTS OR PERMISSION TO MANUFACTURE, USE, OR SELL ANY PATENTED INVENTION THAT MAY IN ANY WAY BE RELATED THERETO.

THIS REPORT IS RELEASABLE TO THE NATIONAL TECHNICAL INFORMATION SERVICE (NTIS). AT NTIS, IT WILL BE AVAILABLE TO THE GENERAL PUBLIC, INCLUDING FOREIGN NATIONS.

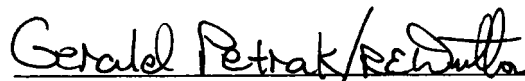
THIS TECHNICAL REPORT HAS BEEN REVIEWED AND IS APPROVED FOR PUBLICATION.



WILLIAM T. O'HARA
Metals Branch
Metals, Ceramics & NDE Division



ROLLIE E. DUTTON, Chief
Metals Branch
Metals, Ceramics & NDE Division



GERALD J. PETRAK, Asst Chief
Metals, Ceramics & NDE Division
Materials and Manufacturing Directorate

IF YOUR ADDRESS HAS CHANGED, IF YOU WISH TO BE REMOVED FROM OUR MAILING LIST, OR IF THE ADDRESSEE IS NO LONGER EMPLOYED BY YOUR ORGANIZATION, PLEASE NOTIFY, AFRL/MLLMP, WRIGHT-PATTERSON AFB, OH 45433-7750 TO HELP US MAINTAIN A CURRENT MAILING LIST.

COPIES OF THIS REPORT SHOULD NOT BE RETURNED UNLESS RETURN IS REQUIRED BY SECURITY CONSIDERATIONS, CONTRACTUAL OBLIGATIONS, OR NOTICE ON A SPECIFIC DOCUMENT.

REPORT DOCUMENTATION PAGE					Form Approved OMB No. 0704-0188	
The public reporting burden for this collection of information is estimated to average 1 hour per response, including the time for reviewing instructions, searching existing data sources, gathering and maintaining the data needed, and completing and reviewing the collection of information. Send comments regarding this burden estimate or any other aspect of this collection of information, including suggestions for reducing this burden, to Department of Defense, Washington Headquarters Services, Directorate for Information Operations and Reports (0704-0188), 1215 Jefferson Davis Highway, Suite 1204, Arlington, VA 22202-4302. Respondents should be aware that notwithstanding any other provision of law, no person shall be subject to any penalty for failing to comply with a collection of information if it does not display a currently valid OMB control number. PLEASE DO NOT RETURN YOUR FORM TO THE ABOVE ADDRESS.						
1. REPORT DATE (DD-MM-YY) November 2001		2. REPORT TYPE Final		3. DATES COVERED (From - To) 08/23/1996 – 01/23/2001		
4. TITLE AND SUBTITLE MATERIALS PROCESSING RESEARCH AND DEVELOPMENT				5a. CONTRACT NUMBER F33615-96-C-5251		
				5b. GRANT NUMBER		
				5c. PROGRAM ELEMENT NUMBER 62102F		
6. AUTHOR(S) Douglas R. Barker Robert L. Goetz				5d. PROJECT NUMBER 4347		
				5e. TASK NUMBER 53		
				5f. WORK UNIT NUMBER 06		
7. PERFORMING ORGANIZATION NAME(S) AND ADDRESS(ES) UES, Inc. 4401 Dayton-Xenia Rd. Dayton, OH 45432-1894				8. PERFORMING ORGANIZATION REPORT NUMBER		
9. SPONSORING/MONITORING AGENCY NAME(S) AND ADDRESS(ES) Materials and Manufacturing Directorate Air Force Research Laboratory Air Force Materiel Command Wright-Patterson AFB, OH 45433-7750				10. SPONSORING/MONITORING AGENCY ACRONYM(S) AFRL/MLLMP		
				11. SPONSORING/MONITORING AGENCY REPORT NUMBER(S) AFRL-ML-WP-TR-2001-4177		
12. DISTRIBUTION/AVAILABILITY STATEMENT Approved for public release; distribution is unlimited.						
13. SUPPLEMENTARY NOTES Report contains color.						
14. ABSTRACT <p>Research during the contract dealt with several areas related to the processing of advanced aerospace materials: fracture and cavitation, microstructure evolution, texture evolution, and constitutive equations. Materials studied were α_2, γ, and near γ TiAl's, an orthorhombic TiAl alloy, Ti-6Al-4V, 2024 Al, a nanophase Al alloy, and a tungsten heavy alloy. Tensile and uniaxial compression tests were used, as was the ring test for interface friction and heat transfer tests. In addition to conventional processes, emerging processes such as ECAE and friction stir welding were used and modeled. Finite element modeling was employed to predict states of stress, strain, strain rate, and temperature as well as material flow and loads. New models were developed for crack and cavitation prediction. Microstructure evolution was modeled using analytical methods, and a CA model was developed for heterogeneous static and dynamic recrystallization.</p> <p>AFRL resources were united with private industry, DoD contractors, and other Federal facilities using CTeC, MAI, and various CRADA tasks involving 13 DoD and DOE contractors. MPL technicians conducted 3072 processing operations and tests, and designed, fabricated or installed the following tooling or equipment; salt pot, ECAE tooling, rapid heat treat stand, 1000-ton load cell, DS unit, 55 kip and 200 kip MTS tooling, spin mold casting device, and mothballed the isothermal chamber.</p>						
15. SUBJECT TERMS processing, metals, nickel alloys, titanium alloys						
16. SECURITY CLASSIFICATION OF:			17. LIMITATION OF ABSTRACT: SAR	18. NUMBER OF PAGES 158	19a. NAME OF RESPONSIBLE PERSON (Monitor) William O'Hara	
a. REPORT Unclassified	b. ABSTRACT Unclassified	c. THIS PAGE Unclassified			19b. TELEPHONE NUMBER (Include Area Code) (937) 255-1995	

Table of Contents

<u>Section</u>	<u>Page</u>
LIST OF FIGURES	VI
LIST OF TABLES	VII
FOREWORD.....	VIII
1 INTRODUCTION.....	1
2 PUBLISHED RESEARCH	2
2.1 PUBLISHED RESEARCH ON INTERMETALLICS	2
2.1.1 <i>A Criterion for Intergranular Fracture During Hot Working of a Near Gamma Titanium Aluminide Alloy.....</i>	<i>2</i>
2.1.2 <i>Analysis of Grain Growth in a Two-Phase Gamma Titanium Aluminide Alloy.....</i>	<i>2</i>
2.1.3 <i>Modeling of Cracking and Cavitation During Hot Working of Gamma Titanium Aluminides.....</i>	<i>3</i>
2.1.4 <i>Phase Stability in a Ti-45.5Al-2Nb-2Cr Alloy.....</i>	<i>3</i>
2.1.5 <i>Plastic Flow and Microstructure Evolution during Hot Deformation of a Gamma Titanium Aluminide Alloy.....</i>	<i>4</i>
2.1.6 <i>Intergranular Fracture of Gamma Titanium Aluminides under Hot Working Conditions.</i>	<i>4</i>
2.1.7 <i>Phase Transformation Behavior of Gamma Titanium Aluminide Alloys During Supertransus Heat Treatment.....</i>	<i>4</i>
2.1.8 <i>The Knoop-Hardness Yield Locus of an Orthorhombic Titanium Aluminide Alloy.....</i>	<i>5</i>
2.1.9 <i>Dynamic Globularization of Lamellar Structures in a Near Gamma Titanium Aluminide Alloy.....</i>	<i>5</i>
2.1.10 <i>Microstructures and Tensile Properties of Ti-45.5Al-2Nb-2Cr Rolled Sheets.....</i>	<i>6</i>
2.2 PUBLISHED RESEARCH ON Ti-6Al-4V.....	6
2.2.1 <i>Cavitation During Hot Tension Testing of Ti-6Al-4V.....</i>	<i>6</i>
2.2.2 <i>Cavitation and Failure During Hot Forging of Ti-6Al-4V.....</i>	<i>7</i>
2.2.3 <i>Flow Behavior and Globularization Kinetics during Hot Working of Ti-6Al-4V with a Colony Alpha Microstructure.....</i>	<i>7</i>
2.2.4 <i>Strain-Path Effects during Hot Working of Ti-6Al-4V with a Colony-Alpha Microstructure.....</i>	<i>7</i>
2.2.5 <i>Effect of Initial Microstructure on Plastic Flow and Dynamic Globularization during Hot Working of Ti-6Al-4V.....</i>	<i>8</i>
2.3 PUBLISHED RESEARCH ON Ti-6Al-4V AND TiAl.....	9
2.3.1 <i>Plastic Flow, Microstructure Evolution, and Defect Formation during Primary Hot Working of Titanium and Titanium Aluminide Alloys with Lamellar Colony Microstructures.....</i>	<i>9</i>
2.4 PUBLISHED RESEARCH ON THE RING TEST.....	9
2.4.1 <i>Effect of Flow Softening on Ring Test Calibration Curves.....</i>	<i>9</i>
2.4.2 <i>The Ring Test for P/M Materials.....</i>	<i>9</i>
2.5 PUBLISHED RESEARCH ON ECAE	10
2.5.1 <i>The Effect of Material Properties and Tooling Design on Deformation and Fracture During ECAE.....</i>	<i>10</i>
2.5.2 <i>Failure Modes during ECAE of Aluminum Alloy 2024.....</i>	<i>10</i>
2.6 PUBLISHED RESEARCH ON TEXTURE EFFECTS	11

2.6.1	<i>An Analysis of the Effect of Normal Plastic Anisotropy on the Tensile Ductility of Sheet Tension Specimens.....</i>	11
2.6.2	<i>An Investigation of the Effect of Texture on the High-Temperature Flow Behavior of an Orthorhombic Titanium Aluminide Alloy</i>	11
2.6.3	<i>Influence of Texture on Beta Grain Growth during Continuous Annealing of Ti-6Al-4V</i>	12
2.7	PUBLISHED RESEARCH ON CELLULAR AUTOMATA MODELING.....	12
2.7.1	<i>Static Recrystallization Kinetics with Homogeneous and Heterogeneous Nucleation using a Cellular Automata Model.....</i>	12
2.7.2	<i>Modeling Dynamic Recrystallization Using Cellular Automata</i>	12
2.7.3	<i>Dynamic Globularization of Lamellar Structures in a Near Gamma Titanium Aluminide Alloy</i>	13
2.8	PUBLISHED RESEARCH ON OTHER MODELING	16
2.8.1	<i>A Theoretical Investigation of the Effect of Materials Properties and Cavity Architecture/Shape on Ductile Failure During the Hot Tension Test.....</i>	16
2.8.2	<i>An Analysis of the Effect of Cavity Nucleation Rate and Cavity Coalescence on the Tensile Behavior of Superplastic Materials.....</i>	16
2.9	PUBLISHED RESEARCH ON OTHER WORK	17
2.9.1	<i>The Adiabatic Correction Factor for Deformation Heating During the Uniaxial Compression Test.....</i>	17
2.9.2	<i>Development of Nickel Alloy Substrates for Y-Ba-Cu-O Coated Conductor Applications</i>	17
3	UNPUBLISHED RESEARCH	19
3.1	CHARACTERIZATION OF THE FORGING DIE WORKPIECE INTERFACE FRICTION AND HEAT TRANSFER BETWEEN ALLOY STEEL AND ALLOY Ti-6Al-4V	19
3.1.1	<i>Introduction.....</i>	19
3.1.2	<i>Experimental Procedure</i>	19
3.1.3	<i>Compression Testing.....</i>	20
3.1.4	<i>Ring Tests.....</i>	20
3.1.5	<i>FEM</i>	24
3.1.6	<i>Summary of Results.....</i>	30
3.2	PROCESS MODELING FOR FRICTION STIR WELDING FOR THE METALS AFFORDABILITY INITIATIVE (MAI)	36
3.2.1	<i>Introduction.....</i>	36
3.2.2	<i>Statement of Work.....</i>	36
3.2.3	<i>Results and Discussion.....</i>	37
3.3	FURNACE COOLING OF TiAl DISKS	46
3.4	MICROSTRUCTURE DEVELOPMENT AND CRACK INITIATION DURING DEFORMATION PROCESSING OF GAMMA TITANIUM ALUMINIDE ALLOYS	48
3.5	SALT POT QUENCHING OF A TiAl BAR	48
3.6	CONSOLIDATION OF A WIRE Ti/SiC COMPOSITE	49
3.7	VOID GROWTH MODELING	49
3.8	FEASIBILITY OF AN ULTRASONIC DIE PRESSURE SENSOR	49
3.9	EXTRUSION OF NANOPHASE AL TUBING.....	49
3.10	DYNAMIC RECOVERY MODELING (DRX) USING CA.....	50
3.11	FEM OF ECAE OF TUNGSTEN HEAVY ALLOY FOR DOE	50
4	COOPERATIVE PROJECTS	52

4.1	COOPERATIVE TECHNOLOGY CLUSTERS (CTEC) PILOT PROGRAM.....	52
4.2	CRADA.....	53
4.2.1	<i>American Superconductor Corporation</i>	54
4.2.2	<i>RTI Energy Systems, Inc.</i>	54
4.2.3	<i>Boeing N.A. (Rocketdyne)</i>	54
4.2.4	<i>Howmet Research Corporation</i>	54
4.2.5	<i>UDRI</i>	54
4.2.6	<i>Allison Advanced Development Co.</i>	55
4.2.7	<i>Pratt & Whitney (Bernd Group)</i>	55
4.2.8	<i>Concurrent Technologies Corporation (CTC)</i>	55
4.2.9	<i>Boeing MAI</i>	55
4.2.10	<i>Department of Energy (DOE)</i>	55
4.2.11	<i>Pratt & Whitney</i>	55
4.2.12	<i>Pratt & Whitney (Bernd Group)</i>	55
4.2.13	<i>Lockheed - LDM</i>	55
5	PROCESSING OF MATERIALS.....	56
5.1	EXTRUSION	56
5.2	FORGING	58
5.3	ROLLING	59
5.4	MECHANICAL TESTING	60
5.5	EVACUATION AND DEGASSING	61
5.6	VACUUM ARC MELTING (BUTTON MELTS)	62
5.7	VACUUM INDUCTION MELTING (VIM)	63
5.8	HEAT TREATMENT.....	64
5.9	WELDING AND FABRICATION.....	65
6	OPERATION OF MATERIALS PROCESSING LAB	66
6.1	DESIGN AND BUILD RAPID HEAT TREATMENT TEST STAND.....	66
6.2	INSTALL AND COMMISSION SALT POT HEAT TREATMENT FURNACE	66
6.3	DESIGN, FABRICATE, AND COMMISSION ECAE TOOLING.....	66
6.4	INSTALL AND COMMISSION LOAD CELL IN 1000-TON FORGE PRESS	67
6.5	RELOCATION OF THE HARROP FURNACE AND REINFORCEMENT OF TRENCH COVERS	67
6.6	MAJOR PRESS MAINTENANCE.....	67
6.7	BUILD CLOSED LOOP COOLING SYSTEM	67
6.8	COMMISSIONING OF THE DS UNIT.....	68
6.9	200-KIP MTS TOOL SETUP	68
6.10	55-KIP MTS TOOL SETUP	68
6.11	DESIGN, BUILD, AND INSTALL SPINNING MOLD CASTING DEVICE.....	68
6.12	MOTHBALLING OF ISOTHERMAL CHAMBER	69
7	PUBLICATIONS AND PRESENTATIONS.....	70
7.1	PUBLICATIONS	70
7.2	PRESENTATIONS.....	73
7.3	SELECTED, LIMITED DISTRIBUTION REPORTS	74
8	REFERENCES.....	75
	APPENDIX A: CTEC FINAL REPORT.....	79
	LIST OF ACRONYMS	79

List of Figures

<u>Figure</u>	<u>Page</u>
Figure 1: DEFORM™ simulations for globularization modeling.....	15
Figure 2: The Flow Curves were for an Initial Lamellar Grain Size of 600 μm , at 1093, 1148, and 1204 $^{\circ}\text{C}$, and Compressed at Strain Rates of 0.001, 0.1, and 1.0 s^{-1}	16
Figure 3. Ring Test Setup	21
Figure 4. DEFORM™ FEM Meshes at 50 Percent Reductions for Various HTC's	25
Figure 5. HTC ($\text{kW}/\text{m}^2\text{K}$) Calibration Curves for Test 21	27
Figure 6. Load versus Displacement Curves Comparing FEM Curves to Experimental Curve for Test 21 (HTCs, $\text{kW}/\text{m}^2\text{K}$)	27
Figure 7. Effect of the HTC on the Friction Calibration Curves	29
Figure 8. Effect of Test Temperatures and Strain Rates on Friction Calibration Curves	29
Figure 9. Nonisothermal Friction Calibration Curves	30
Figure 10. FEM Temperature versus Time Curves from the Center of a Ring	32
Figure 11. Temperature versus Time and Load versus Time Curves for a Thermocoupled Ring Test and Comparable FEM Simulation (FEM HTC – 20 $\text{kW}/\text{m}^2\text{K}$).....	33
Figure 12. Flow Curves for Al 1100: (a) 4.0 s^{-1} , (b) 40.0 s^{-1}	37
Figure 13. Point Tracking	38
Figure 14. Flow Net.....	38
Figure 15. Simulation of Initial Tool Plunge	39
Figure 16. Comparison of Isothermal and Nonisothermal Deformation around Pin under 2-D Plane-Strain Conditions	40
Figure 17. Workpiece Temperature Contours and 1100Al Flow Stress versus Temperature for the Nonisothermal Simulation under 2-D Plane-Strain Conditions (500 $^{\circ}\text{C}$ Pin, 1000 rpm, and 1 mm/s).....	41
Figure 18. Comparison of Simulated and Experimental Tool Temperatures and Loads During FSW Tool Plunge.....	42
Figure 19. Tool Temperature versus Plunge Depth for Total Plunge Times of 15, 30, and 60 seconds.....	44
Figure 20. Load versus Plunge Depth for Total Plunge Times of 15, 30, and 60 seconds.....	44
Figure 21. Tool Temperature versus Time for Constant Tool Loads during Plunging to a Depth of 5.0 mm with Loads of 5000, 6000, and 7000 N	45
Figure 22. Tool Temperatures versus Plunge Depth for a 30 second Plunge Time (0.18 mm/s) and Tool Speeds of 250, 500, 1000, and 1250 rpm.....	45
Figure 23. Load versus Plunge Depth for a Plunge Time of 30 seconds (0.18 mm/s) and Tool Speeds of 250, 500, 1000, and 1250 rpm.....	46
Figure 24. Cooling Curves for TiAl Disks Showing Disk Temperatures at Mid-radius and Mid-height with Various Furnace Cooling Rates (50, 200, and 600 $^{\circ}\text{F}/\text{min}$) and TiAl Emissivities (0.3 and 0.6).....	47
Figure 25. Temperature versus Time Curves for a TiAl Bar Preheated to 1315 $^{\circ}\text{C}$ and Quenched in a Salt Bath at either 871 or 1037 $^{\circ}\text{C}$ using a 1-D Lumped-Parameter Numerical Analysis.....	48
Figure 26. (a) Comparison of $\rho(t)$ using CA and the Integrated Equation, (b) Strain Hardening Rates for Dynamic Recovery only using CA, Laasraoui-Jonas, and Roberts.....	50

List of Tables

<u>Table</u>	<u>Page</u>
Table 1. Ti-6Al-4V Flow Stress @ 0.1s^{-1}	22
Table 2. Ti-6Al-4V Flow Stress @ 1.0s^{-1}	22
Table 3. Ring Test Data: Tests 1 through 48 ($815\text{ }^{\circ}\text{C}$ - $1037\text{ }^{\circ}\text{C}$)	23
Table 4. Ring Test Data: Tests 49 through 60 ($676\text{ }^{\circ}\text{C}$)	24
Table 5. Interface HTC's used in FEM Simulations for Friction Factor Calibration Curve Generation.....	28
Table 6. Friction Factors for Lubricant – Deltaforge F-31	33
Table 7. Friction Factors for Lubricant – Oil-Dag.....	34
Table 8. Friction Factors for Lubricant – GP-200	35
Table 9. CRADA Tasks for American Superconductor	54
Table 10. Summary of Extrusion Operations.....	57
Table 11. Summary of Forging Operations	58
Table 12. Summary of Rolling Operations.....	59
Table 13. Summary of Mechanical Testing	60
Table 14. Summary of Evacuation, Outgassing, and Sealing Operations	61
Table 15. Summary of Vacuum Arc Melting	62
Table 16. Summary of VIM.....	63
Table 17. Summary of Heat Treat Operations	64
Table 18. Summary of Welding Operations.....	65

FOREWORD

This report was prepared by the Materials and Processes Division of UES, Inc., Dayton, Ohio under Air Force Contract No. F33615-96-C-5251. Mr. William T. O'Hara of the Metals Branch of the Metals, Ceramics and Non-Destructive Evaluation Division of the Air Force Research Laboratory was the Government Project Engineer. The research reported herein covers the period 23 August 1996 to 23 January 2001.

1 INTRODUCTION

The objectives of this program were to (1) investigate and determine the processing conditions required to achieve desired microstructures and mechanical properties in advanced aerospace materials, (2) implement and use analytical models for process design in the Materials Processing Laboratory (MPL), (3) validate analytical models by physical modeling, and (4) create a center of excellence for materials processing. Primary emphasis was given to composites and high temperature materials used in advanced engines and structures.

Materials of various types and compositions were studied. In several cases, a full-fledged processing science approach was utilized, in which the material was fully characterized in terms of microstructural and flow behavior, the proposed processing method was modeled analytically, the actual processing was carried out in the MPL and the analytical model was validated with experimental measurements. In other cases, some of these steps were eliminated when the material or process was well understood.

2 PUBLISHED RESEARCH

2.1 Published Research on Intermetallics

2.1.1 A Criterion for Intergranular Fracture During Hot Working of a Near Gamma Titanium Aluminide Alloy

Because they are designed for high-temperature service, intermetallic alloys can be difficult to manufacture via conventional hot-working operations. The processing window in terms of strain rates and temperatures that may be utilized to produce sound products of these materials is usually quite narrow. Such problems can be especially severe for ingot-cast forms of these alloys, which consist of relatively coarse-grain microstructures. These coarse structures are particularly susceptible to brittle failures during hot working due to the initiation and propagation of wedge cracks or the nucleation, growth, and coalescence of cavities at the grain boundaries. Thus, the development of models for the initiation and propagation of defects during hot working can be very helpful in the selection of processing conditions in order to avoid extensive and expensive laboratory experimentation.

One group of intermetallic alloys that has posed major challenges during hot working is that based on the gamma (TiAl) phase of the titanium-aluminum system. The hot workability of these materials is substantially improved when the alloy composition is slightly off-stoichiometric (i.e., melted to aluminum levels less than 50 atomic percent) to produce two-phase [TiAl and Ti₃Al (alpha-two)] mixtures. A modicum of success has been achieved in processing of these so-called near-gamma titanium aluminide alloys via techniques such as isothermal forging, canned, conventional hot forging and extrusion, and equal channel angular extrusion. Nevertheless, processing parameters to avoid fracture during ingot breakdown or secondary processing are still selected to some degree by trial-and-error techniques or by recourse to an expanding experience base for a variety of binary, ternary, and higher order gamma plus alpha-two alloys of various compositions and cast grain sizes.

The objective of this work was to begin the development of models for the hot workability of near-gamma titanium aluminide alloys under high-rate deformation conditions that characterize conventional metalworking processes. For this purpose, isothermal, hot compression test results for a typical near-gamma titanium aluminide were analyzed to formulate a criterion for the formation of wedge cracks in these materials. This work was published in *Scripta Materialia* by Semiatin and Seetharaman [1].

2.1.2 Analysis of Grain Growth in a Two-Phase Gamma Titanium Aluminide Alloy

Microstructure evolution during annealing of a wrought near-gamma titanium aluminide alloy, Ti-45.5Al-2Nb-2Cr (at. pct), in the temperature range 1200 °C to 1320 °C was investigated. The mean grain size of the alpha phase as well as the volume fraction and size of the gamma particles were evaluated as a function of annealing temperature and time. Isothermal annealing at temperatures above the alpha transus ($T_a = 1300$ °C) led to rapid grain growth of the alpha phase, the kinetics of which could be described by a simple power-law-type expression with a grain growth exponent $p = 2.3$. Alpha grain growth was significantly retarded during annealing at

subtransus temperatures ($1200\text{ }^{\circ}\text{C} \leq T \leq 1300\text{ }^{\circ}\text{C}$) by the pinning influence of gamma-phase particles. Limiting grain size values predicted by computer simulation models applicable for high-volume fractions of precipitates/particles were in good agreement with experimental findings. The kinetics of alpha grain in the presence of gamma particles were analyzed, and the results showed that a grain growth exponent of $p \approx 2.6$ could satisfactorily account for the experimental results. This work was published in *Metallurgical and Materials Transactions A* by Seetharaman and Semiatin [2].

2.1.3 Modeling of Cracking and Cavitation During Hot Working of Gamma Titanium Aluminides

Hot workability of near gamma titanium aluminides was assessed using hot compression and hot tension tests. A simple model for the brittle intergranular failure of these alloys during hot working was developed to seek correlations between flow properties, microstructural characteristics, and the propensity for cracking. The onset of wedge cracking was predicted using a criterion based on a critical value of the product of the peak flow stress and the square root of the grain size. In contrast, the occurrence of ductile fracture of the workpiece in regions subject to secondary tensile stresses is controlled by the kinetics of nucleation, growth, and coalescence of cavities. This type of cavitation damage could be predicted using the maximum tensile work criterion proposed originally by Cockcroft and Latham. Failures resulting from severe flow localization were analyzed in terms of the relative magnitudes of the normalized flow-softening rate and the strain rate sensitivity. The applicability of the preceding criteria for the onset of brittle and ductile fracture during deformation processing of near gamma titanium aluminide alloys was analyzed. This work was published in *Modeling of Mechanical Response of Structural Materials* by Seetharaman and Semiatin [3].

2.1.4 Phase Stability in a Ti-45.5Al-2Nb-2Cr Alloy

High temperature phase equilibria in a Ti-45.5Al-2Nb-2Cr alloy were investigated via metallography, X-ray diffraction (XRD) and electron microprobe analysis. The alloy was extensively hot worked through a sequence of isothermal forging and pack rolling operations coupled with intermediate, recrystallization heat treatments. Specimens from the rolled sheets were subjected to prolonged isothermal heat treatments in the temperature range $900\text{ }^{\circ}\text{C}$ to $1400\text{ }^{\circ}\text{C}$ for durations ranging up to 100 hours, followed by water quenching as well as slow cooling. The results indicated that a three-phase equilibrium involving γ , α/α_2 , and β/β_2 phases exists in the temperature range $900\text{ }^{\circ}\text{C}$ to $1250\text{ }^{\circ}\text{C}$. While the volume fraction of β_2 appears to reach a maximum at $\sim 1200\text{ }^{\circ}\text{C}$, that of α increases rapidly with temperature in the range $1200\text{ }^{\circ}\text{C}$ to $1300\text{ }^{\circ}\text{C}$. Heat treatment in the single α field ($1300\text{ }^{\circ}\text{C}$ to $1340\text{ }^{\circ}\text{C}$) led to pronounced grain growth, whereas annealing in the $\alpha + \beta$ field ($T > 1340\text{ }^{\circ}\text{C}$) caused retardation in the growth of α grains. The influence of heat treatment temperature and cooling rate on microstructure evolution in this alloy is discussed in the light of available information on phase stability in Ti-Al-X systems, where X is a beta-stabilizing element. This work was published in *Advances in the Science and Technology of Titanium Processing* by Seetharaman, Lombard, and Semiatin [4].

2.1.5 Plastic Flow and Microstructure Evolution during Hot Deformation of a Gamma Titanium Aluminide Alloy

The hot workability of a near gamma titanium aluminide alloy, Ti-49.5Al-2.5Nb-1.1Mn, was assessed in both the cast and the wrought conditions through a series of tension tests conducted over a wide range of strain rates (10^{-4} to 10^0 s $^{-1}$) and temperatures (850 °C to 1377 °C). Tensile flow curves for both materials exhibited sharp peaks at low strain levels followed by pronounced necking and flow localization at high strain levels. A phenomenological analysis of the strain rate and temperature dependence of the peak stress data yielded an average value of the strain rate sensitivity equal to 0.21 and an apparent activation energy of ~ 411 kJ/mol. At low strain rates, the tensile ductility displayed a maximum at ~ 1050 °C to 1150 °C, whereas at high strain rates, a sharp transition from a brittle behavior at low temperatures to a ductile behavior at high temperatures was noticed. Dynamic recrystallization of the gamma phase was the major softening mechanism controlling the growth and coalescence of cavities and wedge cracks in specimens deformed at strain rates of 10^{-4} to 10^{-2} s $^{-1}$ and temperatures varying from 950 °C to 1250 °C. The dynamically recrystallized grain size followed a power-law relationship with the Zener-Hollomon parameter. Deformation at temperatures higher than 1270 °C led to the formation of randomly oriented alpha laths within the gamma grains at low strain levels followed by their reorientation and evolution into fibrous structures containing $\gamma + \alpha$ phases, resulting in excellent ductility even at high strain rates. This work was published in *Metallurgical and Materials Transactions A* by Seetharaman and Semiatin [5].

2.1.6 Intergranular Fracture of Gamma Titanium Aluminides under Hot Working Conditions

A comparative study of the hot workability of a near gamma titanium aluminide alloy Ti-49.5Al-2.5Nb-1.1Mn in the cast and wrought conditions was performed. Tension tests conducted on coarse grain, cast material, and fine grain wrought material revealed a pronounced variation in both fracture/peak stress and ductility with temperature and strain rate. Brittle, intergranular fracture occurring at high strain rates was found to be controlled by wedge crack nucleation, whereas the ductile fracture observed at low strain rates was controlled by the growth of wedge cracks and cavities. Dynamic recrystallization was shown to be the main restorative mechanism to accommodate grain boundary sliding and thereby control the crack growth rates. The ductile-to-brittle (DB) transition was found to be determined by the critical values of a grain size-based stress intensity factor given by the product of the peak/fracture stress and the square root of grain size. A processing map for the near gamma titanium aluminides was constructed based on the comparative analysis of the hot tension and compression test results. This work was published in *Metallurgical and Materials Transactions A* by Seetharaman and Semiatin [6].

2.1.7 Phase Transformation Behavior of Gamma Titanium Aluminide Alloys During Supertransus Heat Treatment

Microstructure evolution in a wrought near-gamma titanium alloy, Ti-45Al-2Cr-2Nb, was investigated by a series of heat treatments comprised of initial heating high in the alpha-plus-gamma phase field followed by short-time heating in the single-phase alpha field. The initial heating step led to a dispersion of gamma particles, which pinned the alpha grain boundaries. The kinetics of the gamma grain dissolution during subsequent heating in the single-phase field

were interpreted in terms of models for both interface reaction-controlled and diffusion-controlled processes. The model for diffusion-controlled dissolution yielded predictions comparable to the observed times, whereas the model for interface reaction-controlled behavior predicted dissolution kinetics over an order of magnitude slower than observed. The growth of the alpha grains, both before and after the dissolution of the gamma phase, was also modeled. Section size limitations to the ability to use supertransus heating to obtain uniform and moderately fine alpha grain sizes were examined using the transformation models and a simple heat transfer analysis approach. The results were validated through the heat treatment of subscale and full-scale forgings. This work was published in *Metallurgical and Materials Transactions A* by Semiatin, Seetharaman, Dimiduk and Ashbee [7].

2.1.8 The Knoop-Hardness Yield Locus of an Orthorhombic Titanium Aluminide Alloy

Extensive research has been conducted recently to develop an understanding of the properties and processing of an emerging class of titanium aluminide alloys based on the orthorhombic Ti_2AlNb phase. These materials possess a good combination of room- and high-temperature mechanical properties. Microstructure evolution during various thermomechanical processes in the single- or two-phase field has been established. The effect of the mechanical and crystallographic texture developed during primary processing on ambient and elevated temperature properties has also been investigated.

The objective of the work reported was to establish the plastic anisotropy of a Ti-21Al-22Nb (atomic percent) sheet material in the as-fabricated condition as well as after subsequent hot-tension deformation. For this purpose, plane-stress yield loci were determined using a Knoop microhardness method and interpreted in terms of measured tensile properties and aggregate theory calculations based on the measured textures in the sheet. This work was published in *Metallurgical and Materials Transactions A* by Nicolaou and Semiatin [8].

2.1.9 Dynamic Globularization of Lamellar Structures in a Near Gamma Titanium Aluminide Alloy

The kinetics of dynamic globularization of the lamellar microstructure and the associated flow softening behavior during hot working of a near gamma titanium aluminide alloy were investigated. Isothermal compression tests were conducted on specimens of Ti-45.5Al-2Nb-2Cr containing fully lamellar microstructures at 1093 °C to 1204 °C and strain rates ranging from 0.001 s^{-1} to 1.0 s^{-1} . Both the peak stress and flow-softening rate were strongly dependent on the test temperature and the strain rate. Microbuckling of the lamellae in the interior regions of the grains and the formation of fine, equiaxed grains at the grain boundaries constituted the major microstructural changes during hot deformation. The kinetics of the dynamic globularization process and its influence on the flow stress of the alloy were interpreted via numerical simulation of the coupled plastic flow and globularization processes using a finite element model (FEM). This work was published in *Recrystallization and Related Phenomena (ReX '99)* by Seetharaman, Goetz and Semiatin [9].

2.1.10 Microstructures and Tensile Properties of Ti-45.5Al-2Nb-2Cr Rolled Sheets

Tension tests were carried out at 20, 704, 760, and 815 °C on sheet specimens machined from pack rolled and heat-treated sheets of a multiphase gamma titanium aluminide alloy, Ti-45.5Al-2Nb-2Cr. The microstructures of the heat-treated sheets ranged from equiaxed, recrystallized primary gamma structure obtained by annealing at 1200 °C to the fine-grained, fully lamellar structure obtained by a short-term solution treatment at 1320 °C followed by air cooling to 900 °C. The yield strength and the tensile strength of specimens containing the equiaxed, primary gamma microstructure were consistently low at all test temperatures, while the strength properties of duplex and fully lamellar structures were comparatively quite high. The tensile ductility values showed a complex dependence on the microstructure and the test temperature. Fully lamellar structures exhibited poor ductility at all temperatures up to 815 °C. Fractography and metallography of the tensile test specimens revealed evidence of a mixture of failure mechanisms: cleavage cracking, ductile failure by microvoid coalescence, and intergranular fracture by cavitation and wedge cracking. The relative contributions of these mechanisms varied with the initial microstructure and the test temperature. Both the lamellar grains and the gamma grains became significantly elongated near the fracture zone, particularly in specimens deformed at 760 and 815 °C. The yield and tensile strength of Ti-45.5Al-2Nb-2Cr alloy sheets in all microstructural conditions were significantly higher than those reported for a majority of alloys containing 47-49% aluminum. However, the ductile-to-brittle transition temperatures of the Ti-45.5Al-2Nb-2Cr alloy were somewhat higher than those obtained for the majority of gamma titanium aluminides. This work was published in *Materials Science and Engineering A* by Seetharaman and Semiatin [10].

2.2 Published Research on Ti-6Al-4V

2.2.1 Cavitation During Hot Tension Testing of Ti-6Al-4V

Cavity initiation, growth, and coalescence phenomena during the hot tension testing of Ti-6Al-4V with several different transformed β -microstructures were established to obtain an understanding of the failure process during subtransus hot working. Samples with either a colony-type microstructure (containing grain-boundary α) or a martensitic, acicular α -microstructure were pulled to failure at strain rates between 0.01 and 3 s⁻¹ and various subtransus temperatures ranging from 540 to 955 °C. Metallographic analysis of sectioned tension samples with colony microstructures revealed that cavity initiation occurred at very low strains (≤ 0.2) irrespective of strain rate at temperatures below 900 °C due to an apparent incompatibility of deformation between the grain-boundary α -layer and the Widmanstätten side plates. Initiation strains were somewhat higher (~ 0.2 to 0.5) for samples with the acicular microstructure tested at temperatures below 900 °C; however, failure was still intergranular. Subsequent cavity growth was more rapid for colony microstructures than that for the martensitic microstructure at these temperatures. Above 900 °C, however, substantially higher cavity initiation strains and lower cavity growth rates were obtained for both microstructures. These latter behaviors were ascribed to the presence of a large volume fraction of ductile β -phase and moderate values of the strain-rate sensitivity of the flow stress, respectively. This work was published in *Materials Science and Engineering A* by Semiatin, Seetharaman, Ghosh, Shell, Simon and Fagin [11].

2.2.2 Cavitation and Failure During Hot Forging of Ti-6Al-4V

The occurrence of cavity initiation and gross, free-surface fracture during subtransus hot pancake forging of Ti-6Al-4V with a transformed beta (colony) microstructure was established. Cavity initiation mechanisms were one of two distinct types. At temperatures approximately 75 °C or more below the beta transus temperature (T_b), cavity initiation occurred at relatively low strains in the beta phase lying between the grain-boundary alpha phase and the lamellar colonies. By contrast, at temperatures near the transus (*i.e.*, $T \approx T_b - 25$ °C), cavity initiation occurred at much larger strains as a result of microfracture of partially-to-fully-globularized alpha phase. FEM of the pancake forging process revealed that secondary tensile stresses had been developed in the regions that had exhibited cavitation/fracture. The FEM analyses were used to correlate both the cavity initiation and the gross free-surface fracture results to previous observations from uniaxial hot tension tests in which identical damage mechanisms had been observed. The tensile work criterion of Cockcroft and Latham gave moderately good (quantitative) correlation between the forging and uniaxial tension behaviors. An alternative comparison based on the Rice and Tracey cavity growth model gave reasonable predictions of free surface fracture but tended to overestimate the incidence of subsurface cavity initiation. This work was published in *Metallurgical and Materials Transactions A* by Semiatin, Goetz, Shell, Seetharaman and Ghosh [12].

2.2.3 Flow Behavior and Globularization Kinetics during Hot Working of Ti-6Al-4V with a Colony Alpha Microstructure

The effect of process variables on flow response and microstructure evolution during hot working of Ti-6Al-4V with a colony alpha preform microstructure was established using isothermal hot compression tests. Testing was conducted on material with prior-beta grain sizes of 100 μm or 400 μm at strain rates of 0.001 to 10 s^{-1} , test temperatures between 815 and 955 °C and height reductions of 40 to 80 percent. All of the flow curves exhibited a peak stress followed by moderate flow softening. The absence of a grain/colony size dependence of flow behavior, coupled with relatively low values of the strain rate sensitivity of the flow stress (~ 0.05 to 0.30), led to the conclusion that deformation was controlled by dislocation glide/climb processes. Flow softening was interpreted in terms of deformation heating and substructure/texture evolution. The dependence on strain rate and temperature of the kinetics of dynamic globularization of the colony microstructure was complex and appeared to be of second-order importance compared to the effects of strain per se, thus suggesting the dominance of dislocation-type processes for the control of globularization as well. This work was published in *Materials Science and Engineering A* by Semiatin, Seetharaman and Weiss [13].

2.2.4 Strain-Path Effects during Hot Working of Ti-6Al-4V with a Colony-Alpha Microstructure

The conversion of titanium ingot materials to wrought mill products often involves a series of hot-working and heat-treatment steps. One of the most important steps consists of the breakdown of the lamellar colony or acicular microstructure formed during cooling after beta working or recrystallization heat treatment. This breakdown operation usually comprises upsetting or cogging operations followed by annealing in the alpha-beta phase field to produce a globularized-alpha structure.

Recently, DeLo et al. [14,15] have established that the equal channel angular extrusion (ECAE) process can also be used effectively to convert the colony microstructure in a typical alpha/beta alloy Ti-6Al-4V. However, it was shown that the successful application of the method requires an increment of upsetting deformation prior to the shear that is imposed in the ECAE deformation zone. The efficacy of this approach was rationalized on the basis of the dependence of flow-softening rate on strain. At low strains ($\epsilon < 0.5$), the flow-softening rate is high for Ti-6Al-4V (and similar alloys) with a colony microstructure, and the tendency for flow localization in shear is very high. At larger strains, at which flow softening is much lower, flow localization is less likely. Hence, the use of an initial increment of upset deformation, which is inherently more stable than shear because of geometric hardening, was thought to be beneficial through its ability to predeform the material uniformly to a strain at which flow softening and the tendency for flow localization in shear were considerably diminished.

The primary objective of this work was to provide a basis for an alternate, but equally plausible, explanation for the stabilizing effect of an upset prestrain on flow stability during ECAE. Specifically, the effect of a strain-path change on flow softening was established. A second objective was to establish the precise prestrain required to stabilize flow during ECAE and to relate this strain to the strain-path observations.

The effect of a strain-path change on flow response and flow stability was assessed via two sets of experiments. Both made use of Ti-6Al-4V material which had been heat treated to develop a colony microstructure with similar beta grain, colony size, and alpha plate thickness. This heat treatment comprised 940 °C/20 min + 1065 °C/15 min + 940 °C/5 min + 815 °C/15 min + air cool. A microstructure consisting of 600- μ m beta grains with 150- μ m colonies having 1- μ m-thick alpha plates (at hot working temperatures) was thus produced. Both materials had a beta transus temperature (at which alpha + beta \rightarrow beta) of approximately 955 °C. This work was published in *Metallurgical and Materials Transactions A* by Semiatin, Brown, Brown, DeLo, Bieler and Beynon [16].

2.2.5 Effect of Initial Microstructure on Plastic Flow and Dynamic Globularization during Hot Working of Ti-6Al-4V

Plastic flow behavior and globularization kinetics during subtransus hot working were determined for Ti-6Al-4V with three different transformed beta microstructures. These conditions consisted of fine lamellar colonies, a mixture of coarse colonies and acicular alpha, and acicular alpha. Isothermal hot compression tests were performed on cylindrical samples at subtransus temperatures and strain rates typical of ingot breakdown (i.e., $T \sim 815$ °C to 955 °C, $\dot{\epsilon}_{\text{eff}} \sim 0.1$ s⁻¹). For all three material conditions, true stress-true strain curves exhibited a peak stress followed by noticeable flow softening; the values of peak stress and flow softening rate showed dependence on starting microstructure.

On the other hand, the kinetics of dynamic globularization varied noticeably with microstructure. By and large, the globularization rate under a given set of deformation conditions was most rapid for the fine acicular microstructure and least rapid for the mixed coarse-colony/acicular structure. At temperatures close to the beta transus, however, the difference in globularization rates for the three microstructures was less, an effect attributed to the rapid (continuous) coarsening of the laths in the acicular microstructure during preheating prior to hot working. The absence of a

correlation between the globularization kinetics and the observed flow softening at low strains suggested platelet/lath bending and kinking as the primary deformation mechanism that controls the shape of the flow curves. This work was published in *Metallurgical and Materials Transactions A* by Shell and Semiatin [17].

2.3 Published Research on Ti-6Al-4V and TiAl

2.3.1 Plastic Flow, Microstructure Evolution, and Defect Formation during Primary Hot Working of Titanium and Titanium Aluminide Alloys with Lamellar Colony Microstructures

Plastic flow response, microstructure evolution, and defect formation during the primary hot working of conventional alpha/beta titanium alloys and gamma titanium aluminide alloys with two-phase lamellar colony microstructures were reviewed. The effects of initial grain/colony size, deformation rate and temperature on constitutive behaviour and the mechanisms associated with the observed flow softening were discussed. The kinetics of dynamic globularization were summarized and interpreted in terms of measured constitutive response. In addition, the mechanisms underlying failure via shear localization and cavitation during breakdown metalworking operations were also described. This work was published in *Philosophical Transactions Royal Society of London A* by Semiatin, Seetharaman and Ghosh [18].

2.4 Published Research on the Ring Test

2.4.1 Effect of Flow Softening on Ring Test Calibration Curves

The application of the ring test to assess die-workpiece interface friction during forging of a flow softening material was investigated. Calibration curves were generated by conducting FEM simulations of ring forging with different friction factors. The method was validated by conducting isothermal, hot compression tests on rings of an α_2 titanium aluminide alloy for both lubricated and unlubricated interface conditions. The FEM results for the flow softening material were compared to those generated assuming no flow softening. In all cases, the differences between the predicted curves for the flow softening and non-softening behaviors were quite small. Furthermore, for given values of the interface friction factor, the calibration curves were essentially independent of the strain rate sensitivity (m) and flow softening. This work was published in *Materials Science and Engineering A* by Dutton, Seetharaman, Goetz and Semiatin [19].

2.4.2 The Ring Test for P/M Materials

The application of the ring test to assess die-workpiece interface friction during forging of powder metallurgical materials was investigated. As for fully dense materials, the change in internal diameter as a function of height reduction was used to quantify friction. To this end, calibration curves were generated by conducting FEM simulations of ring forging with different friction factors. The method was validated by conducting isothermal, hot compression tests on rings of an α_2 titanium aluminide alloy with starting densities of 75, 85, or 100 percent of full theoretical density. Comparison of the test data to the calibration curves revealed somewhat higher friction factors for the porous materials (as compared to the fully dense material) for both

lubricated and unlubricated interface conditions. Furthermore, the accuracy of the FEM simulations of the ring test was confirmed by good agreement between measured and predicted density distributions and load-stroke curves for tests on the porous titanium aluminide material. This work was published in *Journal of Manufacturing Science and Engineering* by Dutton, Goetz, Shamasundar and Semiatin [20].

2.5 Published Research on ECAE

2.5.1 The Effect of Material Properties and Tooling Design on Deformation and Fracture During ECAE

The effects of material constitutive behavior, tooling design, and friction conditions on metal flow, stress fields, and the tendency for tensile fracture during ECAE were established using a FEM technique. Three different material behaviors, typical of those encountered during cold and hot working, were investigated. These comprised (1) strain hardening, (2) rigid, perfectly plastic, and (3) flow softening types of behavior. The tooling geometries consisted of a so-called simple design with no moving channel members and a complex design with a sliding bottom floor. The FEM results indicated that the most uniform flow was obtained during ECAE of a strain-hardening material having low strain-rate sensitivity in tooling with a sharp inner corner (front leg) radius. The ECAE of materials with other constitutive behaviors or in tooling with a radiused front leg showed some degree of flow nonuniformity, even away from the head and tail of the extrusion. Tooling design and material properties were also predicted to have an important influence on the tensile stresses and hence tensile damage developed during ECAE. The FEM results were validated using viscoplasticity and fracture observations for AISI 4340 steel and a near-gamma titanium aluminide alloy. This work was published in *Acta Metallurgica* by Semiatin, DeLo and Shell [21].

2.5.2 Failure Modes during ECAE of Aluminum Alloy 2024

ECAE is an emerging metals-processing technique developed by Segal in the former Soviet Union. Metal flow comprises deformation through two intersecting channels of equal cross-sectional area. The imparted strain is a function primarily of the angle between the two channels. For an angle of 90 degrees, for example, the effective strain is approximately equal to 1.15. By passing the workpiece through the tooling many times, very large deformations can be developed. Hence, the process has been investigated as a means to refine microstructure and control texture. The majority of this work focused on alloys of aluminum, copper, iron, nickel, and titanium. The objective of this work was to elucidate the competition between flow-localization-controlled and fracture-controlled failure during ECAE and thus to provide guidance for the selection of process variables. Because of the extensive amount of work that is currently being performed for aluminum-base materials, the program focused on aluminum-alloy 2024. The results of this investigation verified that two distinct types of failure might occur during ECAE. The specific type depends on two material properties, the alpha parameter in shear, γ/m , and the critical tensile damage factor from the Cockcroft and Latham criterion. Depending on the specific values of these properties, fracture, shear localization, or a combination of the two may occur. This work was published in *Metallurgical and Materials Transactions A* by Fagin, Brown, Brown, Jata and Semiatin [22].

2.6 Published Research on Texture Effects

2.6.1 *An Analysis of the Effect of Normal Plastic Anisotropy on the Tensile Ductility of Sheet Tension Specimens*

The uniaxial tension test is the oldest and most common technique used to obtain mechanical property data and to gain insight into the formability of engineering materials. Interpretation of tensile behavior prior to the load maximum is simple; however, the postload maximum deformation is usually quite complex. As a result, extensive theoretical work has been conducted to determine the factors that govern the kinetics of flow localization. These factors include the strain-rate hardening behavior and, to a lesser degree, the strain-hardening behavior. For sheet tensile specimens, the normal plastic anisotropy parameter (r value) is another factor that may affect necking behavior; however, its influence has been studied to only a limited extent.

The objective of the present work was to establish the effect of normal plastic anisotropy on the tensile behavior of sheet specimens. To this end, theoretical analyses were conducted in two major areas. In the first, the influence of r on the transverse stresses and the stress-correction factor during neck development were determined. In the second area of investigation, these results were implemented into a finite difference (direct-equilibrium) simulation of the sheet tension test to establish the effect of r on the stress-strain behavior and ductility. This work was published in *Scripta Materialia* by Nicolaou and Semiatin [23].

2.6.2 *An Investigation of the Effect of Texture on the High-Temperature Flow Behavior of an Orthorhombic Titanium Aluminide Alloy*

The effect of mechanical and crystallographic texture on the flow properties of a Ti-21Al-22Nb (atomic pct) sheet alloy was determined by conducting uniaxial tension and plane-strain compression tests at temperatures between 900 °C and 1060 °C and strain rates between 10^{-4} and 10^{-2} s^{-1} . Despite the presence of noticeable initial texture, all of the mechanical properties for a given test temperature and strain rate (i.e., stress, total elongation to failure, strain-rate sensitivity, and normal plastic anisotropy) were essentially identical irrespective of test direction relative to the rolling direction of the sheet. The absence of an effect of mechanical texture on properties such as ductility was explained by the following: (1) the initially elongated second-phase particles break up during tension tests parallel to the rolling direction of the sheet, thereby producing a globular morphology similar to that noted in samples taken transverse to the rolling direction; and (2) failure was flow localization, rather than fracture, controlled. Similarly, the absence of an effect of mechanical texture on strain-rate sensitivity (m values), normal plastic anisotropy (r values), and the ratio of the plane strain to uniaxial flow stresses was rationalized on the basis of the dominance of matrix (dislocation) slip processes within the ordered beta phase (B2) as opposed to grain boundary sliding. Aggregate theory predictions supported this conclusion inasmuch as the crystallographic texture components determined for the B2 phase ((001) [100] and $(\bar{1}12)$ [110]) would each produce identical r values and uniaxial and plane-strain flow stresses in the rolling, and transverse directions. This work was published in *Metallurgical and Materials Transactions A* by Nicolaou and Semiatin [24].

2.6.3 Influence of Texture on Beta Grain Growth during Continuous Annealing of Ti-6Al-4V

The kinetics of grain growth during continuous beta annealing of two different lots of Ti-6Al-4V bar stock with an equiaxed-alpha preform microstructure were determined using an induction-heating technique. Heating rates of 1.4, 5.6, and 18 °C s⁻¹ and peak temperatures between 1020 and 1260 °C were utilized. Noticeable differences were found in the grain-growth behaviors of the two lots of material with one exhibiting much smaller grain sizes than the other for a given set of processing conditions. A semiquantitative analysis of the results revealed that the two batches of alloy had similar grain-growth exponents and activation energies but different rate constants. These trends were explained in terms of the beta-phase textures in the as-received materials, which persisted during beta annealing. The former material had a moderate strength, cube-like texture, whereas the latter lot of material exhibited a very strong and sharper fiber texture. The grain-growth results were thus explained in terms of the effect of texture on grain-boundary surface energy/mobility. This work was published in *Materials Science and Engineering A* by Semiatin, Fagin, Glavicic, Sukonnik, and Ivasishin [25].

2.7 Published Research on Cellular Automata Modeling

2.7.1 Static Recrystallization Kinetics with Homogeneous and Heterogeneous Nucleation using a Cellular Automata Model

The kinetics of homogeneous and heterogeneous static recrystallization in a single-phase material were analyzed using two-dimensional (2-D) and three-dimensional (3-D) CA. A CA model was developed, which was then validated using the theory based on relationships developed by Johnson and Mehl, Avrami, and Kolmogorov (JMAK) for homogeneous site-saturated and constant-rate nucleation. The model was then modified for heterogeneous nucleation at grain boundaries, with either a fixed number of nuclei or a constant rate of nucleation. The fraction of boundary sites nucleated, for the case of fixed nucleation, varied from 0.006 to 0.28, resulting in Avrami exponents (k) ranging from 1.8 to 1.1 (site saturation). Site saturation with fixed nucleation produced a lamellar microstructure. The parameters of q and m , from Vandermeer's microstructural path method, were calculated and compared with theoretical values. Constant-rate nucleation at grain boundaries between newly recrystallized grains and the unrecrystallized matrix resulted in k values of ≈ 1 . Simulated microstructures revealed that with a low nucleation rate, recrystallized grains formed in clusters, while a high nucleation rate resulted in a necklace microstructure, with kinetics similar to those observed in dynamic recrystallization ($k = 1.4$). This work was published in *Metallurgical and Materials Transactions A* by Goetz and Seetharaman [26].

2.7.2 Modeling Dynamic Recrystallization Using Cellular Automata

Dynamic recrystallization (DRX) and dynamic recovery (DR) are two competing processes by which metals and alloys undergo a reduction in the density of accumulated dislocations during plastic deformation at elevated temperatures. Certain high stacking-fault energy materials, such as Al, α -iron, and their single phase alloys, do not readily undergo DRX because DR by cross-slip and climb processes is sufficiently rapid to prevent dislocation densities from reaching levels critical for the formation of DRX nuclei. With low stacking fault energy materials, such as

copper, nickel, γ -iron, and their single-phase alloys, dissociation of dislocations into widely separated partials renders cross-slip and climb processes very difficult. This effectively reduces the rate of DR; thereby allowing dislocation densities to attain high values required for the nucleation of dynamically recrystallized, strain free crystals. It is important to note that DR occurs either separately or in conjunction with DRX.

The objective of this work was to model DRX under isothermal and constant strain rate conditions using the cellular automata (CA) technique. CA is similar to the Monte Carlo (MC) method. However, fundamental differences exist due to the use of different phenomenological relationships, MC's probabilistic method of grain boundary motion and its use of the Potts model. This study is a sequel to the authors' work on static recrystallization at grain boundaries using CA [Sec. 2.7.1]. The application of CA to DRX was practical because DRX also occurs through grain boundary nucleation. The model was used to examine the effect of initial grain size on the transition from single to multipeak flow curves, nucleation density, recrystallization kinetics, and the strain hardening rate.

Modeling of DRX by CA is a two-step process in which an initial microstructure is first created. For DRX, the dislocation density of a cell, ρ^C is tracked and determines nucleation and growth. If a critical dislocation density is reached in any cell located on a grain boundary, DRX begins. The following four processes take place sequentially: (1) cell dislocation input, (2) DR, (3) nucleation of recrystallized grains, and (4) growth of recrystallized grains. Cell dislocation density is incremented uniformly at a fixed rate, $d\rho/dt$, for each time step. Strain and strain rate are assumed to be directly proportional to ρ and $d\rho/dt$, respectively. Also, the flow stress at each time step, σ , is taken to be proportional to the square root of the average dislocation density $(\rho_A)^{1/2}$, with $\rho_A = (\sum \rho^C)/(490^2)$.

The CA model comprehensively predicted the following experimentally observed features of DRX: (1) necklace type microstructures at high strain rates, (2) kinetics of DRX that obey the JMAK equation with an Avrami exponent of $k=1.4-1.6$, (3) an increase in the volume fraction recrystallized at the peak stress with increasing strain rates, (4) the ratio of the strain at the onset of recrystallization to the strain at the peak stress, ϵ_{CR}/ϵ_P , varied from 0.57 to 0.88, (5) a deviation in the strain hardening rate versus stress curve at the onset of DRX, and (6) a transition from single to multipeak flow curves at $D_O/D_{SS} = 2$. Also, the probability of nucleation at the onset of DRX was twice the probability for nucleation at steady state. This work was published in *Scripta Materialia* by Goetz and Seetharaman [27].

2.7.3 Dynamic Globularization of Lamellar Structures in a Near Gamma Titanium Aluminide Alloy

The kinetics of dynamic globularization of the lamellar microstructures and the associated flow softening behavior during hot working of a near gamma titanium aluminide alloy were investigated. Isothermal compression tests were conducted on specimens of Ti-45.5Al-2Nb-2Cr containing fully lamellar microstructures at 1093 °C to 1204 °C and strain rates ranging from 0.001 to 1.0 s⁻¹. Both the peak stress and flow-softening rate were strongly dependent on the test temperature and the strain rate. Microbuckling of the lamellae in the interior regions of the grains and the formation of fine, equiaxed grains at the grain boundaries constituted the major microstructural changes during hot deformation. The kinetics of the dynamic globularization

process and its influence on the flow stress of the alloy were interpreted via numerical simulation of the coupled plastic flow and globularization processes using a finite element model.

2.7.3.1 Modeling Globularized, Fully Lamellar TiAl using DEFORMTM and CA

Work was initiated to model the deformation and globularization of fully lamellar TiAl. One goal was to predict flow curves under hot-working conditions as a function of prior alpha grain size. For large prior grain sizes (200 to 900 μm), severe flow softening occurs before globularization. Initially, a CA generated microstructure was input to DEFORMTM with randomly assigned lamellar orientations surrounded by globularized γ grains. A constant power-law equation with flow stress as a function of strain rate was assigned to each lamellar orientation using a parabolic relationship. As expected, large strains occurred in softer grains of 45° lamellar orientation. However, the flow curve exhibited strain hardening, not softening, due to the power-law, flow stress relationship. To avoid a constant flow stress relationship and account for the local rotations inside grains, DEFORMTM was modified so that as each element rotates, the flow stress changes depending on the initial assigned lamellar orientation. Preliminary results exhibited some kinking of the lamellae in the interior of grains (also shown experimentally) and a constant flow curve.

The effect of the volume fraction of a soft phase ($\sigma = 50$ MPa) on the flow curve was examined. The flow stress with a 0 percent volume fraction soft phase was 640 MPa: 8 percent - 640 MPa, 32 percent - 430 MPa, 47 percent - 320 MPa, 81 percent - 120 MPa, 95 percent - 84 MPa, and 100 percent - 59 MPa. The flow stress is 59 MPa with 100 percent soft phase rather than 50 MPa as listed above because of the plain-strain state of stress. From the distortion energy criterion, the yield stress of a material in plane strain is $2/\sqrt{3}$, or 1.155 the yield stress in uniaxial compression, although the value here is 1.18.

The work modeling the deformation and globularization of fully lamellar TiAl using DEFORMTM and CA continued in three areas: First, the DEFORMTM flow stress subroutine for lamellar and globularized TiAl was modified to incorporate flow stress as a function of changes in lamellar angles during deformation. Several simulations were performed with realistic distributions of lamellar angles and grain sizes (80, 100, 200, and 900 μm) corresponding to experimental compression tests at 1093 °C and 1.0 s^{-1} . The resulting flow curves for the various grain sizes correlated with the peak stresses of the experimental curves, Figure 1a. The results also correlated with experimental observations of increasing peak stresses with increasing grain size. Histograms of the lamellar angles after deformation exhibited a more uniform distribution than the initial distribution. Second, to determine the relationship between flow stress, lamellar angle, and volume fraction globularized, three curves of flow stress versus volume fraction globularized were produced. The three curves corresponded to three initial lamellar angles and corresponding flow stresses: 0° - 600 MPa, 45° - 300 MPa, and 90° - 1000 MPa. The flow stress of the globularized regions was 250 MPa for all three cases, and the flow stress of the lamellar regions was held constant neglecting changes in flow stress due to changes in lamellar angle during deformation. Third, to determine the amount of flow softening due to globularization and changes in lamellar angle, a simulation was conducted with a realistic distribution of lamellar angles (and in turn flow stresses) and grain sizes. The average grain size and grain density corresponds to that of the 900- μm grain size compression specimens. Globularization was set to

occur when local strains equaled or exceeded 0.3. The resulting flow curve and flow softening correlated with the experimental flow curve, Figure 1b, which had been corrected for deformation heating.

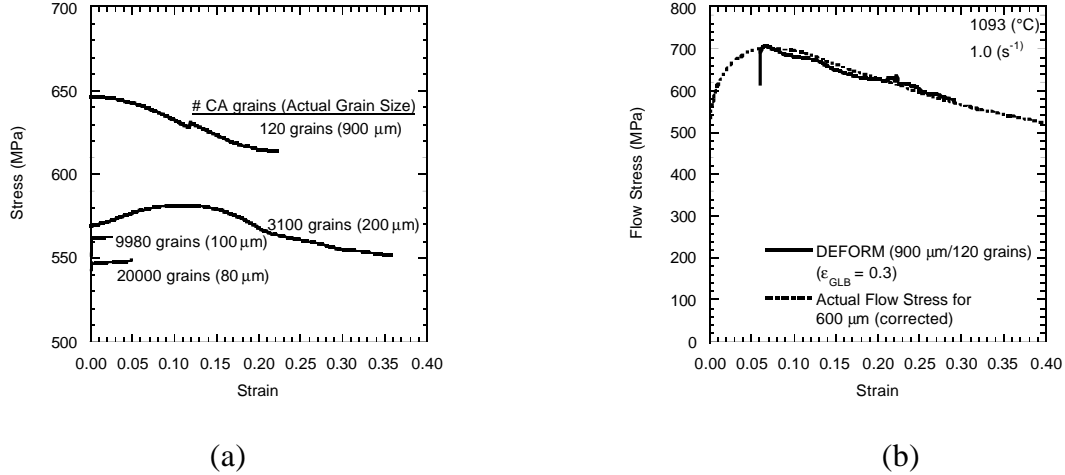


Figure 1: DEFORM™ simulations for globularization modeling

Note: (a) realistic distributions of lamellar angles and grain sizes (80, 100, 200, and 900 μm) corresponding to experimental compression tests at 1093 $^{\circ}\text{C}$ and 1.0 s^{-1} ,
 (b) globularization set to occur when local strains equaled or exceeded 0.3

Flow stress versus strain curves for fully lamellar TiAl were corrected for deformation heating, Figure 2. The flow curves were for an initial lamellar grain size of 600 μm , at 1093, 1148, and 1204 $^{\circ}\text{C}$, and compressed at strain rates of 0.001, 0.1, and 1.0 s^{-1} . The uncorrected flow curves appear in the paper published in *Metallurgical and Materials Transactions A* titled, “Effect of the Lamellar Grain Size on Plastic Flow Behavior and Microstructure Evolution during Hot Working of a Gamma Titanium Aluminide Alloy” by Seetharaman and Semiatin [28]. The method used to correct the curves involved the traditional method of calculating the temperature rise in the compression specimen using the area under the uncorrected curve, the adiabatic correction factor, η , and the temperature sensitivity of the flow stress, $d\sigma/dT$. As a check, these first generation corrected curves were used in nonisothermal DEFORM™ simulations of the compression test for each temperature and strain rate. If flow stress curves have been accurately corrected for deformation heating, the load/stroke curves taken from DEFORM™ simulations and converted to stress/strain curves should match the uncorrected experimental flow stress curves. The first generation corrected curves did not match and it was found that η is a function of strain as well as strain rate [Sec. 2.9.1]. Also, the values of $d\sigma/dT$ were not constant throughout the temperature range as originally assumed, but decrease significantly at 1204 $^{\circ}\text{C}$. It was also necessary to extrapolate beyond the lower and upper limits of strain rate and temperature to provide flow stress data outside the original database due to deformation heating and strain rate effects. This work was presented and published in the conference proceedings at *The Fourth International Conference on Recrystallization and Related Phenomena* by Seetharaman, Goetz, and Semiatin [29].

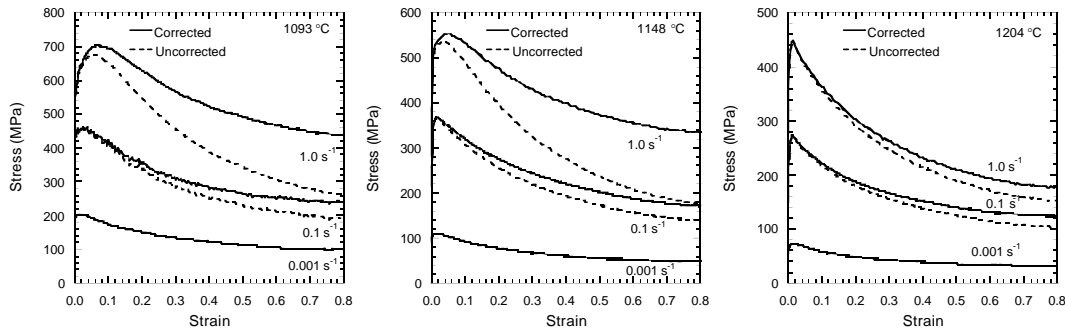


Figure 2: The Flow Curves were for an Initial Lamellar Grain Size of 600 μm , at 1093, 1148, and 1204 $^{\circ}\text{C}$, and Compressed at Strain Rates of 0.001, 0.1, and 1.0 s^{-1}

2.8 Published Research on Other Modeling

2.8.1 A Theoretical Investigation of the Effect of Materials Properties and Cavity Architecture/Shape on Ductile Failure During the Hot Tension Test

The effect of material properties and cavity architecture, shape, and orientation on ductile failure behavior during hot tension testing was established using a numerical analysis of the deformation of a representative microspecimen. The microspecimen consisted of two regions, or slices, one containing the cavities and the other comprising a uniform, cavity-free area. The cavities were assumed to be spherical or cylindrical and to form a simple cubic (sc), body-centered cubic (bcc), or face-centered cubic (fcc) network; tensile loading was taken to be parallel to either the cube edge, face diagonal, or body diagonal. By invoking load equilibrium, expressions describing the relation between the deformations in the uniform and cavity-containing regions were derived. The principal material-related coefficients in these equations were a geometry factor G , whose value depended on the specific cavity architecture and tensile loading direction, the strain-hardening and strain-rate sensitivity exponents n and m , and the parameter η , used to describe the (volumetric) cavity growth kinetics. For cylindrical cavities, the pertinent void-growth parameter was deduced to be the area cavity growth rate η_A . Failure was predicted to be either retarded or accelerated when η_A is less than or greater than $2\eta/3$, respectively. The simulations were used to quantify the microscopic strain localization kinetics and, thus, to identify those deformation regimes in which void growth versus void coalescence (i.e., internal necking) predominates during the ductile failure process. Model predictions of tensile elongation were validated by comparison with experimental measurements for cavitating materials found in the literature. This work was published in *Metallurgical and Materials Transactions A* by Nicolaou and Semiatin [30].

2.8.2 An Analysis of the Effect of Cavity Nucleation Rate and Cavity Coalescence on the Tensile Behavior of Superplastic Materials

A model utilizing a simple force-equilibrium approach was developed to establish the effect of the cavity nucleation rate and cavity coalescence on the uniaxial tensile behavior of superplastic metals. All cavities were assumed to be spherical and uniformly distributed within the material,

irrespective of the degree of deformation. Material input parameters for the model comprised the cavity nucleation rate (N), the strain-rate sensitivity of the flow stress (m), and the growth parameter for individual cavities (h), which was taken to be a function of m . The effect of cavity coalescence on average void size and volume fraction was treated using an empirical relation, which correlates an average void growth rate to the growth rate of individual, noninteracting cavities. Model predictions indicated that the macroscopic quantities often used to describe cavitation behavior, i.e., initial cavity volume fraction (C_{n0}) and apparent cavity growth rate (η_{APP}) describe the combined influence of cavity nucleation, growth, and coalescence. With regard to the overall tensile behavior, simulation results revealed that increasing cavity nucleation rates reduce ductility in a manner analogous to the effect of decreases in the strain-rate sensitivity. In addition, the failure mode was established with regard to the relative magnitudes of the cavity nucleation rate and the strain-rate sensitivity. Model predictions of tensile elongation and cavity-size distributions were validated by comparison to measurements found in the literature for cavitating superplastic materials. This work was published in *Metallurgical and Materials Transactions A* by Nicolaou, Semiatin, and Ghosh [31].

2.9 Published Research on Other Work

2.9.1 The Adiabatic Correction Factor for Deformation Heating During the Uniaxial Compression Test

The isothermal uniaxial compression test is a common method for determining the flow stress of metals. For accurate flow stress data at strain rates $> 10^{-3} \text{ s}^{-1}$, the data must be corrected for flow softening due to deformation heating. The first step in the correction is to determine the increase in temperature. An adiabatic correction factor, η , is used to determine the temperature between strain rates of 10^{-3} to 10^1 s^{-1} . The adiabatic correction factor is the fraction of adiabatic heat retained in the workpiece after heat loss to the dies, $\eta = (\Delta T_{ACTUAL})/(\Delta T_{ADIABATIC})$, where $\Delta T_{ADIABATIC} = (0.95 \int \sigma d\epsilon)/(\rho C_p)$. η is typically taken to be constant with strain and vary linearly (0 to 1) with $\log(\dot{\epsilon})$ between 10^{-3} s^{-1} and 10^1 s^{-1} . However, using the FEM and a one-dimensional, lumped parameter method, η was found to vary with strain, die and workpiece thermal conductivities, and the interface heat transfer coefficient (HTC). Using the lumped parameter method, an analytical expression for η was derived. In this expression, η is a function of the die and workpiece thermal conductivities, the HTC, workpiece heat capacity, strain, and strain rate. The results show that an increase in the HTC or thermal conductivity decreases η . This work was published in *Journal of Materials Engineering and Performance* by Goetz and Semiatin [32].

2.9.2 Development of Nickel Alloy Substrates for Y-Ba-Cu-O Coated Conductor Applications

Fabrication of long-length, textured substrates constitute a critical step in the successful application of coated high-temperature superconductors. Substrate materials stronger than nickel are needed for robust applications, while substrates with nonmagnetic characteristics are preferred for alternating current applications. This work focused on the development of texture in high strength, nonmagnetic substrate materials. As the development of cube texture is easier in medium to high stacking fault energy materials, binary alloys based on nickel were evaluated for

the present application. High purity alloys were melted and hot/cold worked to obtain thin tapes. The development of texture in these alloys as a function of processing parameters was studied by XRD and metallographic techniques. Orientation imaging microscopy (OIM) was used to quantify the extent of texture development in these substrates. Results to date on the development of texture by thermomechanical processing of these alloys are presented. This work was published in *IEEE Transactions on Applied Superconductivity* by Nekkanti, Seetharaman, Brunke, Maatense, Dempsey, Kozlowski, Tomich, Biggers, Peterson, Barnes and Oberly [33].

3 UNPUBLISHED RESEARCH

3.1 Characterization of the Forging Die Workpiece Interface Friction and Heat Transfer Between Alloy Steel and Alloy Ti-6Al-4V

3.1.1 Introduction

A joint USAF/Navy program awarded two teams, Pratt & Whitney (P&W) and General Electric (GE) Aircraft engines, a 1-year Phase I contract under the Joint Forging Supplier Initiative. The goal of the Joint Forging Supplier Initiative was to lower the cost of aerospace forgings by 35 to 40 percent. Concurrent Technologies Corporation (CTC) supported both teams in this effort with management responsibilities of a Navy MANTECH project titled, "Forging Supplier Initiative Support," under the National Center for Excellence in Metalworking Technology Government Prime Contract.

In support of this project, CTC contracted UES to determine the interface HTC and the friction factor (m). The goal of this task was to improve the knowledge base of workpiece-die interface conditions thereby improving the accuracy of computer simulations of forging processes. More accurate computer simulations will reduce costs by allowing greater reliance on simulations than on trial and error.

This work was conducted by UES through a Cooperative Research and Development Agreement (CRADA No. 99-025-ML-01) at the Materials Processing Laboratory (MPL) of the Air Force Research Laboratory, Materials and Manufacturing Directorate (AFRL/MLLM).

The objective of this work was to determine the HTC and the friction factor, m , at the interface between a Ti-6Al-4V workpiece and H13 tool steel die for various combinations of lubricants and workpiece-die temperatures. The ring test was used to determine friction factors and HTCs under nonisothermal conditions using thermocoupled dies to measure the heat transfer from the Ti-6Al-4V ring to H13 dies. FEM software was used to generate nonisothermal calibration curves for the determination of friction factors and HTCs. In addition to the ring tests, uniaxial compression tests of Ti-6Al-4V cylinders were performed to measure the flow stress at the strains, strain rates, and temperatures that the rings were subjected to during the tests. Accurate flow stress data is necessary for the FEM simulations used to generate calibration curves. This work was detailed in a report by Barker, Goetz and Fagin [34].

3.1.2 Experimental Procedure

The determination of friction factors and HTCs using the ring test requires calibration curves upon which experimental measurements are plotted to determine either the friction factor or the HTC. For the friction factor, calibration curves are plots of % Reduction in Minimum Internal Diameter versus the % Reduction in Height for a constant friction factor (m), with a single curve for each value of m . The experimental ring measurements of % Reduction in Minimum Internal Diameter and % Reduction in Height are then plotted, and the friction factor is determined by which calibration curve the experimental points fall upon. For the HTC, the calibration curves are Temperature versus Time curves at various locations in the dies, with a single curve for a

constant value of die/ring HTC. As with the friction factor curves, the HTC is determined by plotting the experimental temperature versus time curves on the calibration curves, and determining the HTC by which calibration curve the experimental curve falls upon.

The generation of the calibration curves requires knowledge beforehand of ring metal flow and die temperatures during the test for different friction factors and HTCs. Due to the highly nonlinear nature of the nonisothermal ring test, generation of the calibration curves requires FEM simulations of the process.

3.1.3 Compression Testing

Before FEM simulations can be done, accurate flow stress data of the material involved is required. Uniaxial compression tests of Ti-6Al-4V cylinders were performed to measure the flow stress at the strains, strain rates, and temperatures that the rings undergo during ring tests. These cylinders were machined from the same starting material as the rings for the ring test. The compression test conditions were strain rates of 0.1 and 1.0 s⁻¹, temperatures of 400, 676, 815, 954, and 1037 °C, and true plastic strains of 0.0 to 0.5. The 400 °C tests were performed due to the expectation that low-temperature/low-strain-rate ring tests will chill to around 400 °C.

Compression tests were performed at a constant strain rate on a 55 kip MTS-810 servo-hydraulic test machine with SiN platens. The samples at 676, 815, 954, and 1037 °C were induction heated, with the test temperature controlled by attaching a type-K thermocouple to the sample. The samples at 400 °C were heated using band heaters attached to H13 tool steel dies, with the temperature also controlled by thermocoupling the sample. The samples were soaked for 10 minutes before testing.

The tests were conducted in an air atmosphere, although the samples were protected from oxidation by a glass lubricant on all surfaces. The samples were sandblasted and coated with one of three glass lubricants depending on the test temperature: 1037 °C – Deltaglaze 349, 815 °C and 954 °C – Corning Glass 8871, and 400 °C - Oil-Dag. The choice of lubricant was made based on past experience as to which one gives the best lubrication and least barreling of the sample. There is a certain temperature range that each glass is applicable. The sample dimensions were 0.5 inch diameter by 0.625 inch height (12.7 mm by 15.87 mm). The load versus displacement curves were converted to stress versus strain curves after compensating for machine compliance. The stress versus strain curves were then compensated for deformation heating. The Ti-6Al-4V flow stress from these compression tests can be found in Table 1 and Table 2.

3.1.4 Ring Tests

The ring tests were performed on a 200 kip servo-hydraulic press between H13 tool steel dies heated to the prescribed die temperatures of either 260 or 427 °C using band heaters, Figure 3. The top die was instrumented with six thermocouples, two thermocouples at each of three distances from the die surface: 0.025, 0.050, and 0.100 inch, equally spaced around a 1.2-inch-diameter circle. The thermocouple temperatures, load, ram displacement, and time were collected and stored by a Pentium III PC with Labtech software. The press was controlled with an MTS controller at constant strain rates of 0.1 and 1.0 s⁻¹. The ring dimensions were: outside

diameter (O.D.) – 1.5 inch, inside diameter (I.D.) – 0.75 inch, height – 0.50 inch, for an O.D. to I.D. to height ratio of 6:3:2.

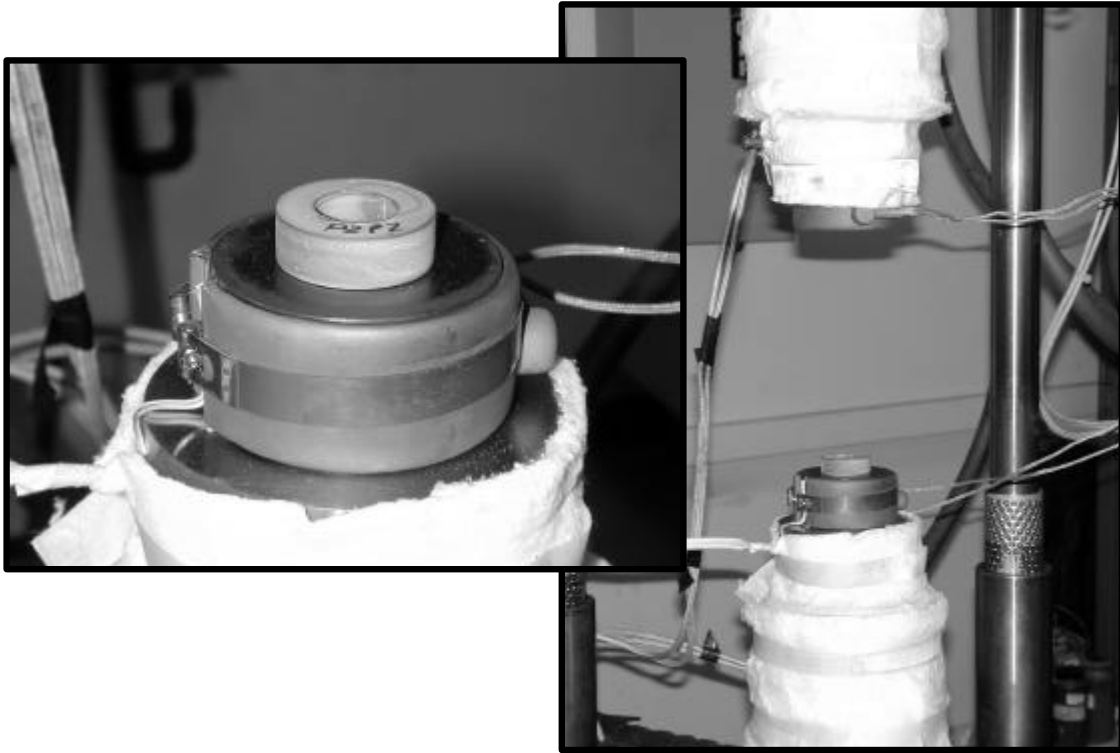


Figure 3. Ring Test Setup

Each ring was sand blasted and coated with a glass lubricant, Deltaglaze 153, while the die surfaces were cleaned before each test and coated with one of three die lubricants (Deltaforge F-31, Oil-Dag, and GP-200) using an air brush. The rings were preheated to the prescribed test temperature [676 °C, 815 °C, 954 °C, or 1037 °C] in a Harrop resistance furnace for 10 minutes prior to the test. The rings were then transferred to the die surface, centered on the die, and either forged to the prescribed reduction (30 or 60 percent), or to the highest reduction allowed given the maximum press load limit of 200 kip. The average time to transfer a ring from the furnace to the die surface was three seconds. The average dwell time on the bottom die before forging was 2.5 seconds. This 2.5 seconds includes the time to center the ring, raise the bottom die to contact the top die, and begin forging. Figure 3 shows the ring test setup with band-heated dies and an unheated glass coated ring.

Ring test conditions and final dimensions are given in Table 3 and Table 4.

Table 1. Ti-6Al-4V Flow Stress @ 0.1s^{-1}

Strain	Flow Stress (MPa)				
	400 °C	676 °C	815 °C	954 °C	1037 °C
0.05	657.00	433.27	239.39	67.844	29.785
0.10	730.00	444.02	227.25	65.569	31.164
0.15	793.00	447.26	219.12	63.570	31.854
0.20	850.00	444.30	212.70	61.777	32.474
0.25	900.00	440.02	208.15	60.191	32.819
0.30	935.00	435.82	204.36	59.019	32.888
0.35	967.00	433.20	202.09	57.709	33.026
0.40	995.00	430.99	199.95	56.813	33.302
0.45	1025.0	430.30	198.64	55.985	33.922
0.50	1050.0	430.30	197.88	55.710	34.060

Table 2. Ti-6Al-4V Flow Stress @ 1.0s^{-1}

Strain	Flow Stress (MPa)				
	400 °C	676 °C	815 °C	954 °C	1037 °C
0.05	694.00	484.49	308.54	98.595	50.125
0.10	770.00	513.18	303.92	96.802	51.780
0.15	835.00	534.27	299.72	94.872	53.641
0.20	880.00	537.38	294.75	93.286	54.262
0.25	935.00	537.65	291.10	91.080	54.744
0.30	980.00	533.79	288.96	90.666	55.572
0.35	1010.0	525.86	285.17	89.287	56.192
0.40	1045.0	516.83	279.72	88.805	56.744
0.45	1070.0	511.87	278.89	88.115	56.813
0.50	1100.0	506.01	275.24	88.529	57.433

Table 3. Ring Test Data: Tests 1 through 48 (815 °C - 1037 °C)

Test #	Height (in.)	I.D. (in.)	Set % Red. Height	Actual % Red. Height	% Red. I.D.	Lubricant	Strain Rate (s ⁻¹)	Ring Temperature (°C)	Die Temperature (°C)	Friction Factor, M	
1	0.383	0.74	30	23.4	1.3	F-31	0.1	815	260	0.14	
2	0.379	0.745	60	24.2	0.67	F-31	0.1			0.14	
3	0.381	0.715	30	23.8	4.67	Oil-Dag	0.1			0.17	
4	0.383	0.71	60	23.4	5.33	Oil-Dag	0.1			0.17	
5	0.381	0.705	30	23.8	6.00	GP-200	0.1			0.19	
6	0.385	0.705	60	23.0	6.00	GP-200	0.1			0.19	
7	0.368	0.665	30	26.4	11.33	F-31	0.1	954		0.14	
8	0.31	0.635	30	38.0	15.33	F-31	1.0			0.08	
9	0.349	0.655	60	30.2	12.67	F-31	0.1			0.17	
10	0.212	0.478	60	57.6	36.27	F-31	1.0			0.12	
11	0.37	0.659	30	26.0	12.13	Oil-Dag	0.1			0.16	
12	0.312	0.577	30	37.6	23.07	Oil-Dag	1.0			0.12	
13	0.35	0.654	60	30.0	12.80	Oil-Dag	0.1			0.17	
14	0.215	0.45	60	57.0	40.00	Oil-Dag	1.0			0.13	
15	0.37	0.65	30	26.0	13.33	GP-200	0.1			0.18	
16	0.311	0.525	30	37.8	30.00	GP-200	1.0			0.15	
17	0.353	0.64	60	29.4	14.67	GP-200	0.1			0.19	
18	0.22	0.342	60	56.0	54.40	GP-200	1.0			0.18	
19	0.364	0.6	30	27.2	20.00	F-31	0.1			1037	0.2
20	0.3	0.433	30	40.0	42.27	F-31	1.0				0.15
21	0.344	0.595	60	31.2	20.67	F-31	0.1	0.2			
22	0.209	0.15	60	58.2	80.00	F-31	1.0	0.21			
23	0.363	0.608	30	27.4	18.90	Oil-Dag	0.1	0.17			
24	0.301	0.445	30	39.8	40.67	Oil-Dag	1.0	0.15			
25	0.347	0.611	60	30.6	18.53	Oil-Dag	0.1	0.16			
26	0.209	0.16	60	58.2	78.67	Oil-Dag	1.0	0.21			
27	0.369	0.594	30	26.2	20.80	GP-200	0.1	0.29			
28	0.304	0.453	30	39.2	39.60	GP-200	1.0	0.15			
29	0.354	0.59	60	29.2	21.33	GP-200	0.1	0.28			
30	0.212	0.15	60	57.6	80.00	GP-200	1.0	0.21			
31	0.342	0.673	30	31.6	10.267	F-31	0.1	954	427	0.11	
32	0.301	0.66	30	39.8	12.00	F-31	1.0			0.09	
33	0.304	0.65	60	39.2	13.33	F-31	0.1			0.14	
34	0.191	0.612	60	61.8	18.40	F-31	1.0			0.08	
35	0.342	0.65	30	31.6	13.33	Oil-Dag	0.1			0.14	
36	0.302	0.712	30	39.6	5.07	Oil-Dag	1.0			0.07	
37	0.304	0.677	60	39.2	9.73	Oil-Dag	0.1			0.11	
38	0.196	0.615	60	60.8	18.00	Oil-Dag	1.0			0.08	
39	0.343	0.655	30	31.4	12.67	GP-200	0.1			0.13	
40	0.303	0.703	30	39.4	6.27	GP-200	1.0			0.07	
41	0.304	0.665	60	39.2	11.33	GP-200	0.1			0.12	
42	0.196	0.626	60	60.8	16.53	GP-200	1.0			0.08	
43	0.353	0.775	30	29.4	-3.33	F-31	0.1	815		0.11	
44	0.324	0.78	60	35.2	-4.00	F-31	0.1			0.11	
45	0.352	0.77	30	29.6	-2.67	Oil-Dag	0.1			0.11	
46	0.328	0.765	60	34.4	-2.0	Oil-Dag	0.1			0.12	
47	0.354	0.765	30	29.2	-2.00	GP-200	0.1			0.12	
48	0.324	0.775	60	35.2	-3.33	GP-200	0.1			0.11	

Table 4. Ring Test Data: Tests 49 through 60 (676 °C)

Test #	Height (in.)	I.D. (in.)	Set % Red. Height	Actual % Red. Height	% Red. I.D.	Lubricant	Strain Rate (s ⁻¹)	Ring Temperature (°C)	Die Temperature (°C)	Friction Factor, M
49	.309	.824	30	38.2	-9.87	F-31	1.0	676	427	0.08
50	.338	.794	30	32.4	-5.87	F-31	0.1			0.13
51	.309	.789	30	38.2	-5.20	Oil-Dag	1.0			0.11
52	.339	.780	30	32.4	-4.00	Oil-Dag	0.1			0.14
53	.309	.787	30	38.2	4.93	GP-200	1.0			0.11
54	.339	.775	30	32.4	-3.33	GP-200	0.1			0.15
55	.342	.803	30	31.6	-7.07	F-31	1.0		260	0.08
56	.380	.800	30	24.0	-6.67	F-31	0.1			0.09
57	.346	.668	30	30.8	10.93	GP-200	1.0			0.25
58	.384	.727	30	23.2	3.07	GP-200	0.1			0.23
59	.341	.655	30	31.8	12.67	Oil-Dag	1.0			0.25
60	.380	.750	30	24.0	0.00	Oil-Dag	0.1			0.18

3.1.5 FEM

The ring test has traditionally been used to determine the interface friction factor under isothermal conditions only. Upper bound methods, and then early FEM codes, were used to generate the calibration curves needed to determine friction factors. However, to determine friction factors and HTC's using a nonisothermal ring test, as used in this work, requires FEM software capable of accurately predicting ring dimensions and die temperatures throughout the test for various HTC's and friction factors, Figure 4. This also requires material flow stress as a function of strain, strain rate, and temperature for the range of strains, strain rates, and temperatures encountered throughout the test.

The FEM software that was used for this work is DEFORM™, a product of Scientific Forming Technologies Corporation of Columbus, Ohio. Key features of this code are: 2-D (axisymmetric or plane strain) and 3-D analysis, three analysis modes (isothermal, nonisothermal, heat transfer), multiple deforming objects, four deformation behaviors (plastic, elastic, porous-plastic, rigid), automatic mesh generation, and automatic remeshing of deformed objects.

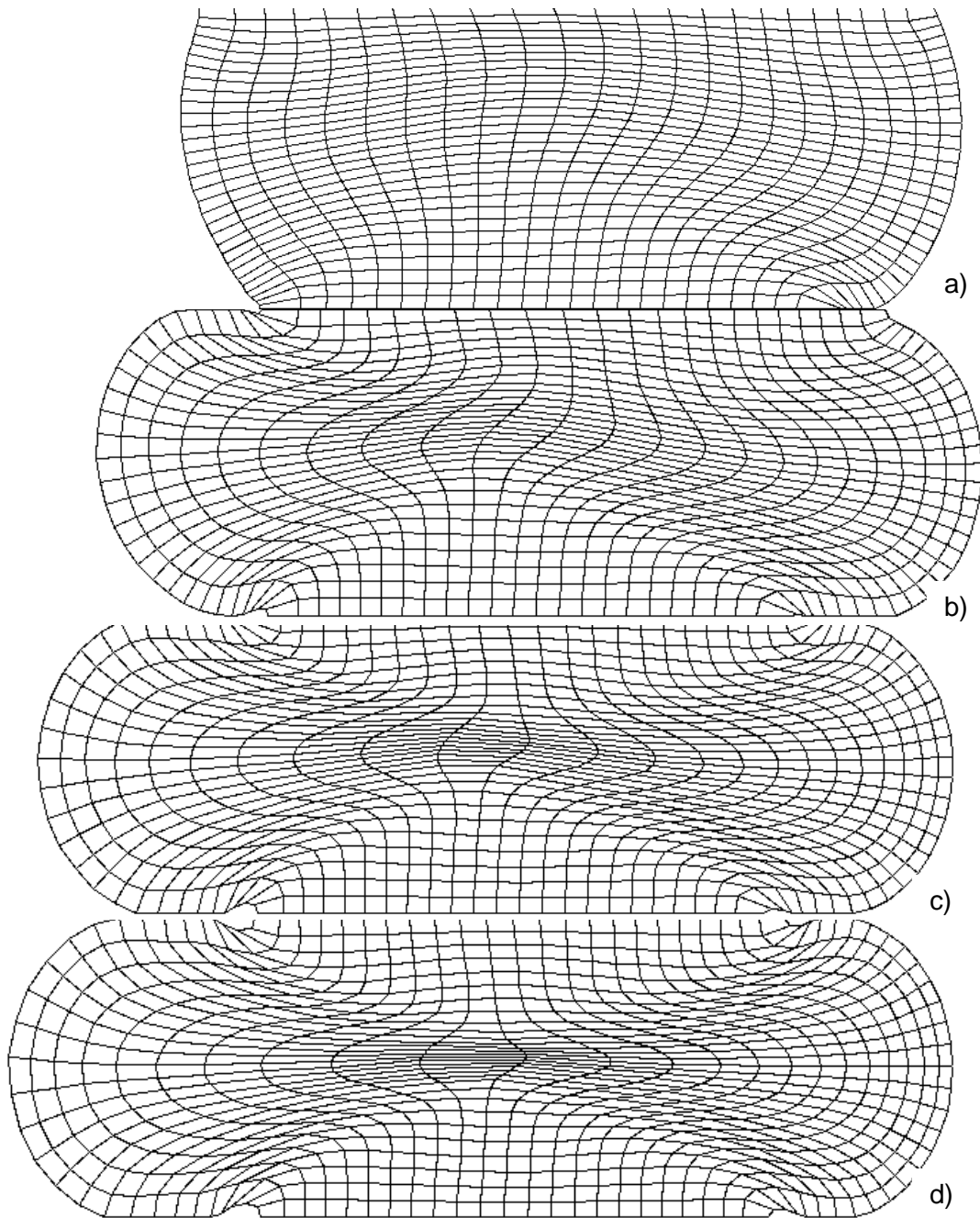


Figure 4. DEFORM™ FEM Meshes at 50 Percent Reductions for Various HTCs

Note: (a) 1.0 kW/m²K, (b) 5.0 kW/m²K, (c) 10.0 kW/m²K, and (d) 20.0 kW/m²K. The initial conditions were: Ring Temperature - 1037 °C, Die temperature - 260 °C, Strain Rate - 1.0s⁻¹, and friction factor (m) - 0.10

There are four steps required to determine the HTC and friction factors for the nonisothermal ring test:

1. The FEM code was used to generate HTC calibration curves. These curves are temperature versus time plots at die locations corresponding to the thermocouple locations used in the ring test experiments, with one curve for each position and HTC. For example, see Figure 5. Load versus displacement curves were also used in a similar fashion, Figure 6.
2. The HTCs are determined by plotting the experimental temperature versus time data, or load versus displacement data, on the FEM generated calibration curves, Figure 5 and Figure 6.
3. After determining the HTC for a given combination of ring temperature, die temperature, and strain rate, the HTC is used in FEM simulations to generate friction calibration curves. Table 5 gives the conditions used in these FEM simulations. These curves plot the % Reduction in Minimum Internal Diameter versus % Reduction in Height of a ring. Several curves are generated using various friction factors (m) ranging from 0 to 1. For example, see Figure 7, Figure 8 and Figure 9.
4. The values of m for each ring test are determined by plotting the experimental % Reduction in Minimum Internal Diameter versus % Reduction in Height on the FEM generated calibration curves. The value of m is determined by which curve the experimental point falls on, Figure 9.

Material properties required by DEFORM™ for the Ti-6Al-4V alloy used in the ring tests include: flow stress, thermal conductivity, and heat capacity. All FEM simulations included cooling the ring in air for 3 seconds for the transfer from the furnace to the die followed by a 2.5 seconds dwell on the bottom die before deformation. This accounts for the actual transfer and dwell times.

Figure 10 shows ring temperatures for various combinations of die/ring temperatures and strain rates as a function of HTC, for comparison with thermocoupled ring tests.

Figure 11 shows how the load and temperature recorded during a thermocoupled ring test correspond to the load and temperature predicted by an FEM simulation using the friction factor and HTC determined by the above method.

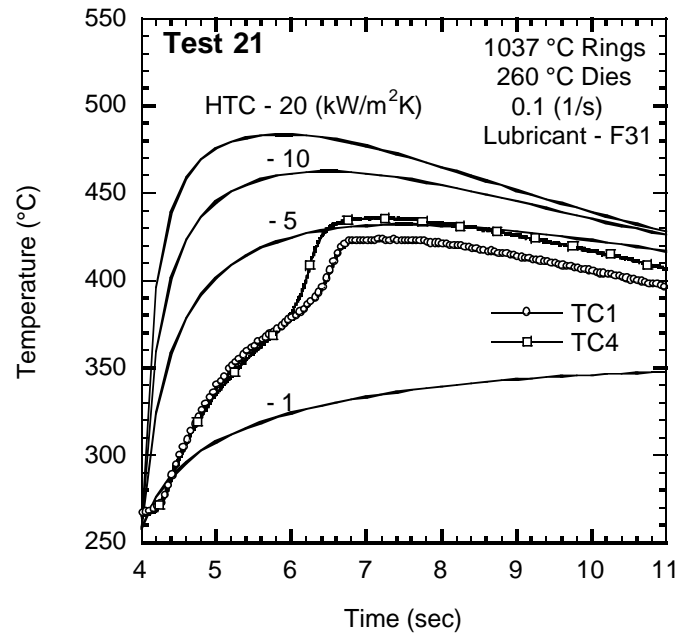


Figure 5. HTC ($\text{kW/m}^2\text{K}$) Calibration Curves for Test 21

Note: Thermocouples #1 and #4 are 0.025 in. from the die surface.

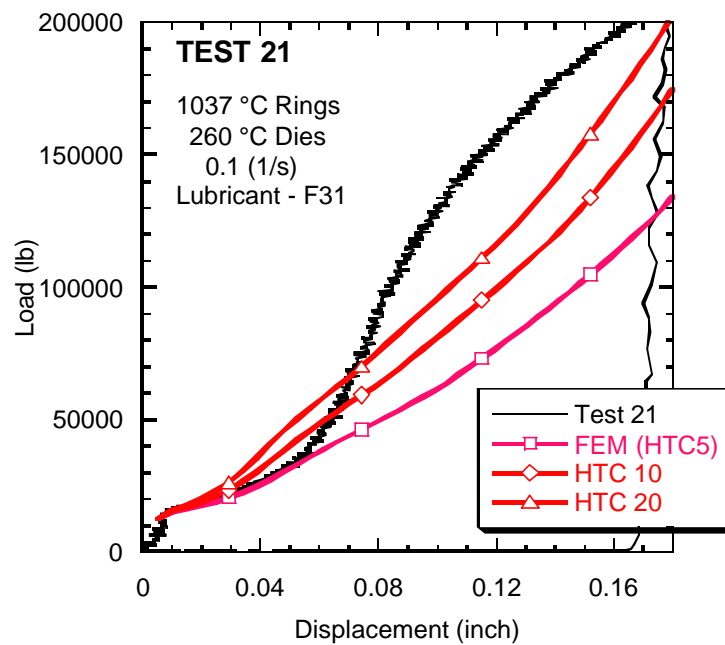


Figure 6. Load versus Displacement Curves Comparing FEM Curves to Experimental Curve for Test 21 (HTCs, $\text{kW/m}^2\text{K}$)

Table 5. Interface HTC's used in FEM Simulations for Friction Factor Calibration Curve Generation

Ring Temperature (°C)	Ring Temperature (°C)	Strain Rate (s-1)	HTC-Interface Heat Transfer Coefficient (kW/m ² K)	
2.5 (sec) Dwell on Bottom Die			0.35	
676	260	0.1	20	
676	260	1.0	20	
676	427	0.1	20	
676	427	1.0	20	
815	260	0.1	20	
815	427	0.1	10	
954	260	1.0	10	
954	427	0.1	10	
954	427	1.0	10	
1037	260	1.0	10	
954	260	0.1	Varied with time	
			Time (s)	HTC
			0.0	5
			1.7	5
			2.25	10
1037	260	0.1	6	20

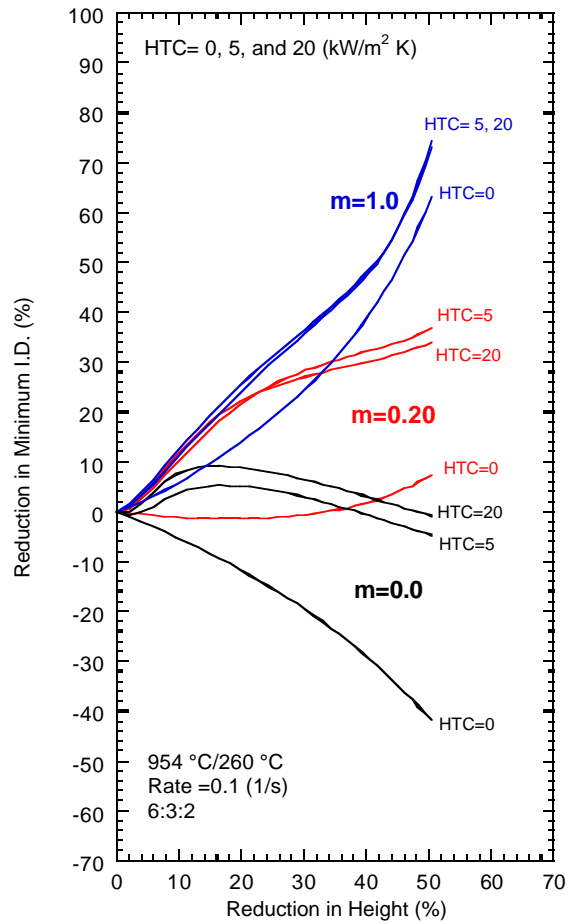


Figure 7. Effect of the HTC on the Friction Calibration Curves

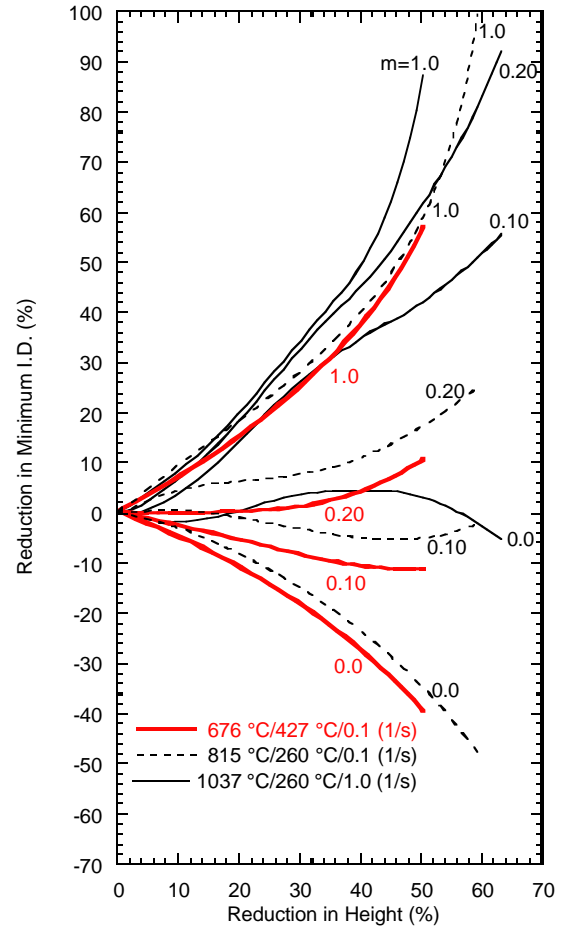


Figure 8. Effect of Test Temperatures and Strain Rates on Friction Calibration Curves

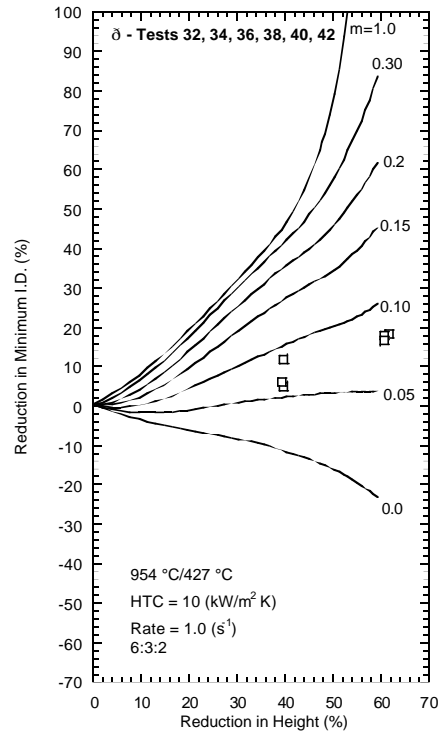


Figure 9. Nonisothermal Friction Calibration Curves

3.1.6 Summary of Results

- The HTC from the load versus displacement curves ranged from an initial value of 5.0 kW/m²K for low strains to a final value of 20.0 kW/m²K at the end of the test. For the 815 °C ring/427 °C die/0.1 s⁻¹ test and all 676 °C tests, the HTC was a constant 20.0 kW/m²K.
- The HTCs derived using temperature versus time curves from the dies and tests with thermocoupled rings were 1.9 - 5.0 kW/m²K. These HTCs are lower than those shown by the load versus displacement curves are. The load versus displacement curves are a more reliable indicator of instantaneous ring temperature, and therefore were the primary method of determining the HTC for the friction calibration curves.
- There is little difference between friction calibration curves with HTCs between 5.0 and 20.0 kW/m²K.
- The friction factors (m) ranged from a low of 0.07 to a high of 0.21 or 0.29 for all three-die lubricants (F-31, Oil-Dag, and GP-200). Table 6, Table 7 and Table 8 give the friction factor, m, at each test condition, grouped by lubricant.
- The average friction factor for all tests and lubricants was 0.15 with a standard deviation of 0.05. The average values and standard deviations for each lubricant were: F-31 – 0.13 (0.04), Oil-Dag – 0.15 (0.04), and GP-200 – 0.17 (0.06).

- The test conditions of 954 °C rings/427 °C dies/1.0 s⁻¹ resulted in uniformly low friction factors (0.07 to 0.09) for all three lubricants. It was also noted that the forged rings retained a glossy appearance denoting the glass lubricant was maintained throughout the test.
- These test conditions were noted by good surface appearance and friction factors of 0.07 to 0.15: 815 °C ring/427 °C die/0.1s⁻¹, 954 °C ring/427 °C die/0.1s⁻¹, 954 °C ring/260 °C die/1.0s⁻¹, 1037 °C ring/260 °C die/1.0s⁻¹ (#20,24,28), 954 °C ring/427 °C die/1.0s⁻¹.
- The lubricant F-31 frequently yielded the lower friction factor and GP-200 yielded the highest, although the differences were often well within experimental error.
- As expected, the glass ring lubricant, Deltaglaze 153, is not applicable for 676 °C due to poor adhesion and viscosity.
- The friction factors for Oil-Dag (0.18 and 0.25) and GP-200 (0.23 and 0.25) for both 676 °C ring/260 °C die tests were significantly larger than those of F-31 (0.09 and 0.08), while the 676 °C ring/427 °C die tests were more uniform, 0.1s⁻¹ (0.13 to 0.15), 1.0s⁻¹ (0.08 to 0.11).

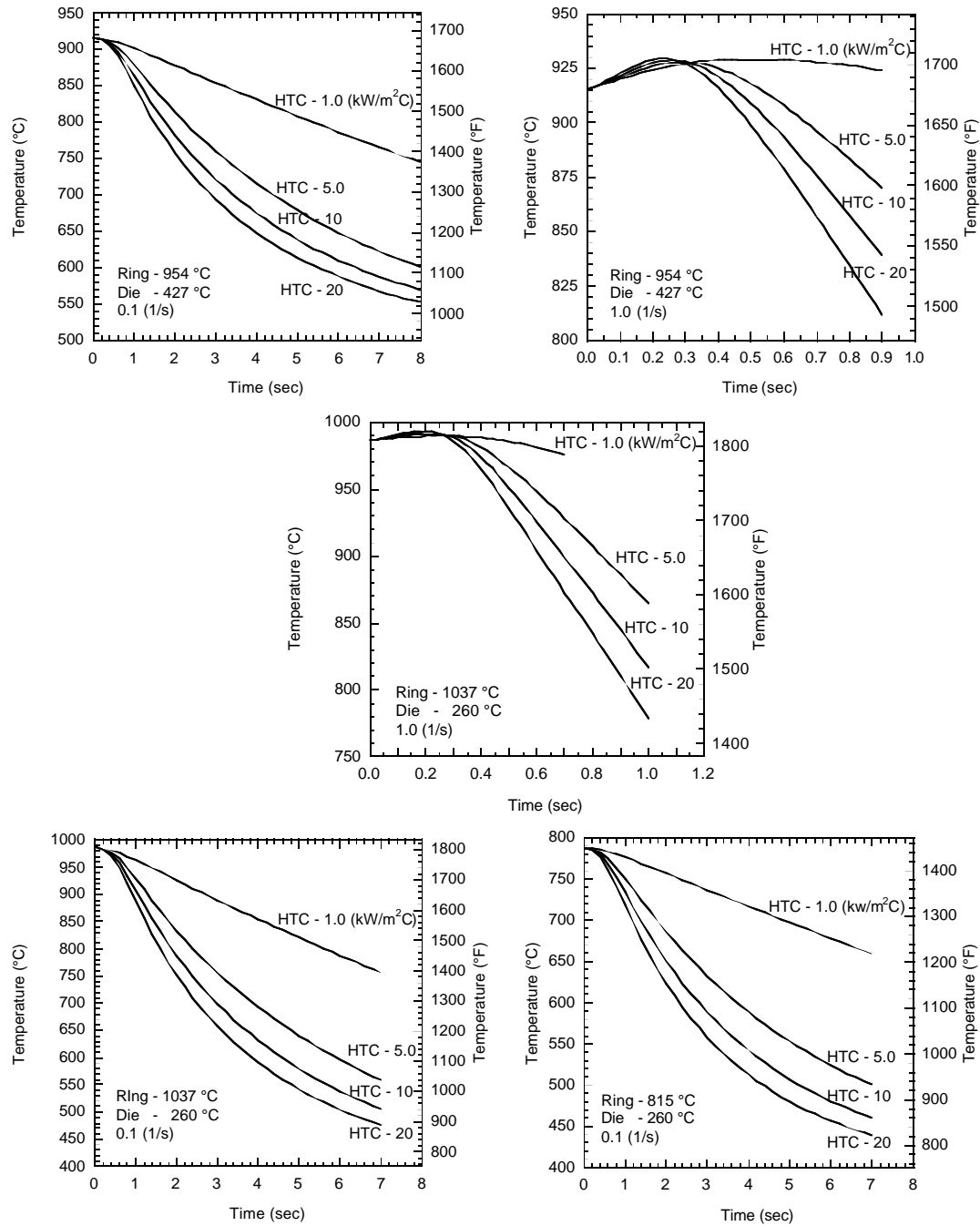


Figure 10. FEM Temperature versus Time Curves from the Center of a Ring

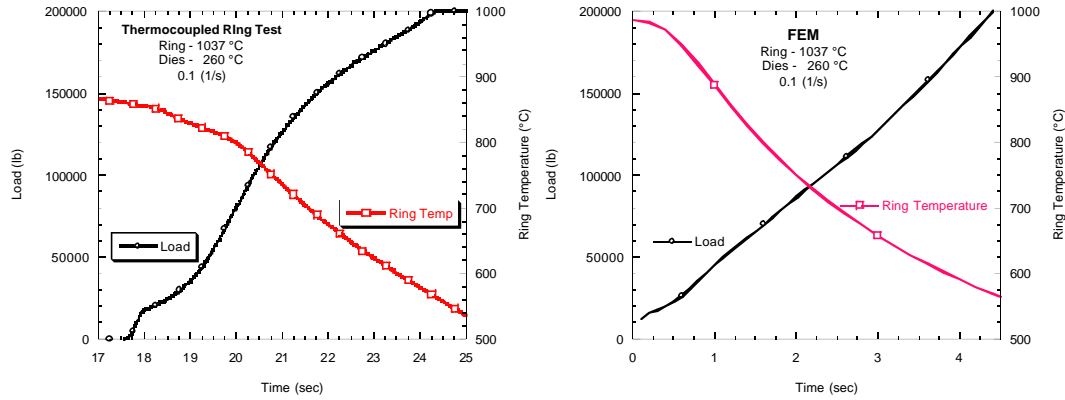


Figure 11. Temperature versus Time and Load versus Time Curves for a Thermocoupled Ring Test and Comparable FEM Simulation (FEM HTC – 20 kW/m²K)

Table 6. Friction Factors for Lubricant – Deltaforge F-31

Lubricant	Test #	Strain Rate (s-1)	Ring Temperature (°C)	Die Temperature (°C)	Friction Factor, M
F-31	55	1	676	260	0.08
F-31	49	1	676	427	0.08
F-31	8	1	954	260	0.08
F-31	34	1	954	427	0.08
F-31	56	0.1	676	260	0.09
F-31	32	1	954	427	0.09
F-31	31	0.1	954	427	0.11
F-31	43	0.1	815	427	0.11
F-31	44	0.1	815	427	0.11
F-31	10	1	954	260	0.12
F-31	50	0.1	676	427	0.13
F-31	1	0.1	815	260	0.14
F-31	2	0.1	815	260	0.14
F-31	7	0.1	954	260	0.14
F-31	33	0.1	954	427	0.14
F-31	20	1	1037	260	0.15
F-31	9	0.1	954	260	0.17
F-31	19	0.1	1037	260	0.2
F-31	21	0.1	1037	260	0.2
F-31	22	1	1037	260	0.21
Average Friction Factor (Standard Deviation)					0.13 (0.04)

Table 7. Friction Factors for Lubricant – Oil-Dag

Lubricant	Test #	Strain Rate (s-1)	Ring Temperature (°C)	Die Temperature (°C)	Friction Factor, M
Oil-Dag	36	1	954	427	0.07
Oil-Dag	38	1	954	427	0.08
Oil-Dag	51	1	676	427	0.11
Oil-Dag	37	0.1	954	427	0.11
Oil-Dag	45	0.1	815	427	0.11
Oil-Dag	12	1	954	260	0.12
Oil-Dag	46	0.1	815	427	0.12
Oil-Dag	14	1	954	260	0.13
Oil-Dag	52	0.1	676	427	0.14
Oil-Dag	35	0.1	954	427	0.14
Oil-Dag	24	1	1037	260	0.15
Oil-Dag	11	0.1	954	260	0.16
Oil-Dag	25	0.1	1037	260	0.16
Oil-Dag	3	0.1	815	260	0.17
Oil-Dag	4	0.1	815	260	0.17
Oil-Dag	13	0.1	954	260	0.17
Oil-Dag	23	0.1	1037	260	0.17
Oil-Dag	60	0.1	676	260	0.18
Oil-Dag	26	1	1037	260	0.21
Oil-Dag	59	1	676	260	0.25
Average Friction Factor (Standard Deviation)					0.15 (0.04)

Table 8. Friction Factors for Lubricant – GP-200

Lubricant	Test #	Strain Rate (s-1)	Ring Temperature (°C)	Die Temperature (°C)	Friction Factor, M
GP-200	40	1	954	427	0.07
GP-200	42	1	954	427	0.08
GP-200	53	1	676	427	0.11
GP-200	48	0.1	815	427	0.11
GP-200	41	0.1	954	427	0.12
GP-200	47	0.1	815	427	0.12
GP-200	39	0.1	954	427	0.13
GP-200	54	0.1	676	427	0.15
GP-200	16	1	954	260	0.15
GP-200	28	1	1037	260	0.15
GP-200	15	0.1	954	260	0.18
GP-200	18	1	954	260	0.18
GP-200	5	0.1	815	260	0.19
GP-200	6	0.1	815	260	0.19
GP-200	17	0.1	954	260	0.19
GP-200	30	1	1037	260	0.21
GP-200	58	0.1	676	260	0.23
GP-200	57	1	676	260	0.25
GP-200	29	0.1	1037	260	0.28
GP-200	27	0.1	1037	260	0.29
Average Friction Factor (Standard Deviation)					0.17 (0.06)

3.2 Process Modeling for Friction Stir Welding for the Metals Affordability Initiative (MAI)

3.2.1 Introduction

Friction stir welding (FSW) is a new solid state welding process that holds considerable promise for practically all aluminum alloys, even precipitation hardened alloys that were previously considered nonweldable. The process entails sinking a rotating pin into the joint until the shoulder of the tool contacts the joint surface. Friction at the tool interface and plastic deformation of the workpiece heats the weld region to temperatures high enough for plastic flow, but below the melting temperature. Once the desired temperature field is created for proper metal flow, the rotating tool is traversed at a constant velocity along the joint. The joint is welded through a process that has been described as a forging and extrusion process in which the weld is created by a stirring action, hence the descriptive name.

Due to the recent and ongoing development of FSW, metal flow around the rotating tool and temperature distributions in the workpiece are not completely understood. Therefore, this project involved the development of a FEM to analyze the temperature distributions and deformation patterns during FSW. This work supported the MAI Core Program titled “Friction Stir Welding of Affordable Lightweight Assemblies” conducted by an industry team headed by The Boeing Company (Boeing) sponsored by the AFRL (contract no. F33615-99-C-5215).

3.2.2 Statement of Work

This work was conducted under Boeing purchase order no. Z00501 and statement of work no. WS-PW-3518 Revision A, which defines the tasks to be conducted as:

A thermal and deformation Finite Element Modeling (FEM) simulation package shall be used to analyze both the transient and steady temperature distributions and deformation patterns within the weld and heat affected zones using appropriate boundary and initial conditions. Results shall include:

1. Develop and test 2D DEFORM™ FEM model
2. Develop and test 3D DEFORM™ FEM model

Input for the model, including the constitutive equations and the thermophysical properties of the material at high temperatures shall be taken from credible technical literature and/or shall be experimentally determined. Sources of key elements shall be identified in documentation.

Progress and data shall be shared with Boeing as it is developed, per mutual agreement with the Boeing technical point of contact.

3.2.3 Results and Discussion

The following results deal with preliminary 2-D simulations for: (1) isothermal/plane-strain simulation of material flow around the FSW pin, and (2) nonisothermal/axisymmetric simulation of the initial tool plunge into the workpiece. The workpiece material for both simulation conditions was 1100 Al. Figure 12 shows the 1100 Al flow stress curves used for this work.

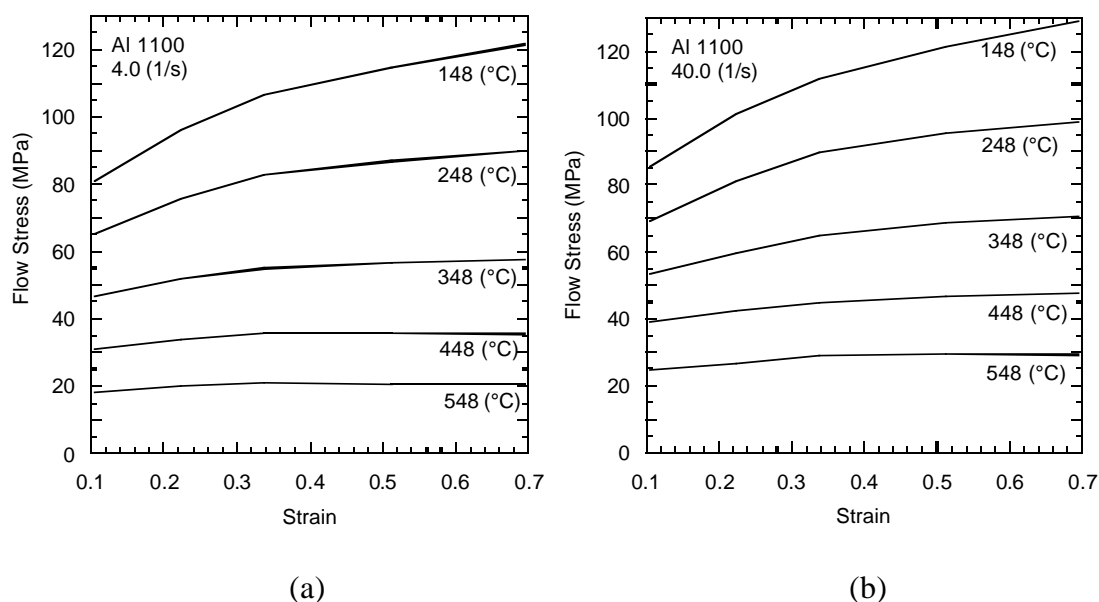


Figure 12. Flow Curves for Al 1100: (a) 4.0 s^{-1} , (b) 40.0 s^{-1}

Figure 13 and Figure 14 show results for isothermal/plane-strain material flow around the FSW pin. The simulation conditions were: pin diameter of 6.0 mm, 1000 rpm, 1 mm/s travel velocity, and a workpiece temperature of 400 (°C). Figure 13 demonstrates material flow around the pin using tracking points. The pin rotation was counter clockwise. The upper half of Figure 13 shows the initial position of the points while the lower half of Figure 13 shows the points after the pin has traveled approximately one diameter. Point 1 was initially on the joint line, and points 22 and 23 were below the joint. Note that point 22 was carried around the pin in the direction of pin rotation, while point 23 and the points below it were not. The final position of the points shows some correlation with the marker studies conducted at the University of South Carolina.

Figure 14 shows the deformation and material flow of the workpiece around the pin using a grid. This is a DEFORM™ feature called Flow Net, and it is only used for tracking material flow. It is not to be confused with the actual FEM mesh used in the solutions.

The results for a nonisothermal simulation of the initial tool plunge are shown in Figure 15 at the completion of the tool plunge. The FEM mesh of the FSW tool, workpiece, and backing tool are shown in Figure 15 along with color shaded contours of the effective strains and temperatures in the workpiece, and the load versus time curve. The FSW tool had a 6.35-mm diameter by 5.6-mm pin, a 25.4-mm-diameter shoulder, and a constant rotation of 1000 rpm. The workpiece was

6.35-mm thick. All objects were initially at room temperature and the total plunge time was 30 seconds. For 2-D axisymmetric simulations, DEFORM™ includes frictional heating due to the rotating tool, but not rotational deformation. The only deformation was due to the forging action caused by the vertical displacement of the FSW tool and the heating in the workpiece was a result of this deformation and friction.

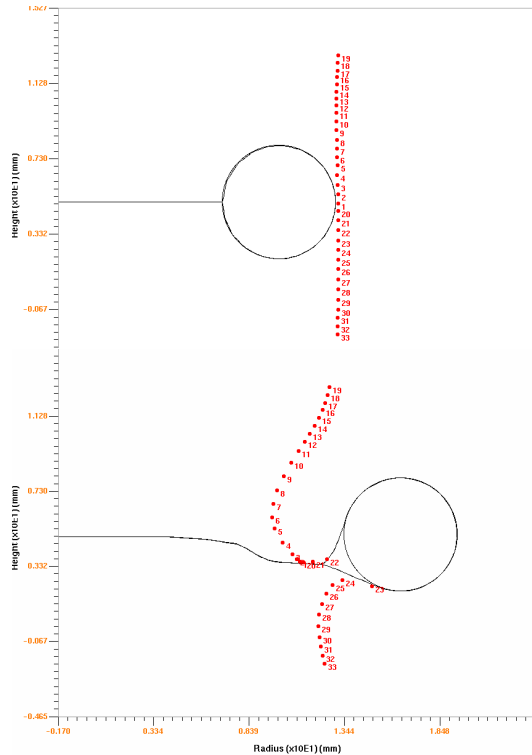


Figure 13. Point Tracking

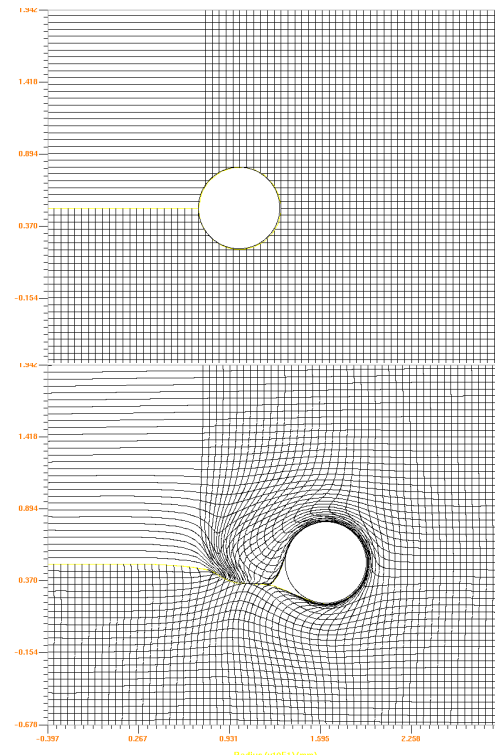


Figure 14. Flow Net

These results show a maximum workpiece temperature of approximately 560 °C, Figure 15. The loads throughout most of the tool plunge were 1000 to 1500 lbs., which correlates with experimental work conducted at the Edison Welding Institute for AFRL/MLLMP. The final load spike at the end is from the tool shoulder contacting the workpiece surface.

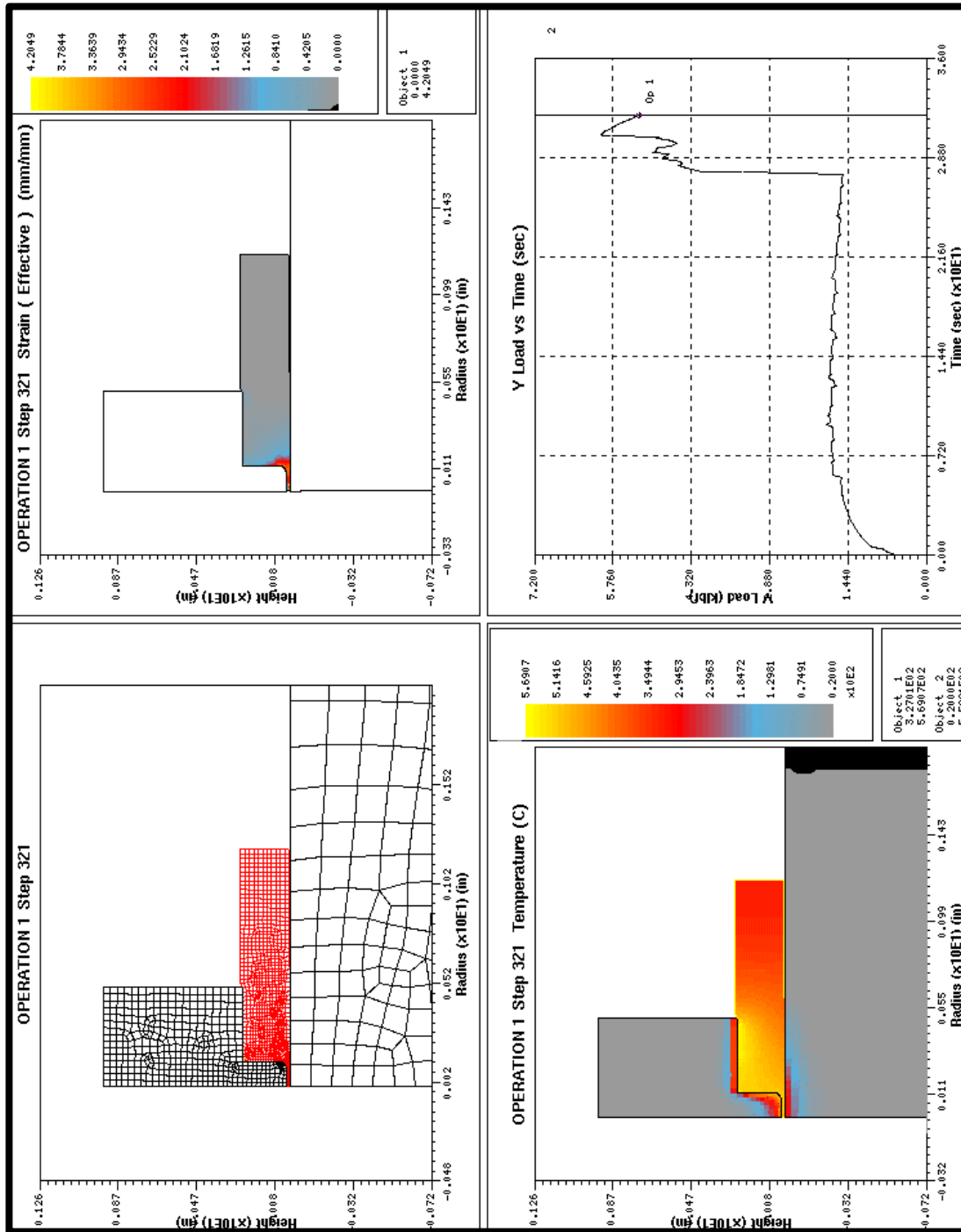


Figure 15. Simulation of Initial Tool Plunge

The following results deal with 2-D simulations for two conditions: (1) nonisothermal/plane-strain simulation of material flow around the FSW pin, and (2) comparison of experimental and simulation results of the initial tool plunge into the workpiece. The workpiece material for both simulation conditions was again 1100 Al.

Figure 16 and Figure 17 show results for the nonisothermal/plane-strain simulation of material flow around the FSW pin. The simulation conditions were: pin diameter of 6.0 mm, 1000 rpm, 1.0 mm/s travel velocity, a constant pin temperature of 500 °C, and nonisothermal conditions in the workpiece. Figure 16 compares the flownets for the isothermal simulation (400 °C workpiece, 1000 rpm, and 1 mm/s) and the nonisothermal simulation (nonisothermal workpiece, 500 °C pin, 1000 rpm, and 1 mm/s). The pin rotation was counter-clockwise for both conditions. The flownet for the nonisothermal simulation shows greater flow localization. This is due to the temperature gradients present in the workpiece. Figure 17 shows the temperature contours in the workpiece with a 500 °C constant pin temperature. The highly localized deformation zone shows temperatures from 482 to 339 °C. The 1100 Al flow stress, which is also shown in Figure 17, ranges from approximately 42 to 73 MPa in this temperature range.

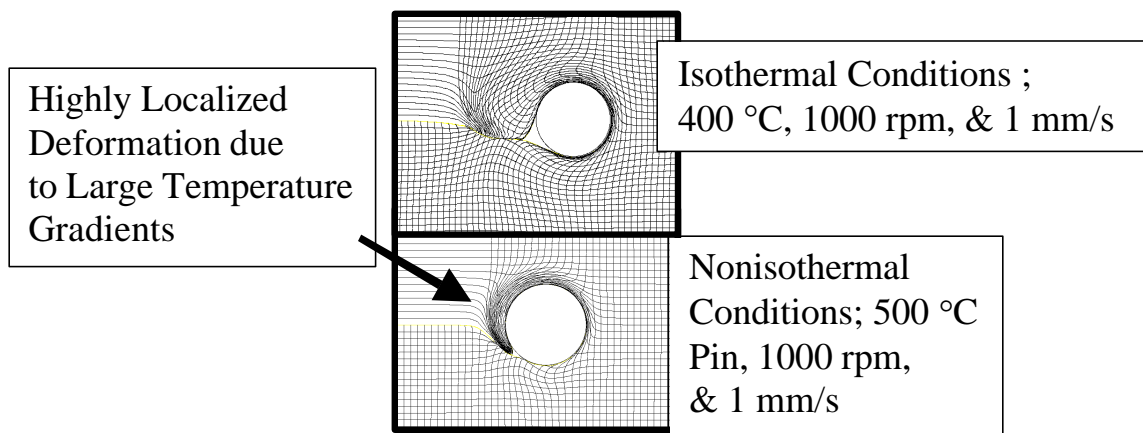


Figure 16. Comparison of Isothermal and Nonisothermal Deformation around Pin under 2-D Plane-Strain Conditions

The second simulation condition was the initial tool plunge. This was simulated as a 2-D nonisothermal/axisymmetric problem. The FSW tool had a 6.35-mm diameter by 5.6-mm pin, a 25.4-mm-diameter shoulder, and an angular velocity of 1000 rpm. The workpiece was 6.35 mm thick. All objects were initially at room temperature and the total plunge time was 30 seconds, for a plunge rate of approximately 0.18 mm/s. These results will be compared with experimental work by C.B. Smith et al., Ninth International Conference on Computer Technology in Welding, NIST Special Publication 949, May 2000.

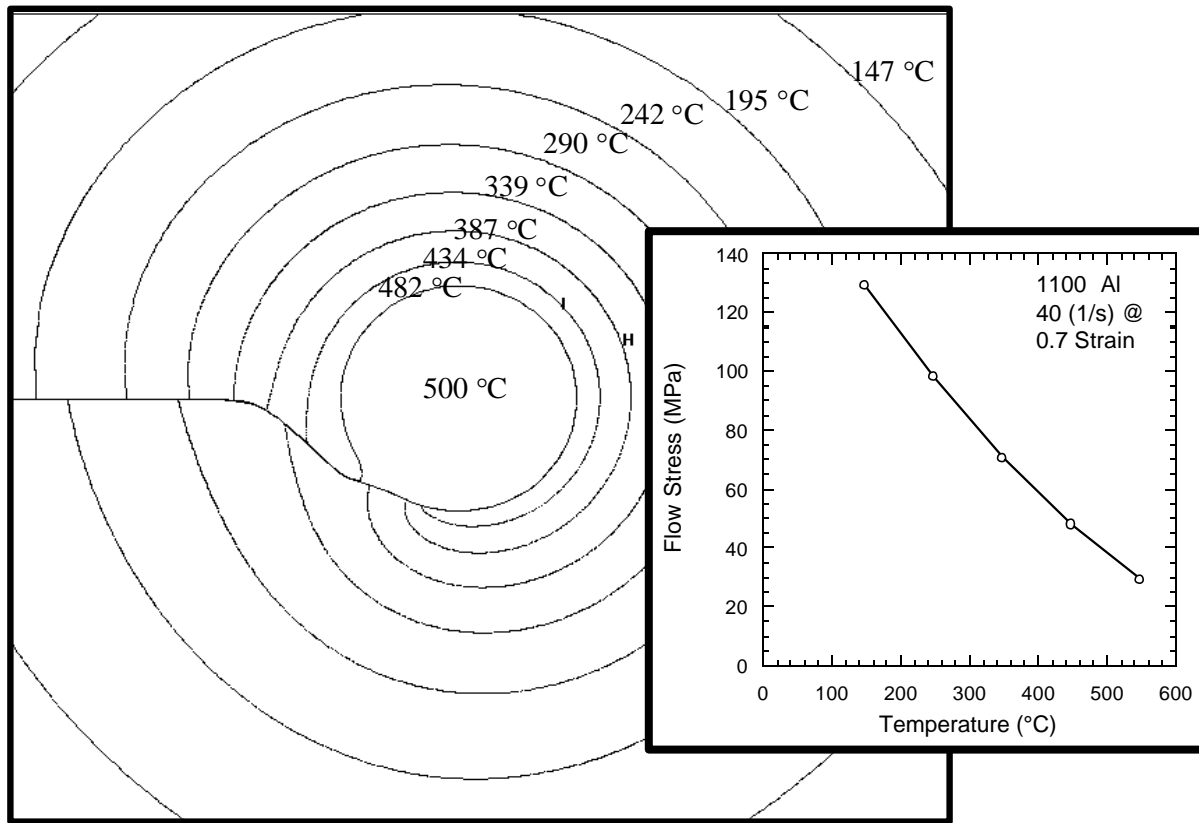
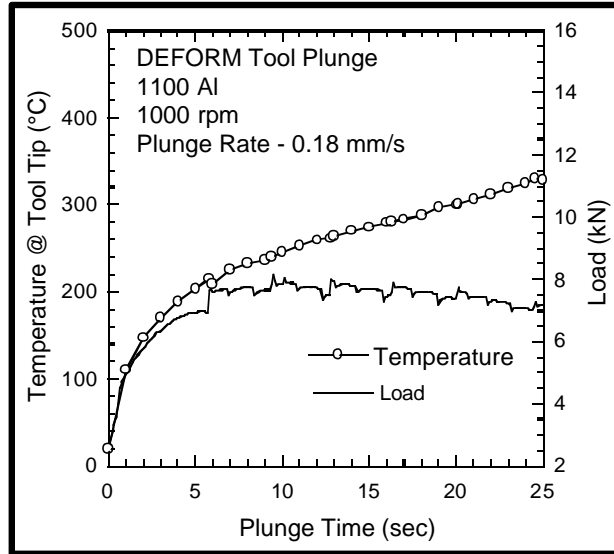
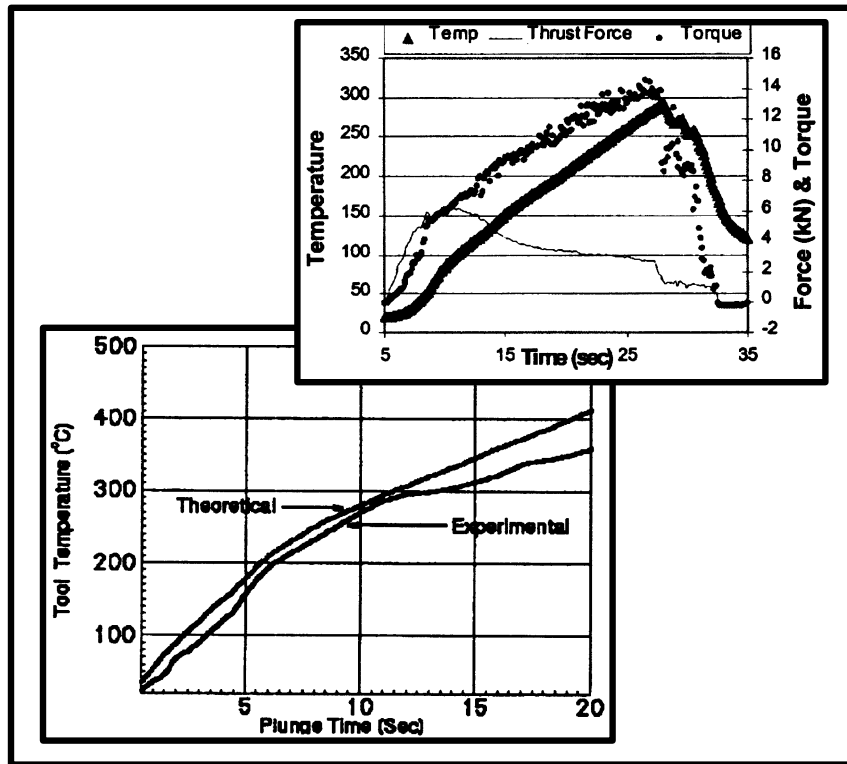


Figure 17. Workpiece Temperature Contours and 1100Al Flow Stress versus Temperature for the Nonisothermal Simulation under 2-D Plane-Strain Conditions (500 °C Pin, 1000 rpm, and 1 mm/s)

The simulation and experimental results are shown in Figure 18. Figure 18a shows the simulated tool load and temperature at the tool tip versus plunge time. The experimental loads and temperatures are shown in Figure 18b. The experimental work consisted of plunging a 5.0-mm pin into a 100-mm diameter by 12.7-mm-thick 6061-T6 Al disk. The plunge rate was 0.25-mm/s at 1100 rpm. The bottom plot in Figure 18b is the temperature at the tool tip, while the top plot in Figure 18b shows the temperature in the workpiece closest to the tool as well as the tool load and torque. Given the slightly different rotation and plunge speeds, and the different alloys, the experimental and simulated temperatures compare well for given plunge depths. The simulated temperature at 25 seconds is 320 °C, which can be compared to the experimental temperature of 350 °C at a plunge time of 18 seconds. The simulated load was approximately 8 kN while the experimental load was 6 kN.



(a)



(b)

Figure 18. Comparison of Simulated and Experimental Tool Temperatures and Loads During FSW Tool Plunge

Note: (a) Simulated, (b) Experimental (C.B. Smith et al., Ninth International Conference on Computer Technology in Welding, NIST Special Publication 949, May 2000)

The following work dealt primarily with continuing simulations of the initial tool plunge into an 1100 Al workpiece. This was simulated as a 2-D nonisothermal/axisymmetric problem. The FSW tool had a 6.35-mm diameter by 5.6-mm pin, and a 25.4-mm-diameter shoulder. The workpiece was 6.35 mm thick. All objects were initially at room temperature. Parameters such as the tool plunge velocity, tool load, and tool rotation speed were varied to show the effect on tool temperature and load.

The tool plunge velocity was varied for the case of a tool rotating at 1000 rpm. Three plunge velocities of 0.38, 0.18, and 0.094 mm/s were used so that the total plunge times were 15, 30, and 60 seconds, respectively. The temperature at the tool tip and load are plotted versus plunge depth in Figure 19 and Figure 20. The slowest plunge velocity (0.094 mm/s, 60 seconds) resulted in the highest temperatures and a low flow stress in the workpiece, which then resulted in the lowest loads. The opposite occurs with the fastest plunge velocity, where lower temperatures and higher loads occurred.

Rather than using a constant plunge velocity during the plunging operation, it is feasible to perform the operation under constant load, with tool movement dictated by the temperature and flow stress of the workpiece. Figure 21 shows the tool temperature versus time for three tool loads - 5000, 6000, and 7000 N, a rotation speed of 1000 rpm, and a plunge depth of 5.0 mm. As expected, the highest load (7000 N) resulted in the shortest plunge time, ≈ 26 seconds, and the lowest load resulted in the quickest plunge time, ≈ 56 seconds. However, the temperature is higher for the 5000 N case (≈ 380 °C) than for the 7000 N case (≈ 345 °C).

The third parameter varied was the tool rotation speed. The rotation speeds were 250, 500, 1000, and 1250 rpm and the plunge velocity was a constant 0.18 mm/s for a 30-second plunge time. The temperatures and loads are shown in Figure 22 and Figure 23. As expected, the higher rotation speeds resulted in higher temperatures and lower loads.

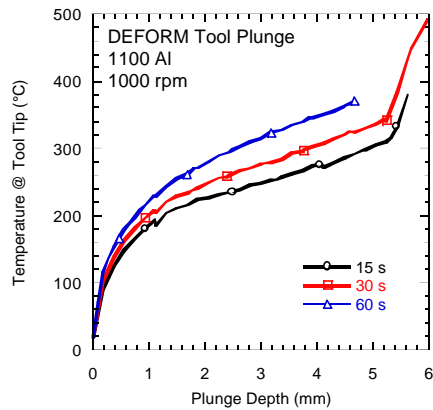


Figure 19. Tool Temperature versus Plunge Depth for Total Plunge Times of 15, 30, and 60 seconds

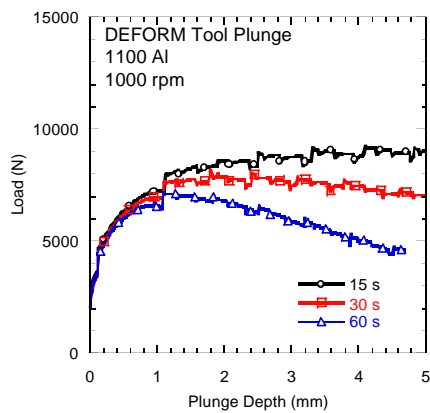


Figure 20. Load versus Plunge Depth for Total Plunge Times of 15, 30, and 60 seconds

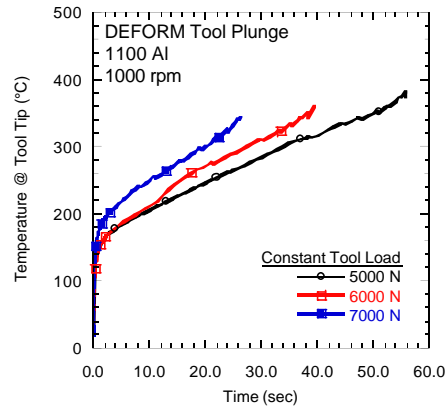


Figure 21. Tool Temperature versus Time for Constant Tool Loads during Plunging to a Depth of 5.0 mm with Loads of 5000, 6000, and 7000 N

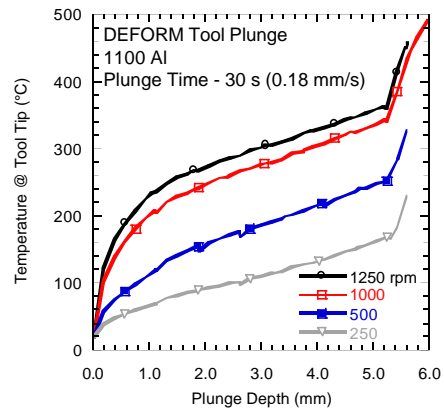


Figure 22. Tool Temperatures versus Plunge Depth for a 30 second Plunge Time (0.18 mm/s) and Tool Speeds of 250, 500, 1000, and 1250 rpm

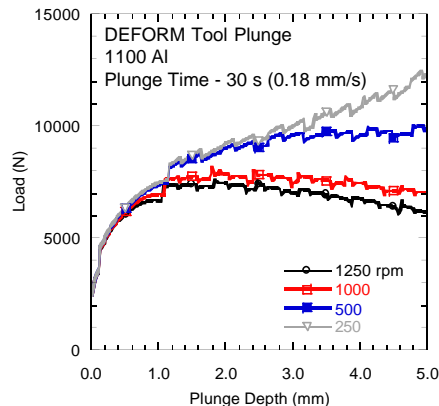


Figure 23. Load versus Plunge Depth for a Plunge Time of 30 seconds (0.18 mm/s) and Tool Speeds of 250, 500, 1000, and 1250 rpm

3.3 Furnace Cooling of TiAl Disks

Cooling curves for TiAl disks were developed for Dave Allen and Don Clemens of P&W-FL in support of the PRDA V Wrought Gamma Rotor Program sponsored by the propulsion lab of AFRL with Kathleen Sargent as technical monitor. The TiAl alloy was P&W Alloy 395 (Ti-47Al-2Cr-2Nb-1Mo-0.2B). Six disk sizes (3.0-inch I.D. by 12.6-inch O.D. by 5.5-inch thick, 3.0-inch I.D. by 17.6-inch O.D. by 1.1-inch thick, 3.0-inch I.D. by 17.6-inch O.D. by 2.83-inch thick, 1.875-inch I.D. by 20.0-inch O.D. by 4.0-inch thick, 1.875-inch I.D. by 30.0-inch O.D. by 5.0-inch thick, 1.875-inch I.D. by 10.3-inch O.D. by 2.6-inch thick) were modeled using DEFORM™. Six heat transfer conditions were simulated for each disk using three furnace cooling rates [333 °C/min (600 °F/min), 111 °C/min (200 °F/min), and 27.7 °C/min (50 °F/min)] and two disk emissivities (0.3 and 0.6). The initial disk temperatures were 1349 and 1371 °C.

The cooling curves plot temperature versus time in the center of the disk, mid-radius and mid-height (Figure 24). The cooling curves were used to estimate the maximum cooling rate in the disks during furnace quenching after heat treating in P&W's 30-inch diameter by 45-inch long furnace. The maximum cooling rate for this furnace is accomplished by circulating helium with a fan through the furnace and an external heat exchanger, creating a 4 to 5 psi positive pressure. A maximum furnace-cooling rate of 600 °F/min has been measured using a thermocouple located in the center of the furnace. This 600 °F/min cooling rate was measured with a relatively small mass in the furnace, while the cooling rate with larger masses, such as the disks modeled here, is unknown and expected to be lower, which is the reason for modeling with three cooling rates. Heat treatments of two 10.3-inch O.D. by 2.6-inch disks yielded an estimated cooling rate of 80 °F/min in the center of the disk, which occurs with a furnace-cooling rate between 200 to 600 °F/min.

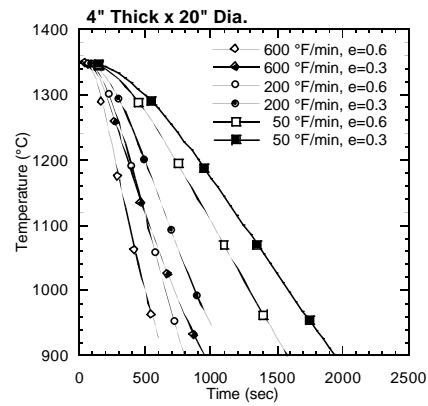
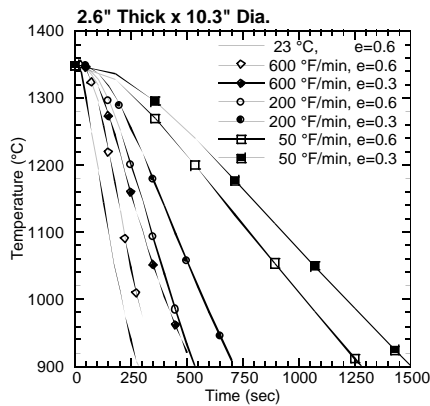
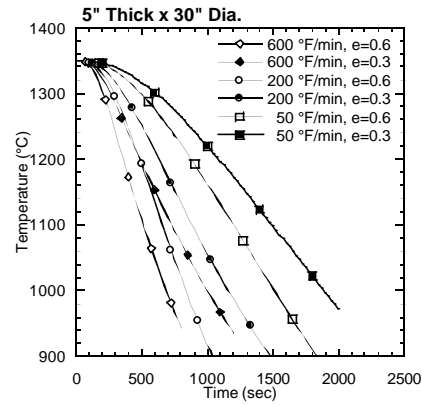
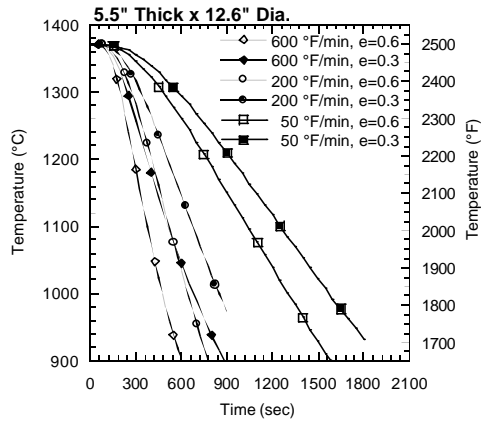
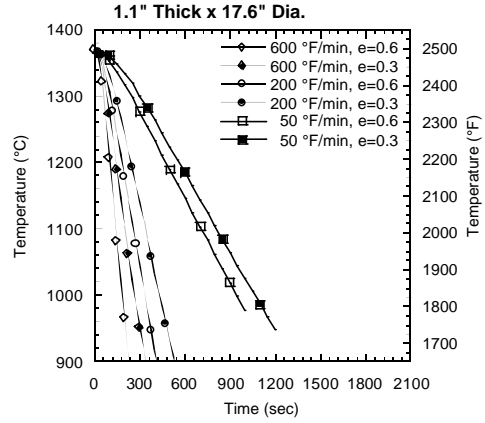
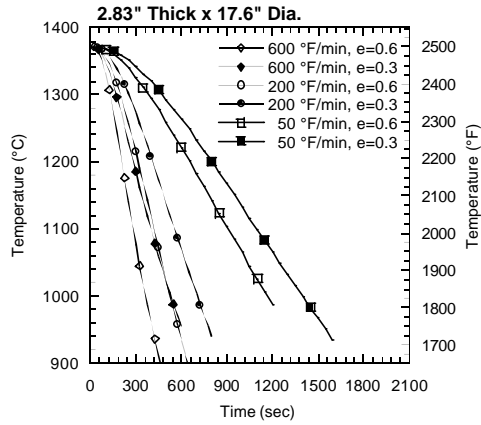


Figure 24. Cooling Curves for TiAl Disks Showing Disk Temperatures at Mid-radius and Mid-height with Various Furnace Cooling Rates (50, 200, and 600 °F/min) and TiAl Emissivities (0.3 and 0.6)

3.4 Microstructure Development and Crack Initiation During Deformation Processing of Gamma Titanium Aluminide Alloys

Work on the breakdown of multiphase titanium aluminide ingots through forging and extrusion methods was presented. The influence of the lamellar grain size on plastic flow behavior as well as microstructure evolution during hot deformation of lamellar structures was described. The kinetics of dynamic globularization during hot working was analyzed to identify the roles of microstructural and deformation parameters separately. A simple model for the onset of wedge cracking during hot working was developed. This model, which was based on a critical value of the product the peak flow stress and square root of the grain size, was used to predict the occurrence of brittle, intergranular failure of gamma titanium aluminides. Furthermore, the ductile cracking encountered in forgings at high strain rates was predicted successfully using a maximum tensile work criterion. This work was presented at the 5th Tri-Service Titanium Contracts Review, WPAFB, 7-9 October 1997 by Seetharaman, Goetz, and Semiatin [35].

3.5 Salt Pot Quenching of a TiAl Bar

Heat transfer modeling was performed to determine cooling curves on a square bar of TiAl preheated to 1315 °C and quenched in a salt bath at either 871 or 1037 °C using 3-D DEFORM™. The TiAl bar was 76.2-mm square by 152.4-mm long and the temperature of the salt bath was assumed constant. The heat transfer coefficient between the TiAl bar and liquid salt bath was either 290 or 585 J/s m² K for salt temperatures of 871 or 1037 °C, respectively. A simple 1-D lumped-parameter numerical analysis was also performed to determine the temperature increase of the salt bath due to the large mass of the TiAl bar, assuming 0.00469 m³ of Liquid Heat 1550 in the MPL salt pot, as shown in Figure 25. The 1-D numerical results compared well with the 3-D FEM results using DEFORM™. This work was conducted for Dr. Dennis Dimiduk of AFRL/MLLMD in consultation with Dr. S.L. Semiatin of AFRL/MLLMP.

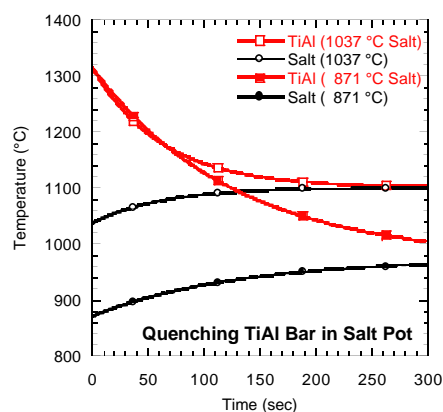


Figure 25. Temperature versus Time Curves for a TiAl Bar Preheated to 1315 °C and Quenched in a Salt Bath at either 871 or 1037 °C using a 1-D Lumped-Parameter Numerical Analysis

3.6 Consolidation of a Wire Ti/SiC Composite

The consolidation of a wire wound, Ti matrix, SiC composite was modeled using the powder metal (PM) model in DEFORM™. This work was performed for Atlantic Research Corporation. Further processing details are proprietary.

3.7 Void Growth Modeling

Void growth was modeled using 3-D DEFORM™. The growth of a thin, disk-shaped void under uniaxial tension was modeled with various strain rate sensitivities (0.05, 0.3, 0.5) and disk orientation angles (0°, 45°). The shape change of the disk was examined by plotting the disk thickness, radius, and the ratio of the two with strain. This work was conducted in collaboration with Dr. Amit Ghosh.

3.8 Feasibility of an Ultrasonic Die Pressure Sensor

The University of Dayton Research Institute (UDRI) in conjunction with AFRL/MLLMP (Dr. Rollie Dutton) investigated the possibility of developing a surface-pressure sensor for forging dies using an ultrasonic probe. The work conducted by UES in support of this project entailed conducting FEM simulations of simple cylinder upset forgings to determine if the expected amount of die deflection would be within the measurement limits of the ultrasonic sensor. This consisted of modeling the room temperature forging of 3.0 inch diameter by 6.0 inch 304 stainless steel (SS) and Ti-6Al-4V cylinders between flat H13 tool steel dies, which were 5.0-inch thick by 14.0-inch dia. Experimental forgings were also conducted using the 1000-ton Erie forge press. The 304SS simulation predicted that the 1000-ton load limit would occur at a stroke of just over 2.5-inch (≈ 42 percent reduction in height, strain ≈ 0.54). The maximum von Mises stress in the H13 die would be 130.4 ksi and the maximum surface deflection would be 0.014 inch. At 2000 tons the stroke would be ≈ 3.6 inch, and the maximum die stress and deflection would be 190.6 ksi and 0.022 inch, respectively, which is just under the 200 ksi yield stress for H13 with a hardness of HRC50. For Ti-6Al-4V, the die deflection was also 0.014 inch at the 1000-ton press limit, although the maximum die stress was higher at 155 ksi. The higher stress was due to a smaller maximum stroke (≈ 1.63 inch) and thereby a smaller diameter. The FEM results showed that the maximum die deflections that would occur with the 1000-ton Erie press were below the measurement capabilities of the ultrasonic probe sensor. Due to this, UDRI switched to a piezoelectric based pressure sensor.

3.9 Extrusion of Nanophase Al Tubing

The Rocketdyne Division of Boeing is developing nanophase aluminum alloys with a high specific strength for space systems. In assistance to Rocketdyne, the Materials and Manufacturing Directorate of AFRL conducted tube-extrusion trials at MPL on canned, nanophase Al preforms to investigate the feasibility of tube extruding this alloy. FEM simulations were also conducted to provide insight into metal flow and failure during both the sub-scale tube extrusion trials at MPL as well as production-scale extrusions. The FEM simulations correlated with the MPL subscale extrusion of the monolithic extrusions as well as the canned extrusions. Further processing details are proprietary [Sec 7.3].

3.10 Dynamic Recovery Modeling (DRX) Using CA

Work was initiated on a possible joint project on DRX with Dr. Frank Montheillet, Director of Research CNRS, Saint-Etienne, France. As a prelude to this project, Dr. Montheillet requested the input data for the strain hardening (h) and dynamic recovery (r) parameters used in the DRX cellular automata model of reference [27] for use in his DRX model, wherein the rate of change of dislocation density (\mathbf{r}) is $d\mathbf{r}/dt = (h - r\mathbf{r})$. The value of h used in the CA model would correspond to the term for cell dislocation input, which is referred to as $d\mathbf{r}/dt$ in [27]. The term r was not explicitly used in the CA DRX model [27], although it is easily derived ($r = (490/K)^2(h)^{1-2m}$) from Equations (3) and (6) in reference [27] and the relationship, $r = (h)/\mathbf{r}_{DR}$, where \mathbf{r}_{DR} is the average steady state dislocation density. The parameter m is the strain rate sensitivity, K is from the power-law equation, $\mathbf{s} = K(\text{strain rate})^m$, and 490^2 is the number of CA cells. Integration of $d\mathbf{r}/dt = (h - r\mathbf{r})$ results in: $\mathbf{r}_{AVE}(t) = (1/C)[h - \exp(\ln(h) - C \cdot t)]$, where $C = (490/K)^2(h)^{1-2m}$. The results for $\mathbf{r}_{AVE}(t)$ from the CA model [28] with dynamic recovery only and the integrated equation given above correlated very well (Figure 26a), showing CA's capability for modeling problems typically handled by differential equations. Also, since Dr. Montheillet uses the Laasraoui-Jonas equation [36] for dynamic recovery, a comparison was made between CA, the Laasraoui-Jonas equation, and a similar equation from Roberts [37]. This comparison was made by plotting the strain hardening rate (θ) versus stress for the three cases. The curves were very similar with CA being the highest, followed by Laasraoui-Jonas, and then Roberts (Figure 26b).

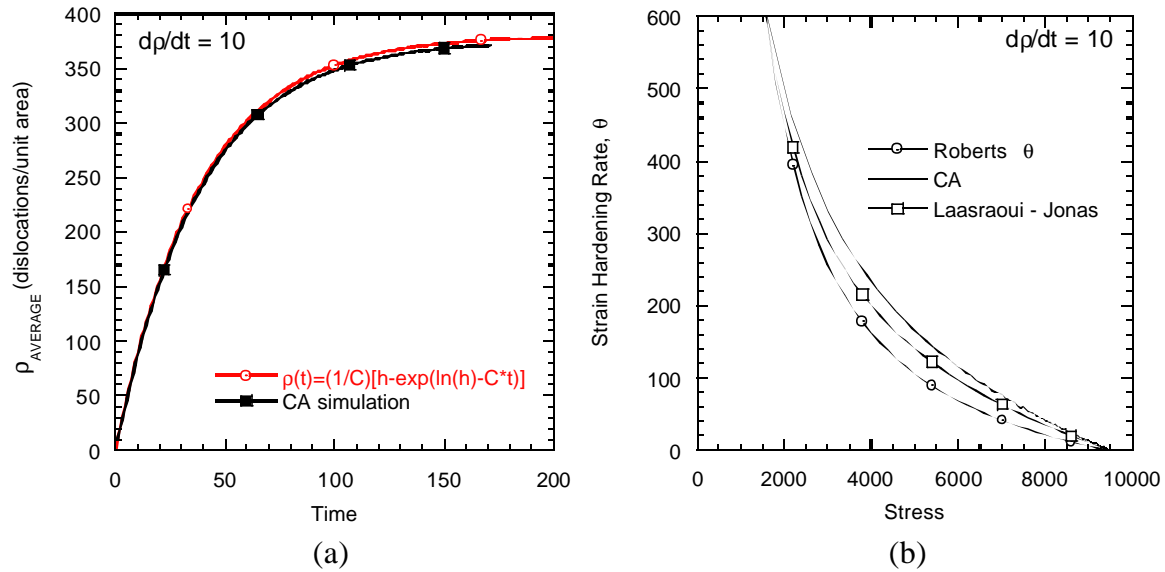


Figure 26. (a) Comparison of $\rho(t)$ using CA and the Integrated Equation, (b) Strain Hardening Rates for Dynamic Recovery only using CA, Laasraoui-Jonas, and Roberts.

3.11 FEM of ECAE of Tungsten Heavy Alloy for DOE

Tungsten heavy alloys (WHA) were investigated as a possible replacement for depleted uranium in long rod, kinetic penetrators in High-Velocity, Armor-Piercing, Fin-Stabilized, Discarding-

Sabot tank projectiles. Tungsten heavy alloys are powder metallurgy composites of W, Ni, and Fe with tungsten contents of 90 to 97 percent. Typical microstructures of heavy alloy composites show rounded grains of essentially pure tungsten surrounded by an alloy of nickel, iron, cobalt and/or copper, and as much tungsten that can be taken into solution. This is a two-phase composite of brittle tungsten grains surrounded by a ductile matrix, resulting in a tungsten alloy of high density for use as a kinetic penetrator, which also possesses useful mechanical properties not usually associated with tungsten.

This work was conducted by UES in support of a joint project investigating the processing of tungsten heavy alloys using ECAE by the Idaho National Engineering and Environmental Laboratory (INEEL) and the Army Research Laboratory. This involved compression testing for flow stress development of WHA and a Cu alloy used as model material, ring tests for determination of the friction factor, and FEM modeling of the 0.5-inch by 0.5-inch, 120° ECAE tooling located at the INEEL facility. The goals of the project were to:

1. Conduct compression tests for flow stress determination: six copper (C10100, 99.99%) tests at R.T. and 100 °C with strain rates of 0.01, 0.10, and 1.0 s⁻¹, six WHA tests at 200, 300, and 400 °C with strain rates of 0.01 and 1.0 s⁻¹. The dimensions for the Cu and WHA specimens were 0.35 inch diameter by 0.53 inch tall. The 400 °C WHA test was for deformation heating corrections.
2. Evaluate the feasibility of WHA ring tests based upon flow stress levels from compression tests.
3. If ring tests were feasible, calculate and provide sample dimensions to Department of Energy (DOE) for machining.
4. Determine the friction factor during ECAE by conducting ring tests under the following conditions: WHA ring tests at 200 and 300 °C and strain rates of 0.01 and 1.0 s⁻¹, Cu ring tests at R.T. and strain rates of 0.01 and 1.0 s⁻¹. The lubricant used for Cu tests was Loctite Moly Paste, Low Friction Lubricant #51048.
5. Evaluate friction factors using deformed ring dimensions from ring tests and standard calibration curves.
6. Conduct FEM simulations of ECAE under initially isothermal conditions for Cu: temperature = R.T., friction factor, $m = 0.2, 0.8$, and ram velocity = 10 ipm.
7. Conduct FEM simulations of ECAE under initially isothermal conditions for WHA: temperature = 200, 300 °C, friction factor, $m = 0.2, 0.8$, and ram velocity = 10 ipm. A ram velocity of 0.1 ipm will also be used if flow curve shapes are significantly different at different strain rates.

Results to date include: flow curves from compression tests, flow curves from ring tests, friction factors from ring tests, FEM results of load versus stroke, strain fields, temperature fields, and stress fields in idealized die, and evaluation of load requirements. This work was still in progress at the end of the contract.

4 COOPERATIVE PROJECTS

4.1 Cooperative Technology Clusters (CTeC) Pilot Program

A critical need exists in the U.S. military for rapid development of new materials and materials processing technology in an uncertain international environment where streamlined turn-around times to deployment can be critical. Private industry in the U.S. has a parallel need to minimize the time and cost from research to commercialization. Both industry and U.S. military interests can be best served by establishing research and development teams between industry, the technology research community and AFRL in key predefined technology project areas.

The U.S. has invested substantially over the years in AFRL at Wright-Patterson Air Force Base (WPAFB), Dayton, Ohio to build up the world's premier research centers in materials and materials processing technology as well as in microstructural characterization. The highly skilled research teams at AFRL have unique equipment and facilities at their disposal. In the past, these researchers have focused their efforts on making U.S. military aircraft the best in the world. By turning a portion of their efforts to assisting U.S. industries, we can now get a further payback on our taxpayer dollars by increasing the world competitiveness of our industries and thus increasing the standard of living of the American people.

In the CTeC pilot program, UES and Edison Materials Technology Center (EMTEC) teamed up to bring private industry together with AFRL. UES is the on-site contractor that operates many of the relevant facilities at AFRL. UES scientists and technicians performed most of the actual research. EMTEC is a nonprofit organization whose mission is to strengthen private industry through technology innovations. EMTEC acted as the collaborative facilitator, forming clusters of companies with common research interests.

EMTEC used its experience and contacts in private industry to bring together groups of companies that had common research needs. Each of these clusters, in cooperation with AFRL and UES personnel, formulated a research task that utilized the unique capabilities of AFRL to increase the competitiveness of the members of the cluster. UES personnel then conducted the work at the AFRL facilities.

The CTeC concept has substantial benefits for the Air Force and the participating companies:

1. The Air Force benefits from forming closer ties between its researchers and private industry and from increasing the efficient utilization of its facilities and personnel. The result is an increase in defense readiness and a decrease in the cost of performing ongoing Department of Defense (DoD) research.
2. Private industry benefits from being able to utilize the unique capabilities of the personnel and facilities that are already in place at AFRL. The result is increased competitiveness that gives U.S. companies an edge in the world market.

The goals of this pilot program were to demonstrate the contractual, financial and technical structure of a full-scale program and to show how the research capabilities of AFRL can be brought to bear on an industrial project. These goals were fully achieved. The success of this

pilot program has resulted in a full-scale follow-on program. The experience gained in the pilot program aided in the development of the complex contractual and funding mechanisms that are needed to institutionalize CTeC as a long term program that will benefit both industry and the Air Force.

For more information, see Appendix A for the CTeC Final Report.

4.2 CRADA

UES and the Air Force entered into CRADA #99-025-ML-01 on 25 January 1999 to run concurrently with the on-site contract. The purpose of the CRADA was to provide a mechanism to make the facilities and personnel of the MPL available to external organizations while recovering appropriate costs of operating the facility.

The CRADA proved to be a very workable tool. UES was able to handle all of the contractual interfacing with the external organization. This sped up the contractual process and greatly simplified the paperwork that was required from the external organization. UES provided a quote based on the customers' requirements, performed the work and collected payment. These funds covered all of the labor and materials that were expended on each CRADA task. UES also passed 10 percent of the CRADA revenue on to the Government to offset the Government costs associated with the work.

CRADA tasks ranged in size from small efforts involving a handful of extrusions to major efforts that lasted more than a year. In all cases, the organizations came to the MPL because of the unique facilities and expert personnel that it has to offer.

The work performed under the CRADA was always carried out on a noninterference basis. This meant that the work was largely done after hours and on weekends so as to not interfere with the Air Force research work that is the primary mission of the MPL.

The tasks performed under the CRADA are summarized briefly in the following sections.

4.2.1 American Superconductor Corporation

The development of substrates for superconductors has been an area of intense research in the past several years. American Superconductor relied on the MPL for the development of their rolling and extrusion processes. The tasks are summarized in Table 9.

Table 9: CRADA Tasks for American Superconductor

CRADA Task	Description
188-001	Two rollings
188-002	Six rollings
188-004	Two extrusions
188-005	Two extrusions and eight rollings
188-006	Nine rollings
188-009	Thirteen rollings
188-019	Two extrusions and thirteen rollings
188-021	Six rollings
188-022	Two extrusions
188-023	Six rollings
188-024	One rolling

4.2.2 RTI Energy Systems, Inc.

Under CRADA task 188-003, UES performed 12 upset tubing forgings. This was a process development project with RTI and RMI Titanium Company.

4.2.3 Boeing N.A. (Rocketdyne)

Under CRADA task 188-007, UES performed four extrusions of nanophase Al billets. Refer to Section 3.9 for a complete discussion.

4.2.4 Howmet Research Corporation

Under CRADA task 188-008, UES performed two rollings of steel billets for the Howmet Whitehall Research Center, in support of their development effort for casting die materials.

4.2.5 UDRI

Under CRADA task 188-010, UES conducted a series of tests of a forging die sensor. UDRI had recently developed a new type of sensor for measuring load. UES personnel designed a method of incorporating this sensor into a forging die to measure loads at the surface of the die. UES conducted a series of forgings on the 1000-ton press while UDRI engineers monitored the output from the sensor. The results compared well with the loads that were expected based upon the standard load cell and hydraulic pressure.

4.2.6 Allison Advanced Development Co.

Under CRADA task 188-011, UES and Allison undertook a significant project on the deformation processing of a complex niobium alloy. This project involved compression testing, extrusion and metallographic analysis.

4.2.7 Pratt & Whitney (Bernd Group)

Under CRADA task 188-012, UES conducted one extrusion of a moly-based billet.

4.2.8 Concurrent Technologies Corporation (CTC)

Under CRADA task 188-013, UES conducted a significant study of the forging die workpiece interface friction and heat transfer between alloy steel and alloy Ti-6Al-4V. This project involved compression testing, ring testing and numerical analysis. Full details are given in Section 3.1.

4.2.9 Boeing MAI

Under CRADA task 188-014, UES conducted process modeling for friction stir welding for the MAI. This project was entirely analytical modeling. For complete details, see Section 3.2.

4.2.10 Department of Energy (DOE)

UES quoted CRADA task 188-016 for ECAE modeling for the DOE. The work was instead funded directly under the on-site contract, see Section 3.11, for details.

4.2.11 Pratt & Whitney

UES quoted CRADA task 188-017 for Pratt & Whitney. The work was instead funded directly under the on-site contract.

4.2.12 Pratt & Whitney (Bernd Group)

Under CRADA task 188-018, UES performed twenty compression tests and two moly extrusions for Pratt & Whitney.

4.2.13 Lockheed - LDM

UES quoted CRADA task 188-020 for study of Laser Direct Manufacturing. This quote was outstanding at the conclusion of the subject contract, but is expected to be funded during the follow-on contract.

5 PROCESSING OF MATERIALS

Much of the day-to-day activity under this program was focused on the actual processing of materials by either deformation or solidification. This work supported the contract's research activities as well as the activities of numerous other agencies both inside and outside of the government. Summaries of these processing operations are given in the following subsections. Complete records were maintained on every major operation performed and are kept on file in the Processing Lab office.

5.1 Extrusion

The 700-ton Lombard extrusion press was the most heavily used piece of equipment in the lab. Two hundred fifty-three extrusions were performed under this program. Customers included several groups in AFRL, as well as many private corporations.

Table 10 gives a breakdown of the extrusions performed cross tabulated by agency versus material class. Detailed records of each operation are on file in the Processing Lab office. Over 10,000 extrusion records, dating back to the 1950s, are in a searchable computer database.

Table 10. Summary of Extrusion Operations

Organization	Material Class										Total
	◇	Al	Cu	In	Mo	Nb	Ni	Ta	Ti	TiAl	
		3									3
AFRL/MLLM		38			2	1			14	5	60
AFRL/MLLN		3							4		7
AFRL/MLMR									8		8
Allison Advanced Development Co.						1					1
American Superconductor Corp.							8				8
Boeing N.A. (Rocketdyne)		4									4
Brush Wellman			5								5
CTeC		3									3
CTeC: Task 001		4									4
CTeC: Task 003		14									14
Cutler-Hammer			2								2
Eaton Corporation			2								2
McDonnell Douglas									3		3
Naval Surface Warfare Center							18				18
Pittsburgh Materials Technology	3				1						4
Pratt & Whitney					3		3				6
Refractory Metals Technology								2			2
Rockwell Science Center		9									9
RTI Energy Systems (RMI)									11		11
Systran		9									9
Systran WUD 56		9									9
UES	1	24			6	2			6	4	43
UES (WUD 55)										4	4
University of California – Irvine				1							1
Westinghouse Electric (Bettis)	7				1	2					10
Wright State University		3									3
Total	11	123	9	1	13	6	29	2	46	13	253

5.2 Forging

The 1000-ton Erie forge press was used for plasticity studies, process development and simple upsettings. A total of 278 forging operations were performed. Table 11 summarizes the forging work. Detailed records are on file in the Processing Lab office.

Table 11. Summary of Forging Operations

Organization	Material Class									Total
	Al	Ni	SS	Ti	TiAl	Pb	Nb	Cu	Steel	
WUD 49	34		6	69	2	1		9		121
WUD 51,52 55,56,57	19			17	44		1			81
Systran/Ashbee				24	24					48
McDonnell Douglas				8						8
Wright State	1									1
AFRL/PRPS		2								2
American Superconductor		7								7
Howmet									6	6
UDRI	4									4
Total	58	9	6	118	70	1	1	9	6	278

5.3 Rolling

A total of 233 multipass rolling operations were performed. Table 12 summarizes the operations. Detailed records are on file in the Processing Lab office.

Table 12. Summary of Rolling Operations

Organization	Material Class						Total
	Al	Ti-Al	Ni	Ti	Al-Li	Other	
WUD 49		13		37		18	68
WUD 52,55,56	28	4	1		1		34
Wright State Univ.	3						3
McDonnell Douglas				30			30
American Superconductor			68				68
WL-POOX			21				21
Battelle	1						1
OSU						2	2
Howmet						6	6
Total	32	17	90	67	1	26	233

5.4 Mechanical Testing

Mechanical testing was performed to provide material data for process modeling and to assist in process development. The majority of the mechanical tests were performed on a 55 kip MTS Systems Corporation (MTS) test frame to measure flow stress over a range of temperatures and strain rates. A 200 kip MTS test frame was also used to conduct heat transfer experiments. Mechanical tests are summarized in Table 13.

Table 13. Summary of Mechanical Testing

Organization	Compression Tests	Ring Tests	Total
WUD 49	578		578
WUD 55	37		37
Boeing	99		99
Pratt & Whitney	8		8
Allison Advanced Development Co.	13		13
DOE	10	11	21
CTC	10	60	70
Total	755	71	826

5.5 Evacuation and Degassing

A total of 90 evacuation, degassing and sealing operations were performed on extrusion, and HIP cans. Summaries of these operations by Type of Can are given in Table 14. Detailed records of each operation are on file in the Processing Lab office.

Table 14. Summary of Evacuation, Outgassing, and Sealing Operations

Organization	Type of Can		Total
	Extrusion	HIP	
WUD 49	2	6	8
WUD 51,52,5355,56	43	15	58
Systran	6		6
Adtech	6		6
Virginia Tech.	12		12
Total	69	21	90

5.6 Vacuum Arc Melting (Button Melts)

A total of 594 vacuum arc melting operations were performed primarily in support of alloy development work by Government and contract scientists in AFRL. These were mainly 50- to 250-gram button and cigar melts. Table 15 summarizes these operations by material class and customer. Detailed records are on file in the Processing Lab office.

Table 15. Summary of Vacuum Arc Melting

Organization	Material Class						Total
	Ni	Mo	Nb	Ti	TiAl	Other	
WUD 49				34			34
WUD 53,55,56		145	134	100	120	53	552
ARFL/PRPS	8						8
Total	8	145	134	134	120	53	594

5.7 Vacuum Induction Melting (VIM)

A total of 43 VIMs were performed. These were conducted for solidification research and for alloy development. Many were instrumented with multiple thermocouples so that cooling curves could be compared to simulation results or used to calculate Interface Heat Transfer Coefficients. Table 16 summarizes these operations. Detailed records are on file in the Processing Lab office.

Table 16. Summary of VIM

Organization	Material Class								Total
	Al-Cu-Zr-Ti	Al 7045	Al 6061	Al Mg	Al 1100	Al + Sc	Ti-6-4	Ti-62-4.2	
US Army Research Lab	3								3
WUD 49		1	5	1	1	23	1		40
Total	3	1	5	1	8	1	23	1	43

5.8 Heat Treatment

Nearly all of the hundreds of extrusion, forging, and rolling operations that were performed required preheats to bring the billets up to the working temperature. In addition to these preheat operations, there were 355 heat treatments performed that were not direct precursors to forming operations. Table 17 summarizes the operations. Detailed records are on file in the Processing Lab office.

Table 17. Summary of Heat Treat Operations

Organization	Type of Specimens						Total
	Ti	Ti-Al	Ni	Steel	Al-Mg	Al	
WUD 49	198	55	12	32	9	1	307
WUD 52,55,56	9	22				7	38
McDonnell Douglas	1						1
WL-POOX			6				6
WUD 1		3					3
Total	208	80	18	32	9	8	355

5.9 Welding and Fabrication

Welding and fabrication operations were performed in support of metal working operations and equipment maintenance. The bulk of the machining and welding is the making of vacuum tight cans that contain either powder or solid research materials to be extruded, rolled, forged or HIP'ed. Cans are fabricated from a variety of materials, most commonly titanium, stainless steel, carbon steel, or aluminum. Exotic materials and welds are occasionally required, such as the welding of C.P. titanium to TiAl. Every can that is fabricated is tested for vacuum tightness using a helium leak detector. A summary of the 400 major research welding operations performed is given in Table 18.

Table 18. Summary of Welding Operations

Organization	Type of Welding Operations						Total
	Extrusion Cans	HIP Cans	Rolling Cans	Forging Cans	ECAE Cans	Other	
WUD 49	13	9	8		30	48	108
WUD 52,53,55,56	94	68	4	38	4	15	223
MLLN WUD 1						42	42
MLBC						1	1
MLBT	1	1				19	21
MLPO WUD 48						2	2
MLPS						1	1
McDonnell Douglas						1	1
UDRI						1	1
Total	108	78	12	38	34	130	400

6 OPERATION OF MATERIALS PROCESSING LAB

6.1 Design and Build Rapid Heat Treatment Test Stand

Previous work demonstrated the feasibility of using rapid induction heating to create desired microstructures in titanium alloys. In a follow on to that work, a set of experiments were designed to use a higher frequency induction power supply and a more rapid quenching method.

A rapid heat treatment test stand was designed, built, and successfully used with the high frequency induction generator. The experiments were completed and the test stand was removed to the high bay for storage.

6.2 Install and Commission Salt Pot Heat Treatment Furnace

Salt pot furnaces are a superior method of heating and quenching in many situations, due to (1) the high conductivity of the liquid salt, (2) the stable and easily measured temperature, and (3) the protection from oxidation. A new salt pot furnace had been purchased previously. In this effort, new stainless steel ductwork was installed to connect the salt pot hood to an exhaust blower on the roof. The pot was loaded and baked out, and the salt was melted. Temperature measurements were made to correlate the salt temperature with the furnace setpoint and to check the uniformity of the temperature in the bath itself. The system worked very well. Two additional sets of crucibles (pots) were ordered to use with other temperature salts.

The salt pot was successfully employed to conduct thermocouple experiments using 1018 salt. During a changeover to 1550 salt, though, a crucible and backup liner both cracked. Heat up procedures were modified and a charge of 1550 salt was successfully brought up to temperature.

The salt charge in the salt pot was successfully converted from type 1018 to type 1550 salt, overcoming an earlier problem with crucible cracking during heat up. Additional spare crucibles have been obtained.

6.3 Design, Fabricate, and Commission ECAE Tooling

ECAE is an innovative new method of extrusion that introduces plastic work into a billet with no reduction in cross sectional area. The method has been reduced to practice at Texas A&M. UES subcontracted with Texas A&M to design an ECAE tool stack for the 1000-ton forge press at WPAFB. UES personnel worked closely with the tooling designer to develop a design that would work with the forge press in regard to both the physical constraints and the control system capabilities.

UES solicited quotes for fabricating the tool stack from several local machine shops. The fabrication contract was awarded to Millat Industries and they successfully completed the machining, fabrication and assembly of the ECAE tool system components. UES personnel performed the final assembly of the ECAE tool stack and installed it in the 1000- ton press. A number of trial extrusions were performed. The tool stack is fully functional and has been used to conduct numerous research extrusions of materials ranging from copper to Ti-6Al-4V.

6.4 Install and Commission Load Cell in 1000-Ton Forge Press

Installation of a load cell directly into the die stack on the 1000-ton forge press is critical to conducting well-instrumented physical modeling experiments. The press was designed to use the hydraulic fluid pressure to indirectly estimate the press load. During this contract, an insert for the standard 14-inch die stack was designed and fabricated to accommodate the 1000-ton load cell directly in the die stack.

Prior to using the new load cell capabilities, the 1000-ton and 250-ton load cells were sent to Texas for calibration. The 250-ton cell's new calibration was very similar to the old calibration. The 1000-ton cell's new calibration was considerably different from the old calibration. UES personnel conducted a series of tests on the load cells and discovered that the load readings were not consistent between the two cells. It was finally determined that the 1000-ton cell calibration had been improperly conducted. The cell was shipped back for recalibration. After recalibration, another series of test were conducted that gave very good agreement between the two load cells.

A series of both dynamic and static load tests were conducted to compare the load cell readings to the press tonnage that was estimated from the oil pressure. Much to UES' delight, there was excellent correlation between the load cell readings and the oil pressure load estimates. The test conclusion was that the oil pressure was quite good, except at high ram velocities.

6.5 Relocation of the Harrop Furnace and Reinforcement of Trench Covers

The installation of the isothermal chamber had eliminated convenient forklift access to the south side of the 1000-ton forge press. It will now be faster and easier to use the north side of the press for tool changes. This required moving the large Harrop extrusion furnace out of the way and installing structural steel supports under the floor plates that cover the trenches on the north and west sides of the press. Specifications for the furnace move were defined and a quote was obtained for the necessary electrical work. A subcontractor performed required electrical changes. The reinforcement system for the trench covers was designed and fabricated by UES personnel. UES personnel did the actual moving of the furnace.

6.6 Major Press Maintenance

Major press maintenance was performed in December 1996, for the first time since the forge and extrusion presses were installed in Building 655 in 1992. Over 1000 gallons of hydraulic was replaced, pumps were cleaned out, slides adjusted, valves repacked, and heating elements replaced.

6.7 Build Closed Loop Cooling System

A closed loop water cooling system was required for the directional solidification (DS) furnace that was being procured by the Government. UES first considered building a system in-house, similar to several other systems that had been built in-house by other groups in the building. This option would have required substantial labor on the part of contract personnel that would have diverted their efforts from ongoing research activities. It is also not clear that the in-house design would handle the larger heat load required by the DS furnace. UES then investigated buying a ready-built unit. The ready-built unit did not cost substantially more than the component parts for

the in-house unit. The reduced labor on the part of in-house staff resulted in a substantial cost savings. Competitive quotes were solicited, an order was placed, and the system was received and installed.

6.8 Commissioning of the DS Unit

A DS Unit was procured from GTi, Inc. by the Air Force. This unit was installed and commissioned at room 135 in Building 655 in the summer of 1998. This required substantial modifications of the ceiling, argon lines, chilled water supply, and the electrical systems. During commissioning of this unit, several problems affecting the performance of the system were noticed. These include overheating of the radio frequency (RF) coil, restrictions on the range of operating pressures, and the inflexibility of the control software. Working in collaboration with engineers at GTi, Inc. and Air Force personnel, UES scientists/technicians solved these problems and commissioned the DS unit satisfactorily in the fall of 1998. Preliminary experiments on the solidification of Ti-6Al-4V and 304 SS were conducted to assess the influence of dynamic changes in the solidification rate, forced argon cooling and the positioning of the RF coil. These experiments produced bars with severe surface undulations, which would be attributed, in part, to the RF coil design. Additional work continued on the coil design until smooth test bars were obtained

6.9 200-KIP MTS Tool Setup

A set of tooling for conducting ring compression tests was designed, fabricated and installed on the 200-kip MTS test frame in the MPL. This tooling was successfully used for many ring compression tests.

6.10 55-KIP MTS Tool Setup

A new set of compression test tooling was designed, fabricated and installed on the 55-kip MTS test frame. This tooling uses a Danly die set to ensure proper die surface alignment.

6.11 Design, Build, and Install Spinning Mold Casting Device

Dr. Amit Ghosh of the University of Michigan devised an innovative new method of metal casting. Dr. Ghosh was subcontracted with to design and build such a device for installation in the MPL. He completed the design and subcontracted to have the device fabricated in Michigan.

A number of changes were made to the Vacuum Induction Melter in the MPL in anticipation of installing the spinning mold unit inside the VIM chamber. A graphite crucible was installed inside the VIM chamber along with required water, argon, thermocouple, induction and plunger piping and feedthroughs. An induction coil was also fabricated and installed on the crucible with a layer of ceramic felt between the coil and the crucible. The spinning mold device itself was delivered to WPAFB in March 1998. A number of installation tasks were initiated immediately and completed within two weeks, including:

- Reposition one of the four wheels to eliminate interference with the VIM chamber legs.

- Install feet on the bottom of the leveling posts. The original leveling posts, which are used to raise the device upward to mate to the VIM chamber, were simple threaded rods. That design was not workable because the device would walk across the floor as it was raised up. Adding standard machine feet to the bottom of the posts solved this problem.
- Fabricate a new water-cooled flange to weld onto the bottom of the VIM chamber. The original flange would not permit the copper mold to lift out with the spin mold device still attached to the VIM chamber.
- Weld the water-cooled flange onto the bottom of the VIM chamber.
- Redesign and fabricate a new splash plate that attaches to the top of the copper mold. The old splash plate did not adequately protect the main bearing from contamination by falling debris.
- One critical task delayed the startup of the spin mold device. The power required for the spin mold device was originally specified as 240 v 1 phase. That type of power was available at the spin mold location. Shortly before delivery, the power specification was changed to 240 v 3 phase. This type of power was not available at the spin mold location.

After successful installation and startup, the DS unit was used to run a series of experiments on aluminum and titanium.

6.12 Mothballing of Isothermal Chamber

The installation of the isothermal chamber on the 1000-ton forge press was suspended at the Government's request due to a redirection in their research needs. The chamber was taken off of the press, crated up and sent to a long-term storage facility.

7 PUBLICATIONS and PRESENTATIONS

7.1 Publications

UES, Inc. employees or consultants working on the contract published the following papers:

1. S.L. Semiatin and V. Seetharaman, "A Criterion for Intergranular Fracture During Hot Working of a Near Gamma Titanium Aluminide Alloy," *Scripta Mater.*, Vol. 36, p. 291 (1997).
2. P.D. Nicolaou and S.L. Semiatin, "An Analysis of the Effect of Normal Plastic Anisotropy on the Tensile Ductility of Sheet Tension Specimens," *Scripta Mater.*, Vol. 36, p. 83 (1997).
3. P.D. Nicolaou and S.L. Semiatin, "An Investigation of the Effect of Texture on the High-Temperature Flow Behavior of an Orthorhombic Titanium Aluminide Alloy," *Metall. and Mater. Trans. A*, Vol. 28A, p. 885 (1997).
4. V. Seetharaman and S.L. Semiatin, "Analysis of Grain Growth in a Two-Phase Gamma Titanium Aluminide Alloy," *Metall. and Mater. Trans. A*, Vol. 28A, p. 947 (1997).
5. C.M. Lombard, A.K. Ghosh and S.L. Semiatin, "Effect of Microstructure on Cavitation and Failure Behavior During Superplastic Deformation of a Near-Gamma Titanium Aluminide Alloy," *Advances in the Science and Technology of Titanium Processing*, I. Weiss, et al., eds., TMS, Warrendale, PA, p. 161 (1997).
6. S.L. Semiatin, V. Seetharaman, and I. Weiss, Hot Working of Titanium Alloys-An Overview," *Advances in the Science and Technology of Titanium Processing*, I. Weiss, et al., eds., TMS, Warrendale, PA, p. 3 (1997).
7. V. Seetharaman and S.L. Semiatin, "Modeling of Cracking and Cavitation During Hot Working of Gamma Titanium Aluminides," *Modeling of Mechanical Response of Structural Materials*, E.A. Taleff and R.K. Mahidhara, eds., TMS, Warrendale, PA, p. 237 (1997).
8. V. Seetharaman, C.M. Lombard, and S.L. Semiatin, "Phase Stability in a Ti-45.5Al-2Nb-2Cr Alloy," *Advances in the Science and Technology of Titanium Processing*, I. Weiss, et al., eds., TMS, Warrendale, PA, p. 497 (1997).
9. V. Seetharaman and S.L. Semiatin, "Plastic Flow and Microstructure Evolution during Hot Deformation of a Gamma Titanium Aluminide Alloy," *Metall. and Mater. Trans. A*, Vol. 28A, p. 2309 (1997).
10. S.L. Semiatin, J.C. Chesnutt, C. Austin, and V. Seetharaman, "Processing of Intermetallic Alloys," *Structural Intermetallics 1997*, M.V. Nathal, R. Darolia, C.T. Liu, P.L. Martin, D.B. Miracle, R. Wagner, and M. Yamaguchi, eds., TMS Warrendale, PA, p. 263 (1997).
11. S.L. Semiatin, V. Seetharaman, and I. Weiss, "The Thermomechanical Processing of Alpha/Beta Titanium Alloys," *JOM*, Vol. 49, No. 6, p. 33 (1997).

12. P.D. Nicolaou and S.L. Semiatin, "A Theoretical Investigation of the Effect of Materials Properties and Cavity Architecture/Shape on Ductile Failure During the Hot Tension Test," *Metall. and Mater. Trans. A*, Vol. 29A, p. 2621 (1998).
13. S.L. Semiatin, V. Seetharaman, A.K. Ghosh, E.B. Shell, M.P. Simon, and P.N. Fagin, "Cavitation during Hot Tension Testing of Ti-6Al-4V," *Mater. Sci. Eng. A*, Vol. A256, p. 92 (1998).
14. S.L. Semiatin, V. Seetharaman, and I. Weiss, "Hot Workability of Titanium Alloys and Titanium Aluminides – An Overview," *Mater. Sci. Eng.*, A243, p. 1 (1998).
15. V. Seetharaman and S.L. Semiatin, "Intergranular Fracture of Gamma Titanium Aluminides under Hot Working Conditions," *Metall. and Mater. Trans. A*, Vol. 29A, p. 1991 (1998).
16. R.L. Goetz and V. Seetharaman, "Modeling Dynamic Recrystallization Using Cellular Automata," *Scripta Mater.*, Vol. 38, p. 405 (1998).
17. S.L. Semiatin, V. Seetharaman, D.M. Dimiduk, and K.H.G. Ashbee, "Phase Transformation Behavior of Gamma Titanium Aluminide Alloys During Supertransus Heat Treatment," *Metall. and Mater. Trans. A*, Vol. 29A, p. 7 (1998).
18. R.L. Goetz and V. Seetharaman, "Static Recrystallization Kinetics with Homogeneous and Heterogeneous Nucleation using a Cellular Automata Model," *Metall. and Mater. Trans. A*, Vol. 29A, p. 2307 (1998).
19. P.D. Nicolaou and S.L. Semiatin, "The Knoop-Hardness Yield Locus of an Orthorhombic Titanium Aluminide Alloy," *Metall. and Mater. Trans. A*, Vol. 29A, p. 1763 (1998).
20. R.E. Dutton, R.L. Goetz, S. Shamasundar, and S.L. Semiatin, "The Ring Test for P/M Materials," *Trans. ASME, J. Manf. Sci. and Eng.*, Vol. 120, p. 764 (1998).
21. M.K. Alam, S.L. Semiatin and Z. Ali, "Thermal Stress Development During Vacuum Arc Remelting and Permanent Mold Casting of Ingots," *Trans. ASME, J. Manf. Sci. and Eng.*, Vol. 120, p. 755 (1998).
22. P. Ari-Gur and S.L. Semiatin, "Evolution of Microstructure, Macrotexture and Microtexture During Hot Rolling of Ti-6Al-4V," *Mater. Sci. Eng. A*, Vol. A257, p. 118 (1998).
23. S.L. Semiatin, R.L. Goetz, E.B. Shell, V. Seetharaman, and A.K. Ghosh, "Cavitation and Failure During Hot Forging of Ti-6Al-4V," *Metall. and Mater. Trans. A*, Vol. 30A, p. 1411 (1999).
24. E.B. Shell and S.L. Semiatin, "Effect of Initial Microstructure on Plastic Flow and Dynamic Globularization during Hot Working of Ti-6Al-4V," *Metall. and Mater. Trans. A*, Vol. 30A, p. 3219 (1999).

25. S.L. Semiatin, V. Seetharaman, and I. Weiss, "Flow Behavior and Globularization Kinetics during Hot Working of Ti-6Al-4V with a Colony Alpha Microstructure," *Mater. Sci. Eng. A*, Vol. A263, p. 257 (1999).
26. R.E. Dutton, V. Seetharaman, R.L. Goetz, and S.L. Semiatin, "Effect of Flow Softening on Ring Test Calibration Curves," *Mater. Sci. Eng. A*, Vol. A270, p. 249 (1999).
27. R.M. Miller, T.R. Bieler and S.L. Semiatin, "Flow Softening During Hot Working of Ti-6Al-4V With A Lamellar Colony Microstructure," *Scripta Mater.*, Vol. 40, p. 1387 (1998).
28. K. An, K.S. Ravichandran, R.E. Dutton and S.L. Semiatin, "Microstructure, Texture, and Thermal Conductivity of Single-Layer and Multilayer Thermal Barrier Coatings of Y₂O₃-Stabilized Zr₂ and Al₂O₃ Made by Physical Vapor Deposition," *J. Am. Ceram. Soc.*, Vol. 82, p. 399 (1999).
29. S.L. Semiatin, V. Seetharaman, and A.K. Ghosh, "Plastic Flow, Microstructure Evolution, and Defect Formation during Primary Hot Working of Titanium and Titanium Aluminide Alloys with Lamellar Colony Microstructures," *Phil. Trans. R. Soc. Lond. A*, Vol. 357, p. 1487 (1999).
30. K.S. Ravichandran, K. An, R.E. Dutton and S.L. Semiatin, "Thermal Conductivity of Plasma-Sprayed Monolithic and Multilayer Coatings of Alumina and Yttria-Stabilized Zirconia," *J. Am. Ceram. Soc.*, Vol. 82, p. 673 (1999).
31. S.L. Semiatin, V.M. Segal, R.E. Goforth, N.D. Frey, and D.P. DeLo, "Workability of Commercial-Purity Titanium and 4340 Steel during Equal Channel Angular Extrusion at Cold-Working Temperatures," *Metall. and Mater. Trans. A*, Vol. 30A, p. 1425 (1999).
32. V. Seetharaman, R.L. Goetz, and S.L. Semiatin, "Dynamic Globularization of Lamellar Structures in a Near Gamma Titanium Aluminide Alloy," *Recrystallization and Related Phenomena (ReX '99)*, T. Sakai and H.G. Suzuki, eds., The Japan Institute of Metals, Sendai, Japan, p. 869 (1999).
33. P.D. Nicolaou, S.L. Semiatin, and A.K. Ghosh, "An Analysis of the Effect of Cavity Nucleation Rate and Cavity Coalescence on the Tensile Behavior of Superplastic Materials," *Metall. and Mater. Trans. A*, Vol. 31A, p. 1425 (2000).
34. S.L. Semiatin, D.P. DeLo and E.B. Shell, "The Effect of Material Properties and Tooling Design on Deformation and Fracture During Equal Channel Angular Extrusion," *Acta Metallurgica*, Vol. 48, p. 1841 (2000).
35. R.M. Nekkanti, V. Seetharaman, L. Brunke, I. Maartense, D. Dempsey, G. Kozlowski, D. Tomich, R. Biggers, T. Peterson, P. Barnes, and C.E. Oberly, "Development of Nickel Alloy Substrates for Y-Ba-Cu-O Coated Conductor Applications," *IEEE Transactions on Applied Superconductivity*, Vol. 11, No. 1, p. 3321 (2001).
36. S.L. Semiatin and T.R. Bieler, "Effect of Texture Changes on Flow Softening during Hot Working of Ti-6Al-4V," *Metall. and Mater. Trans. A*, Vol. 32A, p. 1871 (2001).

37. S.L. Semiatin and T.R. Bieler, "Effect of Texture and Slip Mode on the Anisotropy of Plastic Flow and Flow Softening during Hot Working of Ti-6Al-4V," *Metall. and Mater. Trans. A*, Vol. 32A, p. 1787 (2001).
38. S.L. Semiatin, P.N. Fagin, M.G. Glavicic, I.M. Sukonnik and O.M. Ivasishin, "Influence of Texture on Beta Grain Growth during Continuous Annealing of Ti-6Al-4V," *Mater. Sci. Eng. A*, Vol. A299, p. 225 (2001).
39. P.N. Fagin, J.O. Brown, T.M. Brown, K.V. Jata, and S.L. Semiatin, "Failure Modes during Equal Channel Angular Extrusion of Aluminum Alloy 2024," *Metall. and Mater. Trans. A*, Vol. 32A, p. 1869 (2001).
40. V. Seetharaman and S.L. Semiatin, "Microstructures and Tensile Properties of Ti-45.5Al-2Nb-2Cr Rolled Sheets," *Mater. Sci. Eng. A*, Vol. A299, p. 195 (2001).
41. S.L. Semiatin, J.O. Brown, T.M. Brown, D.P. DeLo, T.R. Bieler, and J.H. Beynon, "Strain-Path Effects during Hot Working of Ti-6Al-4V with a Colony-Alpha Microstructure," *Metall. and Mater. Trans. A*, Vol. 32A, p. 1556 (2001).
42. R.L. Goetz and S.L. Semiatin, "The Adiabatic Correction Factor for Deformation Heating During the Uniaxial Compression Test," *J. Mater. Eng. and Perf.*, Vol. 10(6), p. 710 (2001).
43. V. Seetharaman and S.L. Semiatin, "Powder Metallurgy of Intermetallic Alloys," *Intermetallic Compounds: Principles & Practice: Vol. 3*, J.H. Westbrook and R.L. Fleischer, eds., John Wiley & Sons, West Sussex, U.K. (2002).

7.2 Presentations

1. "Microstructure Development and Crack Initiation During Deformation Processing of Gamma Titanium Aluminide Alloys," V. Seetharaman, R.L. Goetz, and S.L. Semiatin, Presented by V. Seetharaman, 5th Tri-Service Titanium Contracts Review, WPAFB, 7-9 October 1997.
2. "Deformation and Recrystallization of Titanium Alloys," V. Seetharaman, invited talk delivered at The Ladish Company, Cudahy, WI, November 1998.
3. "Dynamic Globularization of Lamellar Structures in a Near Gamma Titanium Aluminide Alloy," V. Seetharaman, R.L. Goetz, and S.L. Semiatin, Presented by V. Seetharaman at The Fourth International Conference on Recrystallization and Related Phenomena (ReX '99), Tsukuba, Japan, July 1999.
4. "Plastic Flow and Microstructure Development during High Temperature Deformation of a Friction Stir Welded 7050 Aluminum Alloy," V. Seetharaman, K.V. Jata, and S.L. Semiatin, Presented by V. Seetharaman at the Second International Symposium on Friction Stir Welding, Gothenburg, Sweden, June 2000.

7.3 Selected, Limited Distribution Reports

1. “Final Report on Extrusion of Nanophase Al-7.5Mg Tubing,” S.L. Semiatin, R.L. Goetz, J.O. Brown, and P.N. Fagin, “Final Report AFRL/MLLM Report to Dr. Cliff Bampton, Rocketdyne Division, Boeing North American, Inc., 11 February 1999.

8 REFERENCES

- (1) S.L. Semiatin and V. Seetharaman, "A Criterion for Intergranular Fracture During Hot Working of a Near Gamma Titanium Aluminide Alloy," *Scripta Mater.*, Vol. 36, p. 291 (1997).
- (2) V. Seetharaman and S.L. Semiatin, "Analysis of Grain Growth in a Two-Phase Gamma Titanium Aluminide Alloy," *Metall. and Mater. Trans. A*, Vol. 28A, p. 947 (1997).
- (3) V. Seetharaman and S.L. Semiatin, "Modeling of Cracking and Cavitation During Hot Working of Gamma Titanium Aluminides," *Modeling of Mechanical Response of Structural Materials*, E.A. Taleff and R.K. Mahidhara, eds., TMS, Warrendale, PA, p. 237 (1997).
- (4) V. Seetharaman, C.M. Lombard, and S.L. Semiatin, "Phase Stability in a Ti-45.5Al-2Nb-2Cr Alloy," *Advances in the Science and Technology of Titanium Processing*, I. Weiss, et al., eds., TMS, Warrendale, PA, p. 497 (1997).
- (5) V. Seetharaman and S.L. Semiatin, "Plastic Flow and Microstructure Evolution during Hot Deformation of a Gamma Titanium Aluminide Alloy," *Metall. and Mater. Trans. A*, Vol. 28A, p. 2309 (1997).
- (6) V. Seetharaman and S.L. Semiatin, "Intergranular Fracture of Gamma Titanium Aluminides under Hot Working Conditions," *Metall. and Mater. Trans. A*, Vol. 29A, p. 1991 (1998).
- (7) S.L. Semiatin, V. Seetharaman, D.M. Dimiduk, and K.H.G. Ashbee, "Phase Transformation Behavior of Gamma Titanium Aluminide Alloys During Supertransus Heat Treatment," *Metall. and Mater. Trans. A*, Vol. 29A, p. 7 (1998).
- (8) P.D. Nicolaou and S.L. Semiatin, "The Knoop-Hardness Yield Locus of an Orthorhombic Titanium Aluminide Alloy," *Metall. and Mater. Trans. A*, Vol. 29A, p. 1763 (1998).
- (9) V. Seetharaman, R.L. Goetz, and S.L. Semiatin, "Dynamic Globularization of Lamellar Structures in a Near Gamma Titanium Aluminide Alloy," *Recrystallization and Related Phenomena (ReX '99)*, T. Sakai and H.G. Suzuki, eds., The Japan Institute of Metals, Sendai, Japan, p. 869 (1999).
- (10) V. Seetharaman and S.L. Semiatin, "Microstructures and Tensile Properties of Ti-45.5Al-2Nb-2Cr Rolled Sheets," *Mater. Sci. Eng. A*, Vol. A299, p. 195 (2001).
- (11) S.L. Semiatin, V. Seetharaman, A.K. Ghosh, E.B. Shell, M.P. Simon, and P.N. Fagin, "Cavitation during Hot Tension Testing of Ti-6Al-4V," *Mater. Sci. Eng. A*, Vol. A256, p. 92 (1998).

- (12) S.L. Semiatin, R.L. Goetz, E.B. Shell, V. Seetharaman, and A.K. Ghosh, "Cavitation and Failure During Hot Forging of Ti-6Al-4V," *Metall. and Mater. Trans. A*, Vol. 30A, p. 1411 (1999).
- (13) S.L. Semiatin, V. Seetharaman, and I. Weiss, "Flow Behavior and Globularization Kinetics during Hot Working of Ti-6Al-4V with a Colony Alpha Microstructure," *Mater. Sci. Eng. A*, Vol. A263, p. 257 (1999).
- (14) D.P. DeLo, T.R. Bieler, and S.L. Semiatin, "Microstructure and Texture Evolution During Equal Channel Angular Extrusion of Ti-6Al-4V," *Ultrafine Grained Materials*, R.S. Mishra, S.L. Semiatin, C. Suryanarayanan, N.N. Thadhani, and T.C. Lowe, eds., TMS, Warrendale, PA, p. 257 (2000).
- (15) D.P. DeLo and S.L. Semiatin, "Hot Working of Ti-6Al-4V via Equal Channel Angular Extrusion," *Metall. Mater. Trans. A*, Vol. 30A, p. 2473 (1999).
- (16) S.L. Semiatin, J.O. Brown, T.M. Brown, D.P. DeLo, T.R. Bieler, and J.H. Beynon, "Strain-Path Effects during Hot Working of Ti-6Al-4V with a Colony-Alpha Microstructure," *Metall. and Mater. Trans. A*, Vol. 32A, p. 1556 (2001).
- (17) E.B. Shell and S.L. Semiatin, "Effect of Initial Microstructure on Plastic Flow and Dynamic Globularization during Hot Working of Ti-6Al-4V," *Metall. and Mater. Trans. A*, Vol. 30A, p. 3219 (1999).
- (18) S.L. Semiatin, V. Seetharaman, and A.K. Ghosh, "Plastic Flow, Microstructure Evolution, and Defect Formation during Primary Hot Working of Titanium and Titanium Aluminide Alloys with Lamellar Colony Microstructures," *Phil. Trans. R. Soc. Lond. A*, Vol. 357, p. 1487 (1999).
- (19) R.E. Dutton, V. Seetharaman, R.L. Goetz, and S.L. Semiatin, "Effect of Flow Softening on Ring Test Calibration Curves," *Mater. Sci. Eng. A*, Vol. A270, p. 249 (1999).
- (20) R.E. Dutton, R.L. Goetz, S. Shamasundar, and S.L. Semiatin, "The Ring Test for P/M Materials," *Trans. ASME, J. Manuf. Sci. and Eng.*, Vol. 120, p. 764 (1998).
- (21) S.L. Semiatin, D.P. DeLo and E.B. Shell, "The Effect of Material Properties and Tooling Design on Deformation and Fracture During Equal Channel Angular Extrusion," *Acta Metallurgica*, Vol. 48, p. 1841 (2000).
- (22) P.N. Fagin, J.O. Brown, T.M. Brown, K.V. Jata, and S.L. Semiatin, "Failure Modes during Equal Channel Angular Extrusion of Aluminum Alloy 2024," *Metall. and Mater. Trans. A*, Vol. 32A, p. 1869 (2001).
- (23) P.D. Nicolaou and S.L. Semiatin, "An Analysis of the Effect of Normal Plastic Anisotropy on the Tensile Ductility of Sheet Tension Specimens," *Scripta Mater.*, Vol. 36, p. 83 (1997).

- (24) P.D. Nicolaou and S.L. Semiatin, "An Investigation of the Effect of Texture on the High-Temperature Flow Behavior of an Orthorhombic Titanium Aluminide Alloy," *Metall. and Mater. Trans. A*, Vol. 28A, p. 885 (1997).
- (25) S.L. Semiatin, P.N. Fagin, M.G. Glavicic, I.M. Sukonnik and O.M. Ivasishin, "Influence of Texture on Beta Grain Growth during Continuous Annealing of Ti-6Al-4V," *Mater. Sci. Eng. A*, Vol. A299, p. 225 (2001).
- (26) R.L. Goetz and V. Seetharaman, "Static Recrystallization Kinetics with Homogeneous and Heterogeneous Nucleation using a Cellular Automata Model," *Metall. and Mater. Trans. A*, Vol. 29A, p. 2307 (1998).
- (27) R.L. Goetz and V. Seetharaman, "Modeling Dynamic Recrystallization Using Cellular Automata," *Scripta Mater.*, Vol. 38, p. 405 (1998).
- (28) V. Seetharaman and S.L. Semiatin, "Effect of the Lamellar Grain Size on Plastic Flow Behavior and Microstructure Evolution during Hot Working of a Gamma Titanium Aluminide Alloy," *Metall. and Mater. Trans. A*, Vol. 33A, p. 3817 (2002).
- (29) V. Seetharaman, R.L. Goetz, and S.L. Semiatin, "Dynamic Globularization of Lamellar Structures in a Near Gamma Titanium Aluminide Alloy," *The Fourth International Conference on Recrystallization and Related Phenomena*, Edited by T. Sakai and H.G. Suzuki, The Japan Institute of Metals, p. 869 (1999).
- (30) P.D. Nicolaou and S.L. Semiatin, "A Theoretical Investigation of the Effect of Materials Properties and Cavity Architecture/Shape on Ductile Failure During the Hot Tension Test," *Metall. and Mater. Trans. A*, Vol. 29A, p. 2621 (1998).
- (31) P.D. Nicolaou, S.L. Semiatin, and A.K. Ghosh, "An Analysis of the Effect of Cavity Nucleation Rate and Cavity Coalescence on the Tensile Behavior of Superplastic Materials," *Metall. and Mater. Trans. A*, Vol. 31A, p. 1425 (2000).
- (32) R.L. Goetz and S.L. Semiatin, "The Adiabatic Correction Factor for Deformation Heating During the Uniaxial Compression Test," *J. Mater. Eng. and Perf.*, Vol. 10(6), p. 710 (2001).
- (33) R.M. Nekkanti, V. Seetharaman, L. Brunke, I. Maartense, D. Dempsey, G. Kozlowski, D. Tomich, R. Biggers, T. Peterson, P. Barnes, and C.E. Oberly, "Development of Nickel Alloy Substrates for Y-Ba-Cu-O Coated Conductor Applications," *IEEE Transactions on Applied Superconductivity*, Vol. 11, No. 1, p. 3321 (2001).
- (34) D.R. Barker, R.L. Goetz, and P. Fagin, "Characterization of the Forging Die-Workpiece Interface Friction and Heat Transfer between Alloy Steel and Alloy Ti-6Al-4V," for Concurrent Technologies Corporation, Johnstown, PA, UES, Inc. Project No. R188-013, CRADA No. 99-025-ML-01, AF Contract No. F33615-96-C-5251, August 31, 2000.

- (35) V. Seetharaman, R.L. Goetz, and S.L. Semiatin, "Microstructure Development And Crack Initiation During Deformation Processing Of Gamma Titanium Aluminide Alloys," was presented at the 5th Tri-Service Titanium Contracts Review, WPAFB, 7-9 October 1997.
- (36) Laasraoui and J.J. Jonas, "Recrystallization of Austenite after Deformation at High Temperatures and Strain Rates – Analysis and Modeling," *Metall. and Mater. Trans. A*, Vol. 22A, p. 151 (1991).
- (37) W. Roberts, "Dynamic Changes That Occur During Hot Working and Their Significance Regarding Microstructural Development and Hot Workability," in *Deformation, Processing, and Structure*, G. Krauss, ed., ASM, p. 109 (1984).

APPENDIX
Cooperative Technology Clusters (CTeC)

Pilot Program

Final Report

for the period
5 March 1999 to 23 August 2000

Douglas R. Barker
Frank J. Scheltens

UES, Inc.
Materials and Processes Division
4401 Dayton-Xenia Road
Dayton, Ohio 45432-1894

TABLE OF CONTENTS

<u>Section</u>	<u>Page</u>
LIST OF FIGURES	83
LIST OF TABLES	85
FOREWORD	86
A1. EXECUTIVE SUMMARY	87
A2. BACKGROUND	88
A2.1 AIR FORCE RESEARCH LABORATORY / AFRL	88
A2.2 SPECIFIC AFRL CAPABILITIES UTILIZED FOR THIS PROGRAM	88
A2.3 CONVERGING NEEDS OF MILITARY AND INDUSTRY	89
A2.4 PROGRAM OBJECTIVES	89
A2.5 PROGRAM ACCOMPLISHMENTS	90
A3. EXTRUSION DIE DESIGN	91
A3.1 PARTICIPANTS AND FACILITIES	91
A3.2 OBJECTIVE	91
A3.3 BACKGROUND.....	91
A3.4 TECHNICAL TASK	91
A3.5 BENEFITS TO THE CLUSTER MEMBERS	91
A3.6 BENEFITS TO THE AIR FORCE.....	92
A3.7 RESULTS	92
A4. CASTING POROSITY STUDY	95
A4.1 PARTICIPANTS AND FACILITIES	95
A4.2 OBJECTIVE	95
A4.3 BACKGROUND.....	95
A4.4 TECHNICAL TASKS.....	95
A4.5 BENEFITS TO THE CLUSTER MEMBERS	96
A4.6 BENEFITS TO THE AIR FORCE.....	96
A4.7 RESULTS	96
A5. EXTRUSION AND CHARACTERIZATION OF AL-FLYASH COMPOSITE	98
A5.1 PARTICIPANTS AND FACILITIES	98
A5.2 OBJECTIVE	98
A5.3 BACKGROUND.....	98
A5.4 TECHNICAL TASK	98
A5.5 BENEFITS TO THE CLUSTER MEMBERS	99
A5.6 BENEFITS TO THE AIR FORCE.....	99
A5.7 RESULTS	99
A6. CASTING SIMULATION TRAINING SEMINAR.....	101
A6.1 PARTICIPANTS AND FACILITIES	101
A6.2 OBJECTIVE	101
A6.3 BACKGROUND.....	101
A6.4 TECHNICAL TASK	101
A6.5 BENEFITS TO THE CLUSTER MEMBERS	101
A6.6 BENEFITS TO THE AIR FORCE.....	102
A6.7 RESULTS	102
A7. SOLIDIFICATION MODELING OF ALUMINUM CASTING	103

A7.1	PARTICIPANTS AND FACILITIES	103
A7.2	OBJECTIVE	103
A7.3	BACKGROUND.....	103
A7.4	TECHNICAL TASK	103
A7.4.1	<i>Construction of the Cummins 1514 Casting</i>	103
A7.4.2	<i>Creation of the FEM</i>	104
A7.4.3	<i>Process Setup</i>	104
A7.4.4	<i>Analysis and Postprocessing</i>	104
A7.5	BENEFITS TO THE CLUSTER MEMBERS	104
A7.6	BENEFITS TO THE AIR FORCE.....	104
A7.7	RESULTS	105
A7.7.1	<i>Summary of Results</i>	105
A7.7.2	<i>Implications of Results</i>	105
A7.7.3	<i>Fluid Solution</i>	106
A7.7.4	<i>Thermal Solution</i>	106
A7.7.5	<i>Conclusions</i>	106
A8.	STEEL CASTING HEAT TREATMENT EVALUATION	119
A8.1	PARTICIPANTS AND FACILITIES	119
A8.2	OBJECTIVE	119
A8.3	BACKGROUND.....	119
A8.4	TECHNICAL TASK	119
A8.5	BENEFITS TO THE CLUSTER MEMBERS	119
A8.6	BENEFITS TO THE AIR FORCE.....	119
A8.7	RESULTS	120
A9.	ALUMINUM SQUEEZE CASTING DEFECTS.....	127
A9.1	PARTICIPANTS AND FACILITIES	127
A9.2	OBJECTIVE	127
A9.3	BACKGROUND.....	127
A9.4	TECHNICAL TASK	127
A9.5	BENEFITS TO THE CLUSTER MEMBERS	127
A9.6	BENEFITS TO THE AIR FORCE.....	128
A9.7	RESULTS	128
A10.	FORGEABILITY OF AL-FLYASH COMPOSITE BRAKE ROTOR	130
A10.1	PARTICIPANTS AND FACILITIES	130
A10.2	OBJECTIVE	130
A10.3	BACKGROUND.....	130
A10.4	TECHNICAL TASK	130
A10.5	BENEFITS TO THE CLUSTER MEMBERS	130
A10.6	BENEFITS TO THE AIR FORCE.....	131
A10.7	RESULTS	131
A11.	STAINLESS STEEL CASTING INCLUSIONS	132
A11.1	PARTICIPANTS AND FACILITIES	132
A11.2	OBJECTIVE	132
A11.3	BACKGROUND.....	132
A11.4	TECHNICAL TASK	132
A11.5	BENEFITS TO THE CLUSTER MEMBERS	132

A11.6 BENEFITS TO THE AIR FORCE.....	132
A11.7 RESULTS	133

List of Figures

	<u>Page</u>
Figure A-1. Star Die and Backup Tooling.....	93
Figure A-2. Extrusions Made Using Star Die in 700-Ton Extrusion Press at AFRL.....	93
Figure A-3. A Series of Computer Tomography (CT) Scans of a Small Piece.....	96
Figure A-4- Medium-Resolution CT Scans (LAMDA) of an Entire Densel 2 Processed Part.....	97
Figure A-5: Series of Optical Micrographs Taken From the 5 Percent Extrusion.....	100
Figure A-6. Training Seminar at AFRL in Casting Simulation Modeling	102
Figure A-7. Initial Casting Design.....	108
Figure A-8. Modified Casting Design	109
Figure A-9. Temperature Plot Showing Free Surface Front at 7.7 Seconds	110
Figure A-10. Temperature Plot Showing Free Surface Front at 21.4 Seconds	110
Figure A-11. Temperature Plot Showing Free Surface Front at 31.2 Seconds	111
Figure A-12. Pressure Plot Showing Free Surface Front at 31.2 Seconds	111
Figure A-13. Fraction Solid Plot with Cutoff = 65 Percent at 57.1 Seconds.....	112
Figure A-14. Fraction Solid Plot with Cutoff = 65 Percent at 73.1 Seconds.....	112
Figure A-15. Fraction Solid Plot with Cutoff = 65 Percent at 92.7 Seconds.....	113
Figure A-16. Fraction Solid Plot with Cutoff = 65 Percent at 119.7 Seconds.....	113
Figure A-17. Temperature Plot Showing Free Surface Front at 6.0 Seconds	114
Figure A-18. Temperature Plot Showing Free Surface Front at 16.6 Seconds.	114
Figure A-19. Temperature Plot Showing Free Surface Front at 31.7 Seconds	115
Figure A-20. Pressure Plot Showing Free Surface Front at 28.4 Seconds	115
Figure A-21. Fraction Solid Plot with Cutoff = 65 Percent at 53.3 Seconds.....	116
Figure A-22. Fraction Solid Plot with Cutoff = 65 Percent at 69.0 Seconds.....	116
Figure A-23. Fraction Solid Plot with Cutoff = 65 Percent at 86.5 Seconds.....	117
Figure A-24. Fraction Solid Plot with Cutoff = 65 Percent at 105.7 Seconds.....	117
Figure A-25. Fraction Solid Plot with Cutoff = 65 Percent at 132.2 Seconds.....	118
Figure A-26. Sectioned Castings	120
Figure A-27. Microstructure 5 mm from the Bottom Edge of Casting #1 (left) and Casting #2 (right)	121
Figure A-28. Microstructure 10 mm from the Bottom Edge of Casting #1 (left) and Casting #2 (right)	121
Figure A-29. Microstructure 20 mm from the Bottom Edge of Casting #1 (left) and Casting #2 (right)	122
Figure A-30. Microstructure 30 mm from the Bottom Edge of Casting #1 (left) and Casting #2 (right)	122
Figure A-31. Microstructure 35 mm from the Bottom Edge (near the center) of Casting #1 (left) and Casting #2 (right)	123
Figure A-32. 35mm (center) Casting #1 on (left), Casting #2 (right) Lower Mag.....	123
Figure A-33. 35mm (center) Casting #1 (left), Casting #2 (right) macro	124
Figure A-34. Hardness Data for Casting #1 Plotted Against the Hardenability Curves for Two Different 8630 Alloys: AISI-SAE 8630H and AISI-SAE 86B30H	125
Figure A-35. Hardness Data for Casting #2 Plotted Against the Hardenability Curves for Two Different 8630 alloys: AISI-SAE 8630H and AISI-SAE 86B30H.....	126
Figure A-36. SEM of Fractured Wheel Rim Produced by the Squeeze Casting Method.....	128

Figure A-37. SEMs of a Defect in the Fracture Surface (left side) and of the Clean Fracture Surface (right side).....	129
Figure A-38. Upset Forgings of 6061Al and of 6061Al + 15wt% 250- μ m Flyash Composite ..	131
Figure A-39. Stainless Steel Investment Casting.....	134
Figure A-40. EDS Compositional Data of Stainless Steel Casting Material.....	134
Figure A-41. SEI of Casting Inclusion, 30x	135
Figure A-42. BEI of Casting Inclusion, 30x.....	135
Figure A-43. SEI of the Sectioned Interface Between Casting (above) and Inclusion (below), 30x	136
Figure A-44. BEI of the Sectioned Interface Between Casting (above) and Inclusion (below), 30x	136
Figure A-45. SEI of Sectioned Casting Inclusion, 1000x.....	137
Figure A-46. BEI of Sectioned Casting Inclusion, 1000x	137
Figure A-47. EDS Compositional Data from the Dark Phase of the Sectioned Casting Inclusion	138
Figure A-48. EDS Compositional Data from the Light Phase of the Sectioned Casting Inclusion	138
Figure A-49. BEI of FeTi Alloying Compound, 1000x	139
Figure A-50. EDS Compositional Data from the Dark Phase of the FeTi	139
Figure A-51. EDS Compositional Data from the Light Phase of the FeTi.....	140
Figure A-52. EDS Compositional Data from the Grey phase of the FeTi.....	140

List of Tables

	<u>Page</u>
Table A-1. Star Die Extrusion Conditions	94

Foreword

This report was prepared by Douglas Barker and Frank Scheltens of the Materials and Processes Division of UES, Inc., Dayton, Ohio under contract from the EMTEC, Dayton, Ohio and from the U.S. Air Force. Robert Shinkle was the EMTEC Program Manager. Daniel Evans was the U.S. Government Engineer who spearheaded the contractual and funding efforts that were necessary to make this program possible.

The research reported herein was conducted primarily by UES personnel working at the AFRL at WPAFB, Ohio. The only exception was the solidification-modeling task, which was conducted by UES Software personnel working at the UES main office.

The work was funded by the Air Force under contract no. F33615-96-C-5251 and by the State of Ohio Technology Action Fund.

A1. Executive Summary

A critical need exists in the U.S. military for rapid development of new materials and materials processing technology in an uncertain international environment where streamlined turn-around times to deployment can be critical. Private industry in the U.S. has a parallel need to minimize the time and cost from research to commercialization. Both industry and U.S. military interests can be best served by establishing research and development teams between industry, the technology research community and AFRL in key predefined technology project areas.

The U.S. has invested substantially over the years in AFRL at WPAFB, Dayton, Ohio to build up the world's premier research centers in materials and materials processing technology as well as in microstructural characterization. The highly skilled research teams at AFRL have unique equipment and facilities at their disposal. In the past, these researchers have focused their efforts on making U.S. military aircraft the best in the world. By turning a portion of their efforts to assisting U.S. industries, we can now get a further payback on our taxpayer dollars by increasing the world competitiveness of our industries and thus increasing the standard of living of the American people.

In the CTec, UES, Inc. and EMTEC teamed up to bring private industry together with AFRL. UES is the onsite contractor that operates many of the relevant facilities at AFRL. UES scientists and technicians performed most of the actual research. EMTEC is a non-profit organization whose mission is to strengthen private industry through technology innovations. In the past ten years, EMTEC has directed over \$38 million in collaborative R&D projects with its member companies. EMTEC acted as the collaborative facilitator, forming clusters of companies with common research interests.

EMTEC used its experience and contacts in private industry to bring together groups of companies that had common research needs. Each of these clusters, in cooperation with AFRL and UES personnel, formulated a research task that utilized the unique capabilities of AFRL to increase the competitiveness of the members of the cluster. UES personnel then conducted the work at the AFRL facilities.

The CTec concept has substantial benefits for the Air Force and the participating companies:

- The Air Force benefits from forming closer ties between its researchers and private industry and from increasing the efficient utilization of its facilities and personnel. The result is an increase in defense readiness and a decrease in the cost of performing ongoing DoD research.
- Private industry benefits from being able to utilize the unique capabilities of the personnel and facilities that are already in place at AFRL. The result is increased competitiveness that gives U.S. companies an edge in the world market.

The goal of this pilot program was to demonstrate the contractual, financial and technical structure of the full-scale program and to show how the research capabilities of AFRL can be brought to bear on an industrial project. This goal was fully achieved. The success of this pilot program has resulted in a full-scale follow-on program. The experience gained in the pilot

program aided in the development of the complex contractual and funding mechanisms that are needed to institutionalize CTeC as a long-term program that will benefit both industry and the Air Force.

A2. Background

A2.1 Air Force Research Laboratory / AFRL

The Materials and Manufacturing Directorate of the AFRL has played a critical role in giving the U.S. Air Force a competitive edge over its adversaries for more than 80 years. The Directorate has led the aerospace industry in research and development of materials and manufacturing processes. It has provided support to the Air Force in selecting new materials and processes and in quick-reaction support to field organizations.

The unique capabilities of the Directorate have been made possible by a substantial taxpayer investment in facilities and equipment and by developing and retaining a highly skilled workforce. The primary laboratory located at WPAFB near Dayton, Ohio has more than one-half million square feet of modern research facilities. The permanent staff of over 400 government scientists and engineers is augmented by an equal number of onsite contractors.

The nature of the research and development conducted by AFRL and the Materials and Manufacturing Directorate in particular has always been focused on the goal of seeing the products of its research incorporated into actual manufacturing processes and flying aircraft. As a result, the Directorate has become accustomed to working closely with the aerospace industry. In recent years, as defense budgets have become leaner, there has been an increasingly explicit thrust toward manufacturability, affordability and maintainability. This thrust has resulted in an increased need to form close ties with industry and to help solve industrial problems in order to reduce the cost of current Air Force systems and to incorporate industrial considerations into future research.

A2.2 Specific AFRL Capabilities Utilized for this Program

This pilot program focused on two specific groups within AFRL. They were the MPL and the Microstructural Characterization Facility (MCF). Both of these groups have unique capabilities that could be used immediately for projects that are of concern to industry. In fact, some of these capabilities are already called upon regularly by other government organizations and DoD contractors.

The MPL is equipped with pilot plant scale metal forming and metal casting equipment. The major pieces include a 1000-ton forge press and a 700-ton extrusion press. The MPL is staffed by a team of UES, Inc. personnel who have extensive experience in a wide variety of metal processing applications. In addition to their own direct experience, they are able to draw upon a vast database of in-house processing records from the last 40 years that range from simple aluminum alloys to exotic materials.

The MCF is equipped with state-of-the-art electron-optical instrumentation, a full set of ancillary sample preparation facilities, light optical instrumentation (including confocal

capabilities), and extensive metallographic preparation facilities. The flagship instrument among the electron microscopes is a fully outfitted analytical Philips CM200 200-kV super twin-alpha field emission gun transmission electron microscope (FEG TEM) equipped with a fully computer controlled, high tilt ($\pm 40^\circ$), high-stability eucentric compustage enabling both high-resolution (HREM), and analytical energy dispersive spectroscopy (EDS) imaging performance. Two additional conventional TEMs, three field emission scanning electron microscopes (SEMs), and two electron microprobes round out the extensive instrumentation available in the MCF. The MCF is staffed by a team of UES scientists and technicians with comprehensive experience at applying all of the aforementioned techniques to the solution of problems in materials science.

A2.3 Converging Needs of Military and Industry

The needs of the U.S. Air Force have undergone a dramatic transformation in recent years. An uncertain and constantly changing international environment has created a critical requirement for rapid development and procurement of new materials and materials processing technology. Gone are the days when our adversary was so well defined that the identification of a new need and the deployment of weapons systems could be spread out over many years. It has become vital to reduce the turnaround time from concept to deployment of new technologies in order to gain both strategic advantage and cost containment.

Private industry in the U.S. has a parallel need to minimize the time and cost from research to commercialization. The financial success and the very survival of many U.S. companies depends on their ability to utilize superior technology in both their products and their manufacturing processes. To survive in a global economy, in which many of our competitors have substantially lower labor and environmental compliance costs, we must be able to amplify the efforts of our U.S. workforce by applying superior technology. This is not a goal that can be accomplished by a one-time application of R&D. As successful companies know, staying ahead of the competition requires an ongoing effort.

Both industry and U.S. military interests can be served best by establishing research and deployment teams between industry, the technology research community and the AFRL in key predefined technology areas.

A2.4 Program Objectives

The overall goal of the CTeC Pilot Program was to create an ongoing relationship between the AFRL and private industry that benefits both the direct participants and the American economy. The program objectives were to achieve the following:

- Increase the competitiveness of U.S. industry by gaining access to technologies and R&D capabilities that have been previously unavailable.
- Increase defense readiness/preparedness by forging a closer working relationship between AFRL and industry.
- Increase defense readiness/preparedness directly by transferring technology and thus increasing the technical capability of American industry.

- Decrease the cost to the Air Force of conducting its own research by increasing the efficient utilization of existing facilities and personnel. This will be accomplished by spreading the costs of facility operation, maintenance and modernization over a larger operational pool.
- Preserve the critical mass of activity that is required at AFRL for conducting world class materials and processing research in multiple fields.
- Maintain infrastructure and human resources at AFRL with a diversified funding base.

A2.5 Program Accomplishments

The CTeC Pilot Program accomplished its goals through success in three major areas: contractual, financial and technical. Contractually, the program developed an initial mechanism for the Air Force, UES and EMTEC to work together with industry. That experience was then used to develop a mature mechanism based upon a Partnership Intermediary Agreement and Cooperative Test Agreement that was later used for the follow-on program. Financially, the program demonstrated how Federal dollars could be enhanced with State of Ohio Technical Action Fund dollars. Technically, and most importantly for the participants, the program successfully tackled nine distinct industrial projects using the personnel and facilities of the MPL and the MCF.

Each of the nine technical projects is detailed in the following sections.

A3. Extrusion Die Design

A3.1 Participants and Facilities

Facilities Utilized:

95% MPL: 700-ton extrusion press
5% MCF: Metallographic analysis

AFRL Participants:

UES, Inc (Dayton, OH) on-site contractor

Cluster Members:

TechnoSoft Inc. (Cincinnati, OH) for die design
General Extrusion Inc. (Youngstown, OH) for follow-on testing
The Werner Company (Youngstown, OH) for follow-on testing
Other members of Aluminum Extrusion Network (Youngstown, OH)
Ohio University (Athens, OH)
Youngstown State University (Youngstown, OH)
EMTEC (Dayton, OH) as facilitator.

A3.2 Objective

Evaluate and calibrate a software system developed by TechnoSoft for the computer-aided design and manufacturing of extrusion dies.

A3.3 Background

A software system for computer aided design and manufacture of extrusion dies was developed by TechnoSoft under EMTEC core technology project CT-44. A review of that project by industry and members of the Aluminum Extrusion Network concluded that significant value and opportunity exists for using this software for a competitive advantage. The software must be tested and its design algorithms validated before it can be introduced into an industrial setting.

A3.4 Technical Task

TechnoSoft designed one die representing the complexity of features commonly required in aluminum extrusion. UES worked with TechnoSoft to incorporate these die designs into the 700-ton extrusion press tooling and to formulate a realistic test plan. A machine shop fabricated the dies using computer numerical control files generated by the TechnoSoft software system. UES conducted a series of extrusions, with intermediate reworks of the die. Extrusion results were evaluated and then used to calibrate the algorithms that are at the heart of the TechnoSoft die design methodology.

A3.5 Benefits to the Cluster Members

Conducting evaluation tests at AFRL was a superior method of evaluating the die design system for two reasons. First, it was more cost effective to conduct trials on the AFRL pilot plant scale extrusion press than to immediately scaleup to commercial size. Second, it was more effective to

conduct trials in the laboratory environment at AFRL, where the entire extrusion process can be closely monitored and expert personnel from multiple fields are only a few steps away.

A3.6 Benefits to the Air Force

In the short term, AFRL personnel benefited by participating and staying abreast of the state-of-the-art in extrusion technology. Additionally, AFRL will receive a perpetual, royalty-free license for the developed die design software, including installation, maintenance and updates. In the long term, the improvement of extrusion technology will contribute to reduced cost of Air Force weapon systems.

A3.7 Results

A meeting was held at AFRL with pertinent TechnoSoft and EMTEC decision makers (management and technical) to formulate the technical work plan and schedule. TechnoSoft briefed their die design approach. UES briefed AFRL capabilities and general working requirements of the 700-ton horizontal extrusion press to be used in the project. A determination was made on how the TechnoSoft designed die would be incorporated into the existing tooling system of the extrusion press. The machining expert from Browder Tool Company discussed machining details for the dies. A star die and backup tooling were fabricated by Die Engineering Services and heat treated (Figure A-1). Some rework of the backup tooling was required after receipt at UES to correct misalignment between the die and the backup tooling. A typical aluminum alloy, 6063 Al, which is used in commercial extrusion shops was specially purchased for this project. To check for press capacity, a trial extrusion of the material was made through a round-to-round shear die at the same reduction ratio as the star die. This extrusion went at less than 200 tons on the 700-ton press. The star die was then used to extrude three billets. All of the extrusions were successful. The products were extremely straight (Figure A-2). The surface finish was not acceptable for ready to use commercial product. After discussions with Cliff Lotzenhiser (an aluminum extrusion industry consultant), a fourth extrusion was performed without lubrication. This extrusion had a good surface finish. Extrusion conditions for the four extrusions are summarized in Table A-1.



Figure A-1. Star Die and Backup Tooling



Figure A-2. Extrusions Made Using Star Die in 700-Ton Extrusion Press at AFRL

Table A-1. Star Die Extrusion Conditions

Extrusion Number	13,460	13,461	13,462	13,478
Material	AA6063 Al Alloy	AA6063 Al Alloy	AA6060 Al Alloy	AA6063 Al Alloy
Billet Diameter	2.950"	2.950"	2.950"	2.950"
Billet Nose	0.125" x 45°	0.125" x 45°	0.125" x 45°	0.125" x 45°
Container Temperature	750°F	750°F	750°F	750°F
Container Size (Area)	3.072" (7.412 sq. in.)	3.072" (7.412 sq. in.)	3.072" (7.412 sq. in.)	3.072" (7.412 sq. in.)
Die Ratio	Star	Star	Star	Star
Die Facing	Bare	Bare	Bare	Bare
Die Temperature	750°F	750°F	750°F	750°F
Billet Temperature	960°F	960°F	960°F	960°F
Billet Heat Time	2 hours	2 hours	2 hours	1.5 hours
Billet Lube	Deltaforge 144	Deltaforge 144	Deltaforge 144	Bare
Billet Lube Thickness	0.010"	0.010"	0.010"	
Billet Lube By	Brush	Brush	Brush	
Max. Load (Max. pressure)	238.1 Tons (64,247 psi)	205.2 Tons (55,370 psi)	187.6 Tons (50,621 psi)	Not Recorded
Extrusion Length	176" (14'8")	176" (14'8")	176" (14'8")	151" (12'7")
Extrusion Diameter	Y	Y	Y	Y
Final Extrusion Radio	--- (20.8)	--- (20.8)	--- (20.8)	--- (20.8)
Billet Length	9"	9"	9"	8"
Carbon Block	1.2"	1.2"	1.2"	1.5"
Steel Block	1.8"	1.8"	1.8"	2.0"
Die Type	Shear	Shear	Shear	Shear
Die After	Good	Good	Good	
Billet Heating	Extrusion	Extrusion	Extrusion	Extrusion
Die Lube	Necrolene	Necrolene	Necrolene	Bare
Container Lube	Fiske 604	Fiske 604	Fiske 604	Bare
Ram Speed (Extrudate Speed)	60 ipm (104 fpm)	60 ipm (104 fpm)	60 ipm (104 fpm)	60 imp (104 fpm)
Valve Setting	---	---	---	---
Extrusions Description	Good	Good	Good	Fair
Extrusion Nose Burst	0	0	0	0
Extrusion Suckin	---	---	---	6"
Quench	Air Cooled	Air Cooled	Air Cooled	Air Cooled
Comment	Extrudate bent during removal from runout tube	Some tearing on the leg of Y		Twist in extrusion

A4. Casting Porosity Study

A4.1 Participants and Facilities

Facilities Utilized:

100% MCF: Metallographic analysis
Electron optical analysis

AFRL Participants:

UES, Inc (Dayton, OH) on-site contractor

Cluster Members:

Bodycote IMT, Inc. (Madison, OH)
Delphi Automotive Systems (Moraine, OH)
Amcast (Dayton, OH)
A&B Foundry
Funk Finecast
Lester Precision Casting
Lodi Foundry
EMTEC (Dayton, OH) as facilitator.

A4.2 Objective

Evaluate the effectiveness of a new, low-cost process for closing porosity in aluminum die castings.

A4.3 Background

Die casting is a common manufacturing method that can have significant price advantages over all other fabrication processes. Unfortunately, die casting can suffer from porosity in the final product. This is a particularly widespread problem in the manufacture of aluminum compressor housings for the automotive industry. Sealing the pores in die cast compressor housings is currently a complex and costly process that has severe waste disposal problems due to the chemical sealant involved. A new method of low cost HIP called the Densel 2 process is being developed by Bodycote. The Densel 2 process would reduce the cost and complexity of sealing the pores and would completely eliminate the waste disposal problems.

A4.4 Technical Tasks

Bodycote provided aluminum die cast compressor housings that had been identified as having porosity in both as-cast and post Densel 2 conditions. UES evaluated which characterization methods would be most appropriate to characterize the porosity and then conducted that characterization. The first goal of the characterization was to understand the nature and cause of the porosity itself. The second goal was to determine the effectiveness of the Densel 2 process at closing this porosity.

A4.5 Benefits to the Cluster Members

Sealing the porosity in aluminum compressor housings with the Densel 2 process has significant cost, simplicity and environmental advantages over the polymer impregnation process that was currently being used. Before the new process could be introduced on a commercial scale, its impact on porosity had to be fully characterized. The facilities and personnel at AFRL are uniquely qualified to conduct this type of a study, due to extensive capabilities in both characterization and processing.

A4.6 Benefits to the Air Force

AFRL personnel benefited by participating and staying abreast of the development of a new, low cost approach to eliminating casting defects. The Air Force may benefit from the future application of this technique to noncritical components.

A4.7 Results

Both as-cast and Densel 2 processed parts were supplied by Bodycote to AFRL. High-resolution microscans (Figure A-3) were taken of small sections cut from the same location on both parts – the corner near the gas inlet. The scans showed massive porosity in the as-cast part and no visible porosity in the Densel 2 part. Medium-resolution scans were taken with the LAMDE instrument to test the practicality and usefulness of scanning the entire part. Larger pores were clearly visible and some areas of where high densities of subresolution pores could be detected.

Based on the successful use of the LAMDE instrument, five scans were taken through an entire Densel 2 processed part that had failed a leak test after the process. As seen in Figure A-4, no clear paths to the surface were found, although several internal pores were located which may have unseen routes to surface.

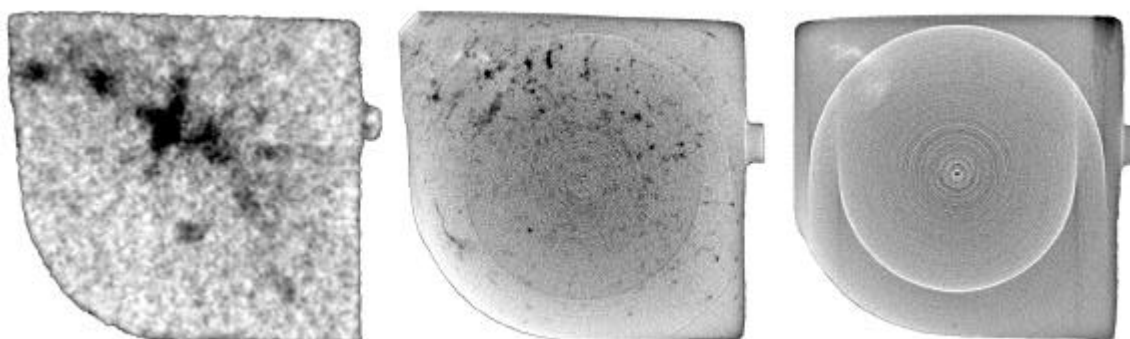


Figure A-3. A Series of Computer Tomography (CT) Scans of a Small Piece

Note: Sectioned from the same location of an as-cast part (left and center) and a post-Densel 2 processed part (right). The image on the left is a medium-resolution LAMDE scan that demonstrates the feasibility of using the LAMDE instrument for inspection of an entire part. The images in the center and on the right are high-resolution microscans that conclusively demonstrate that the Densel 2 process successfully closes internal porosity.

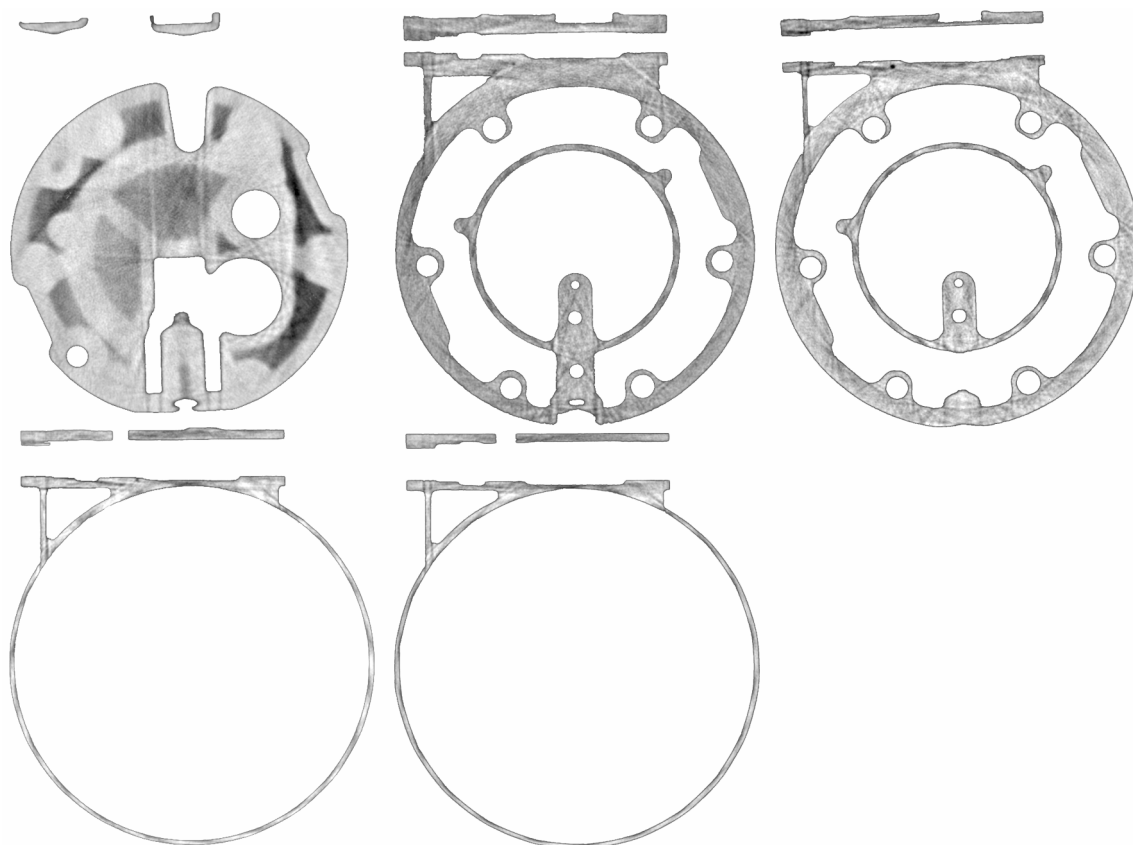


Figure A-4- Medium-Resolution CT Scans (LAMDA) of an Entire Densel 2 Processed Part

Note: A single internal pore is visible in the upper left corner of second, third and fourth scans, but no apparent leak path to the surface is visible.

A5. Extrusion and Characterization of Al-flyash Composite

A5.1 Participants and Facilities

Facilities Utilized:

80%	MPL:	700-ton extrusion press
20%	MCF:	Metallographic analysis Electron optical analysis

AFRL Participants:

UES, Inc (Dayton, OH) on-site contractor

Cluster Members:

Thompson-Aluminum Casting Co. (Cleveland, OH)
ECK Industries, Inc. (Manitowoc, WI)
CHL Microspheres, Inc (Helenwood, TN)
Ohio Edison (Akron, OH)
Dayton Power and Light Corp. (Dayton, OH)
University of Wisconsin (Milwaukee, WI)
Oak Ridge National Laboratory (Oak Ridge, TN)
EMTEC (Dayton, OH) as facilitator.

A5.2 Objective

Study the extrusion behavior of Al-flyash composite.

A5.3 Background

There has been interest for many years in developing a commercially viable method of introducing flyash into aluminum alloys to reduce the cost of raw materials. Flyash is a waste product of coal-fired power generating plants. Compared to an equal volume of aluminum alloy, it is almost a free raw material. By adding 20 volume percent flyash to an aluminum alloy, the cost of the raw materials is reduced as much as 19 percent. A new method for production of Al-flyash composite has been developed under EMTEC CT60. The question is how successfully can the cast ingot material be extruded. Extrudability is a key factor in actual commercialization of the material.

A5.4 Technical Task

Ingots of various aluminum alloys and flyash compositions were cast by Thompson-Aluminum Castings. UES extruded ingots on the 700-ton extrusion press at AFRL. The effect of preheat temperature, extrusion ratio and ram velocity on the quality of the product were evaluated. UES conducted metallographic and electron optical analysis at AFRL to determine the effect of extrusion on the distribution of the flyash particles.

A5.5 Benefits to the Cluster Members

Conducting evaluation tests at AFRL was a superior method of evaluating the extrusion behavior of various Al-flyash alloys for two reasons. First, it was more cost effective to conduct trials on the AFRL pilot plant scale extrusion press than to immediately scaleup to commercial size. Second, it was more effective to conduct trials in the laboratory environment at AFRL, where the entire extrusion process can be closely monitored and expert personnel from multiple fields are only a few steps away. The personnel at AFRL have extensive knowledge and experience with the extrusion of metal matrix composites.

A5.6 Benefits to the Air Force

In the short term, the personnel at AFRL benefited from participating in and staying abreast of the development of a low cost aluminum alloy. In the long term, the U.S. extrusion industry, which the Air Force depends upon for many system components, was strengthened both economically and technically.

A5.7 Results

Two extrusion campaigns were successfully completed. On 11 May 99, a set of five extrusions was conducted. On 22 June 99 another set of seven extrusions was completed. In all cases, the extrusion loads were well within the capacity of the press and there was no excessive die wear. Ram velocity was initially set at relatively low values, but it was finally turned up to a more economical 60 inch/minute. In all cases, the exterior surface finish of the extrusions was quite good. Half of each extrusion was sent to the University of Wisconsin for study and half was retained at AFRL for further examination.

Sections were cut from both the 20 percent and 5 percent extrusion bars. These sections were mounted, prepared metallographically and examined by optical metallography. In order to determine the distribution of flyash particles, optical micrographs (shown in Figure A-5) were taken along the bar radius from the external surface to the center. Preliminary analysis of this data indicated a decreasing density of large flyash particles from the outside surface toward the center of the bar. Further study continued on the distribution of the fine flyash. In addition, a single Rockwell B hardness test was performed at the center of each extrusion, providing both a fiduciary mark indicating the bar's centerpoint and some basic mechanical property information. The hardness values of the 5 percent and 20 percent extrusion bars are 80 R_B and 85 R_B, respectively.

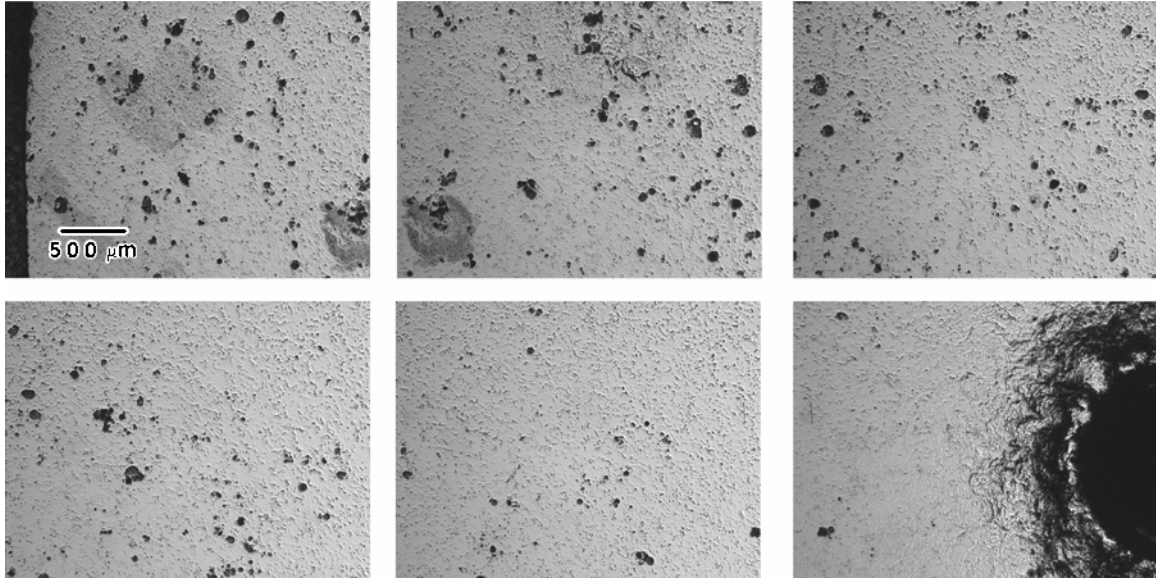


Figure A-5: Series of Optical Micrographs Taken From the 5 Percent Extrusion

Note: Demonstrating the variation in the density of the large flyash particles with position along the radius of the extrusion starting at the outer edge on the upper left and finishing in the center of the extrusion on the lower right.

A6. Casting Simulation Training Seminar

A6.1 Participants and Facilities

Facilities Utilized:

- Computer/Conference Room in Building 655 for classroom
- MPL for instrumentation demos
- MCF for tour
- Nondestructive Evaluation Laboratories for tour

AFRL Participants:

- UES, Inc (Dayton, OH) on-site contractor

Cluster Members:

- CAST-FAB Technologies, Inc (Cincinnati, OH) with 3 students
- SENCO Products, Inc. (Cincinnati, OH) with 3 students
- Parker-Hannifin Corp. (Cincinnati, OH) with 2 students
- EMTEC (Dayton, OH) as facilitator.

A6.2 Objective

Provide training to engineers from the metal casting industry in the use of advanced FEM software. Use the materials processing laboratory at WPAFB to conduct demonstrations of thermocoupling of metal castings, measurement of interface HTC, and computer-aided data acquisition.

A6.3 Background

During the past 20 years, the Air Force has been a leading advocate and funding agency for research in FEM of metal forming and casting processes. In recent years, advanced simulation modeling of metal casting has moved out of the realm of being a research tool and into the world of day-to-day industrial practice. Although it no longer takes a Ph.D. and a main frame computer to run 3-D FEMs, it does require a significant investment in personnel and software for small and medium sized businesses. The first step in this investment is personnel training.

A6.4 Technical Task

UES Software experts conducted an intensive three-day training seminar in FEM of metal casting. The goal of the curriculum was to enable the student to go back to their company and begin running complex 3-D models including advanced features such as fluid flow and moving boundary conditions.

A6.5 Benefits to the Cluster Members

Increasing the number of engineers that are trained in FEM speeded up the acceptance and implementation of simulation modeling in companies that were new to the technology and expanded its use in companies that are already using it. The result was reduced costs, shorter product development cycles and improved quality.

A6.6 Benefits to the Air Force

Increasing the use of simulation modeling in U.S. foundries broadened and strengthened the vendor pool that Air Force prime contractors depend upon for supplying parts. Increasing competition has helped contain initial costs, shortening part development cycle times has reduced weapon system development cycles and increasing part quality has a lasting impact on weapon system life cycle costs.

A6.7 Results

The training seminar was held at WPAFB on 28 to 30 April 1999. Five computer workstations were set up in Building 655 with full installations of the simulation software. The students worked in pairs on each workstation as they followed the instructor's progress on the projection screen (Figure A-6). The seminar room was strategically located near the MPL. During breaks from the classroom instruction, students were given tours of AFRL's processing research capabilities. Demonstrations were set up in the MPL high bay to show the students how to thermocouple castings and use data acquisition systems.



Figure A-6. Training Seminar at AFRL in Casting Simulation Modeling

A7. Solidification Modeling of Aluminum Casting

A7.1 Participants and Facilities

AFRL Participants:

UES, Inc (Dayton, OH) on-site contractor

Cluster Members:

Ross Aluminum Foundries (Sidney, OH)

Cummins Engine (Columbus, IN)

EMTEC (Dayton, OH) as facilitator.

A7.2 Objective

The objectives of this simulation project were as follows:

- Perform a filling and solidification analysis on the Cummins 1514 engine casting
- Generate a characteristic behavior of the filling and solidification pattern.

This was a new project in which ProCAST™ was used to help determine an optimized gating and feeding system.

The purpose of this analysis was to generate a characteristic filling and solidification pattern of the Cummins 1514. This report included both the initial design and modified gating design.

A7.3 Background

Ross Aluminum Foundries, an international supplier of quality castings for the automotive, aerospace, manufacturing and specialty industries, employed UES Software's ProCAST™ division for an investigation into the Cummins 1514 casting.

Ross Aluminum in conjunction with Cummins Engine are in the process of the first time manufacture of a cast component. It is imperative to ensure proper gating design, tool pattern design and process parameters because of critical lead and delivery time.

A7.4 Technical Task

UES Software performed a thermal-only mold heat-up cycle followed by a fully coupled fluid – thermal analysis. Fully coupling the model allowed heat transfer to occur as the model is filling. The simulation employed the ProCAST™ suite of casting simulation software.

A7.4.1 Construction of the Cummins 1514 Casting

The construction of the solid model of the Cummins 1514 was performed using SDRC's I-DEAS Master Series solid modeling tools. This model was transferred to ProCAST™ for the completion of the analysis.

A7.4.2 *Creation of the FEM*

A geometric representation of the model was exported and read into MeshCAST, ProCAST™'s meshing module. A 3-D finite element mesh of the casting and mold was created using MeshCAST's automatic meshing capabilities. Plots of the casting can be found as Figure A-7 and Figure A-8.

A7.4.3 *Process Setup*

The mesh was imported into PreCAST, the pre-processor of the ProCAST™ suite. PreCAST allows for the designation of various process parameters, including the assignment of materials, the simulation of heat transfer between components, the location and rate of the inflow of casting material and many other conditions that affect the casting. For this project, the aluminum alloy A333 was assigned to all of the casting volumes, H-13 die steel to all of the mold components along with a sand core.

The main boundary condition consisted of a heat transfer boundary condition. The heat boundary condition simulated the loss of heat via convection from the metal. Other boundary conditions provided an outer velocity boundary on the pouring cups. The simulation starts with two full pouring cups connected to the runner system. The tilting motion allows the metal to gradually enter the system until the casting is filled when the full rotation is completed.

A7.4.4 *Analysis and Postprocessing*

The analysis of the Cummins 1514 was performed using the ProCAST™ solver. Temperatures and velocities were saved for every ten analysis time steps. Solidification patterns and filling transients were calculated and viewed using ViewCAST and PostCAST, the post-processors for the ProCAST™ suite. Color contour plots of these results were generated and can be found at the end of Section A7.7.5.

A7.5 *Benefits to the Cluster Members*

The use of FEM to optimize commercial process design is now regarded as an essential tool in many foundries. Nonetheless, every company's process is unique and the usefulness of simulation modeling must be demonstrated before the investment in software, hardware and personnel training can be justified. This demonstration stage is more effectively accomplished by using an experienced modeling team, so that the modeling process is more indicative of what the company will be able to accomplish after it's own staff has gone through the learning curve.

A7.6 *Benefits to the Air Force*

In the short term, AFRL personnel benefited by participating in the optimization of a commercial casting design. In the long term, the proliferation of U.S. foundries that use FEM as an integral part of their design process will contribute to reduced cost of Air Force weapon systems.

A7.7 Results

A7.7.1 *Summary of Results*

This task evaluated the Cummins 1514 part and gating design in regard to filling pattern and solidification pattern.

The filling pattern in this tilt pour permanent mold casting is not of a turbulent nature as to cause any defects due to the filling. An initial concern was that of an even distribution of the metal from both pouring cups. In the initial design, there was a heavy dependency on one of the pouring cups as the metal rose into the center section of the casting. The connection at the end of the sprue was increased on the slower filling end, correcting this uneven filling issue.

It is also noted that according to the simulation, the tilt speed may be too fast for the metal to empty the pouring cup. However, this is dependent on the geometry surrounding the cup and is left to the discretion of Ross Aluminum.

The solidification pattern shows a definite trend of starting in the middle of the casting and continuing toward the outer regions. The initial solidification in the center of the casting is due to the thin cross section of the part in that region and to the distance traveled by the metal to reach those locations. This pattern is evident in both the initial and modified designs.

There are several locations, however, of possible shrink porosity due to trapped regions of liquid metal. These locations primarily are bosses on the part. However, two webs appeared to remain hot as the surrounding casting cools. The first of these webs is located just above the large hole in the center bottom of the casting. The other runs from the top of the casting down to a heavy section towards the center of the casting. These possible porosity instances are the same in both the initial and modified designs.

Finally, it appeared that the casting may not have been fully solidified when the mold was tilted back to initial position. This could have easily disturbed the metal as it finishes its solidification in the heavy regions on the edge of the casting.

A7.7.2 *Implications of Results*

The analysis of the Cummins 1514 has determined the following:

- The filling analysis of the initial design showed uneven distribution of the metal from the pouring cups.
- The tilt speed may be slightly faster than the rate the cavity is able to accept the metal.
- The solidification pattern from the center of the casting towards the gating.
- Probable areas of porosity exist in multiple regions of the casting resulting from the isolation of liquid metal during solidification.
- There is a possibility of the mold orientation resetting before total casting solidification.

Please note that these results were based on generalized heat transfer coefficients that are not calibrated for the casting process at Ross Aluminum Foundries. Therefore, there was some degree of error for all results in this analysis.

A7.7.3 *Fluid Solution*

The filling of the Cummins 1514 was driven by the tilting action of the molds. This motion had been captured in ProCAST™ and showed a smooth, even filling of the metal into the mold cavity with no indications of any defects as a result of the filling (Figure A-9 to Figure A-11). The rate of delivery of metal from the pouring cups, however, was a concern as in the initial design, metal was entering from the left pouring cup at a faster rate than the right pouring cup (Figure A-9). Therefore, additional connection area was added between the right runner and right sprue to allow more metal flow. This modification resulted in a filling that allowed the right cup to empty metal faster initially, but then moderated with the left cup as the casting fills (Figure A-17 to Figure A-19). It was also noted that the tilt rate may be faster than the cavity can accept, as a small amount of metal remained in the cup after the mold had fully rotated.

A7.7.4 *Thermal Solution*

The general pattern of solidification for both designs shows a fast solidification from the thin center of the casting towards the thicker and well-fed outer sections of the casting. To find locations of trapped liquid metal, x-ray plots are created which isolate the liquid regions by hiding solid casting regions. These images can be found as Figure A-13 to Figure A-16 for the initial design and as Figure A-22 to Figure A-25 for the modified design. As indicated by these plots, many of these locations are bosses on the casting. However, two rib sections also showed a possibility of shrink porosity. The first rib section was located above the large hole in the lower center portion of the casting (Figure A-13. or Figure A-21.). The other rib section was in the upper right section of the casting to the left of the riser (Figure A-15 or Figure A-24). Both sections appear that they may not be fed enough to prevent the shrink defect.

Also relating to the thermal solution of the Cummins 1514, the analysis shows that the large circular bosses on either side of the casting may not be completely solidified when the mold returns to its initial position. This could cause defects due to sloshing of the metal.

A7.7.5 *Conclusions*

Based on the complete analysis of the Cummins 1514 casting, we developed the following conclusions:

The filling pattern in this tilt pour permanent mold casting is not of a turbulent nature as to cause any defects due to the filling. An initial concern was that of an even distribution of the metal from both pouring cups. In the initial design, there was a heavy dependency on one of the pouring cups as the metal rose into the center section of the casting. The connection at the end of the sprue was increased on the slower filling end, correcting this uneven filling issue.

It is also noted that according to the simulation, the tilt speed may be too fast for the metal to empty the pouring cup. However, this is dependent on the geometry surrounding the cup and is left to the discretion of Ross Aluminum.

The solidification pattern shows a definite trend of starting in the middle of the casting and continuing toward the outer regions. The initial solidification in the center of the casting is due to the thin cross section of the part in that region and to the distance traveled by the metal to reach those locations. This pattern is evident in both the initial and modified designs.

There are several locations, however, of possible shrink porosity due to trapped regions of liquid metal. These locations primarily are bosses on the part. However, two webs appear to remain hot as the surrounding casting cools. The first of these webs are located just above the large hole in the center bottom of the casting. The other runs from the top of the casting down to a heavy section towards the center of the casting. These possible porosity instances are the same in both the initial and modified designs. All possible shrink porosity locations are easily viewed in Section 7.7.6.

Finally, it appears that the casting may not be fully solidified when the mold is tilted back to initial position. This could easily disturb the metal as it finishes its solidification in the heavy regions on the edge of the casting.

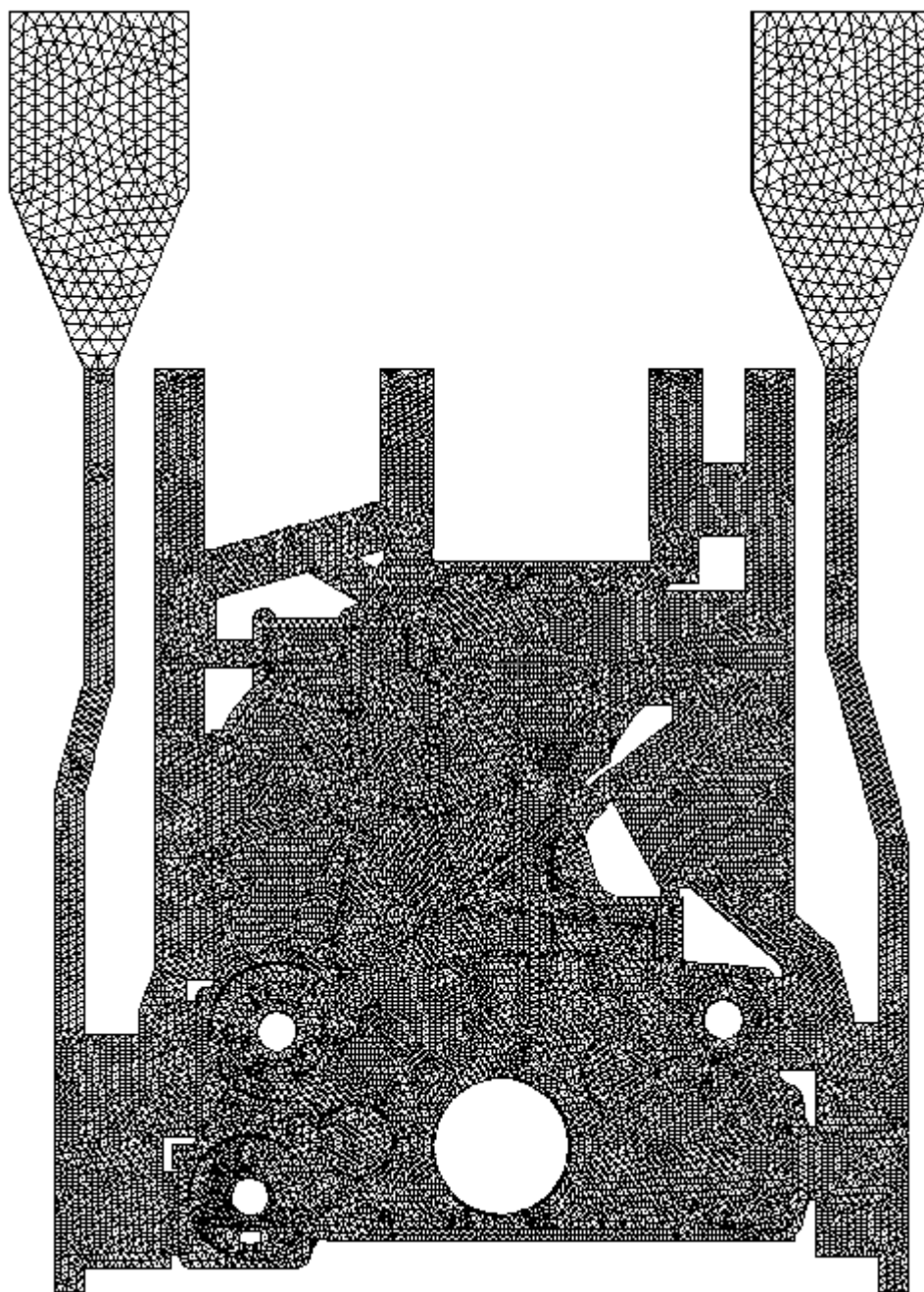


Figure A-7. Initial Casting Design

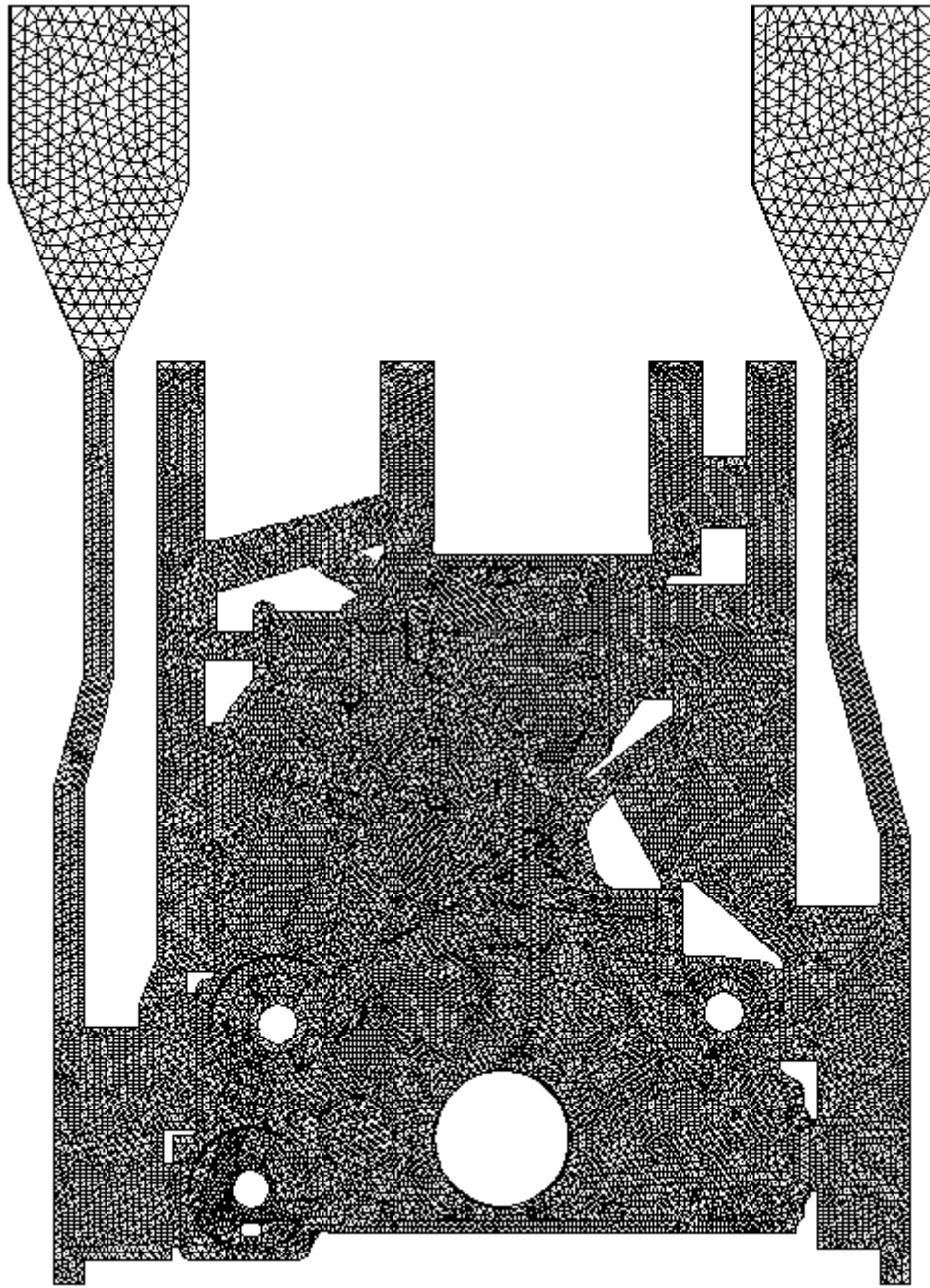


Figure A-8. Modified Casting Design

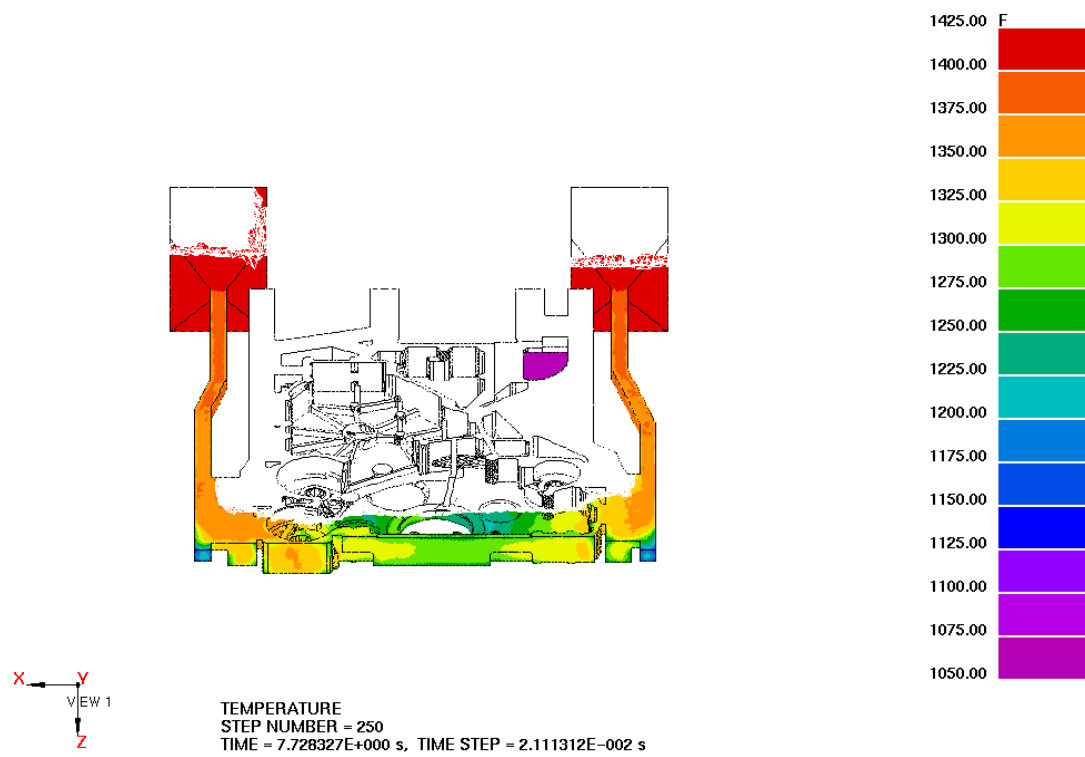


Figure A-9. Temperature Plot Showing Free Surface Front at 7.7 Seconds

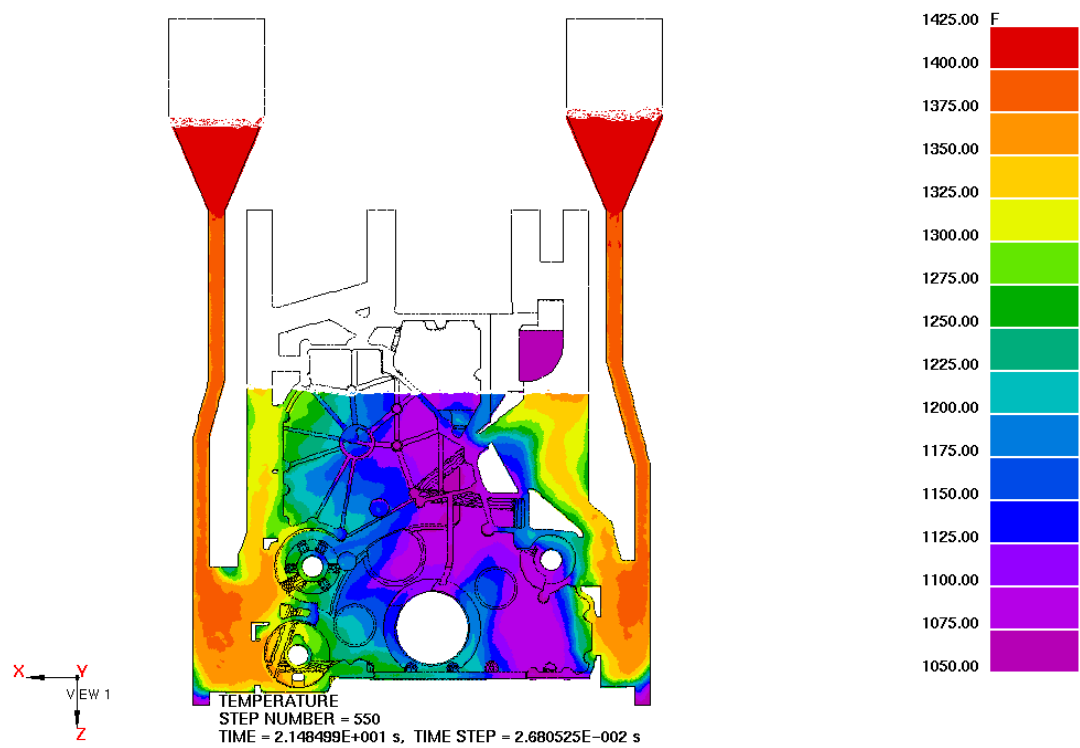


Figure A-10. Temperature Plot Showing Free Surface Front at 21.4 Seconds

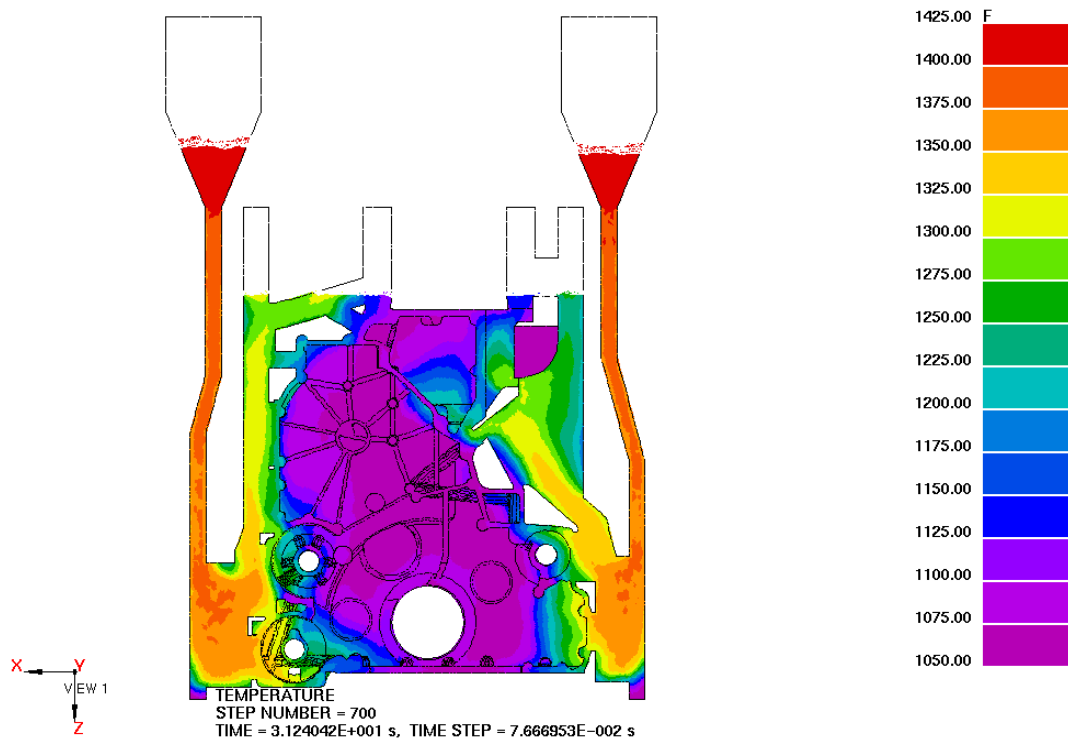


Figure A-11. Temperature Plot Showing Free Surface Front at 31.2 Seconds

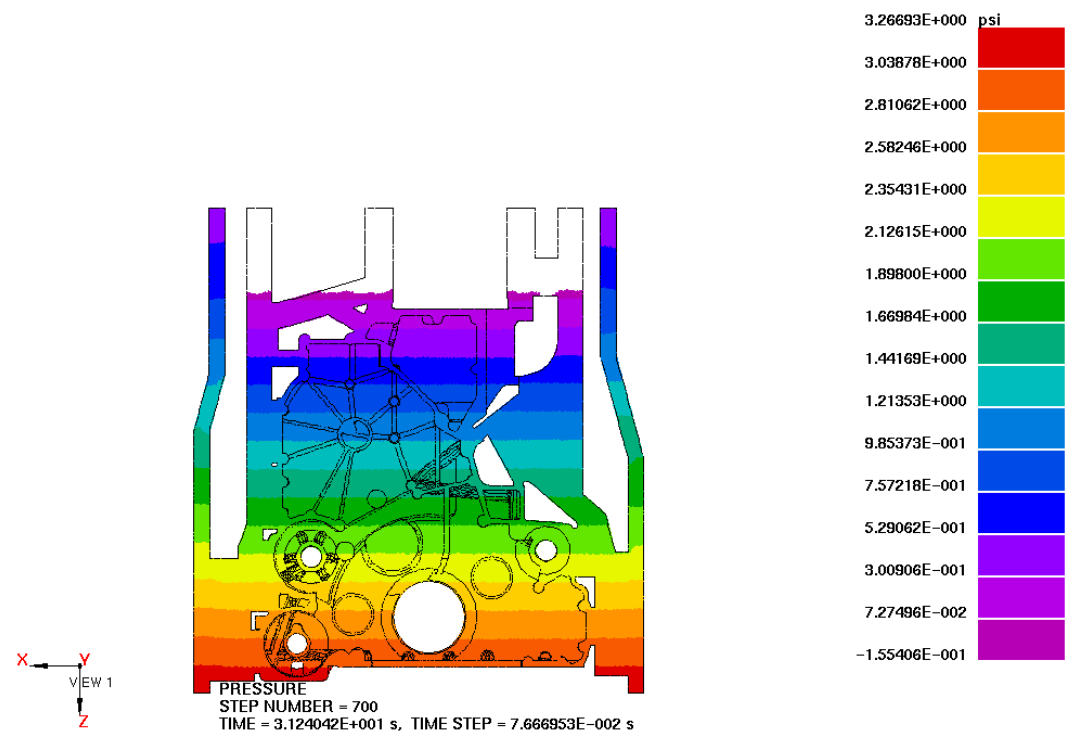


Figure A-12. Pressure Plot Showing Free Surface Front at 31.2 Seconds

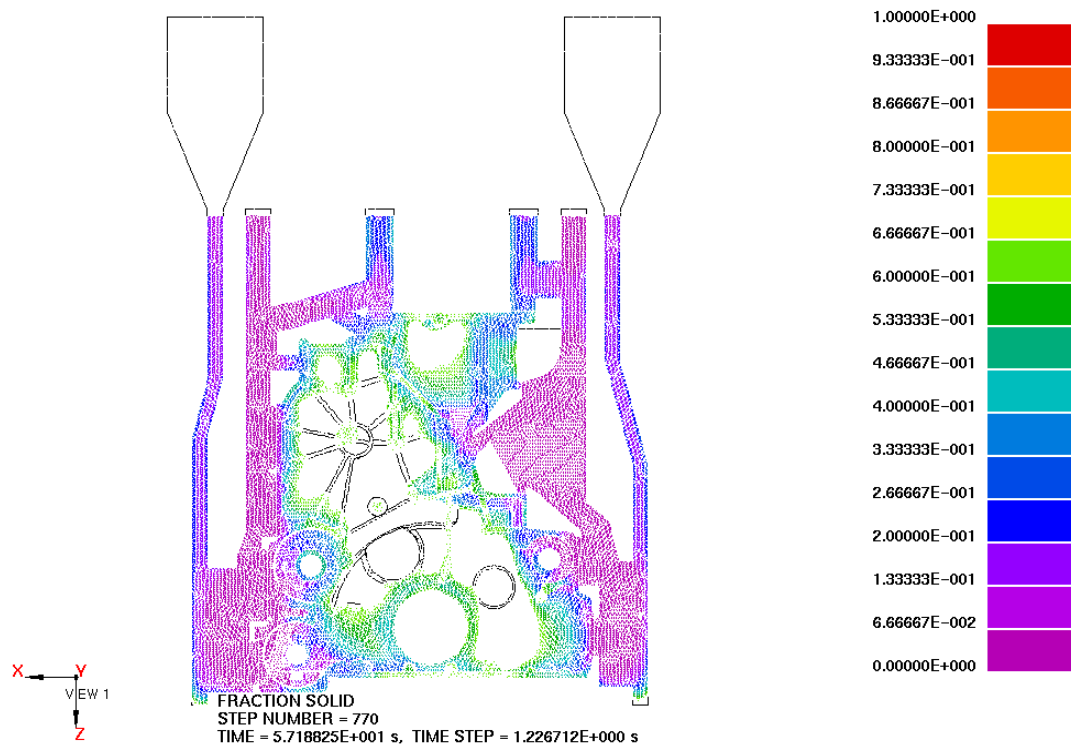


Figure A-13. Fraction Solid Plot with Cutoff = 65 Percent at 57.1 Seconds

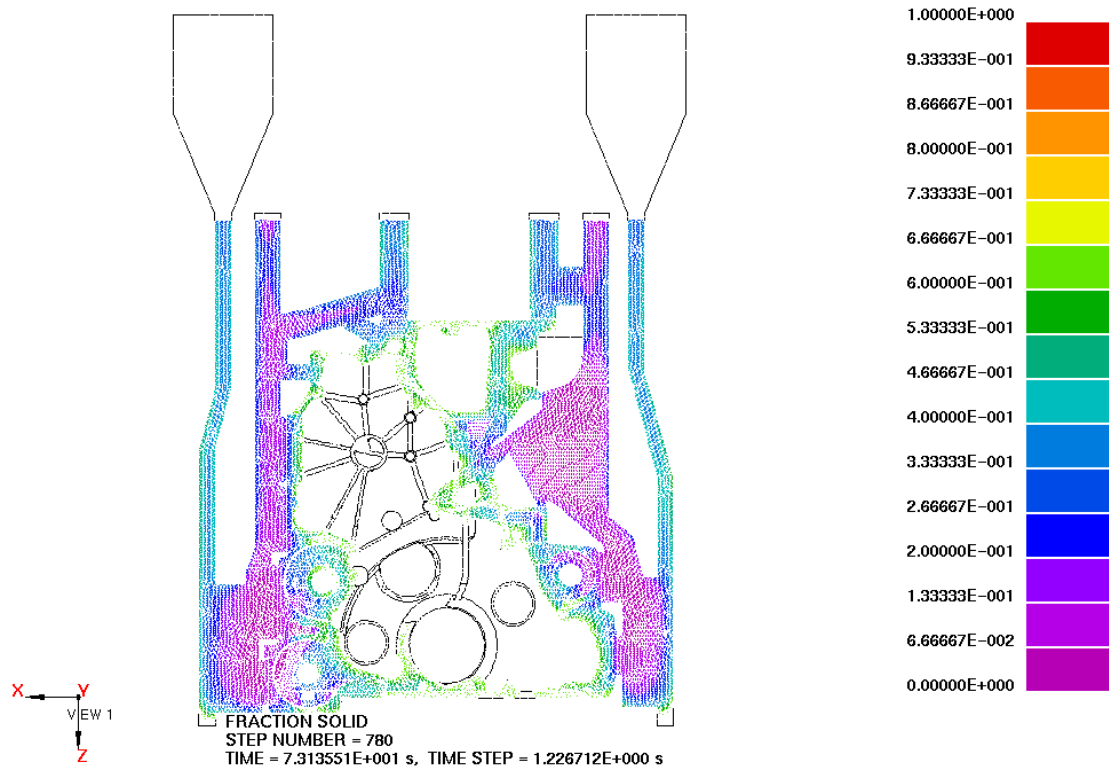


Figure A-14. Fraction Solid Plot with Cutoff = 65 Percent at 73.1 Seconds

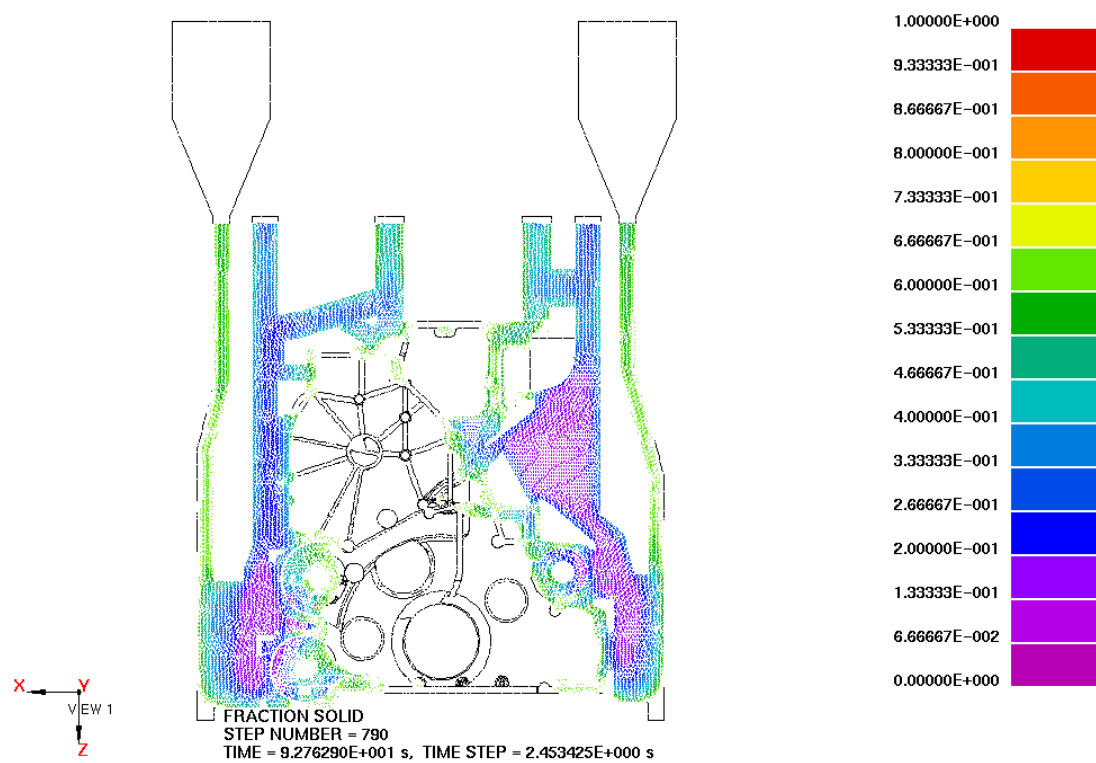


Figure A-15. Fraction Solid Plot with Cutoff = 65 Percent at 92.7 Seconds

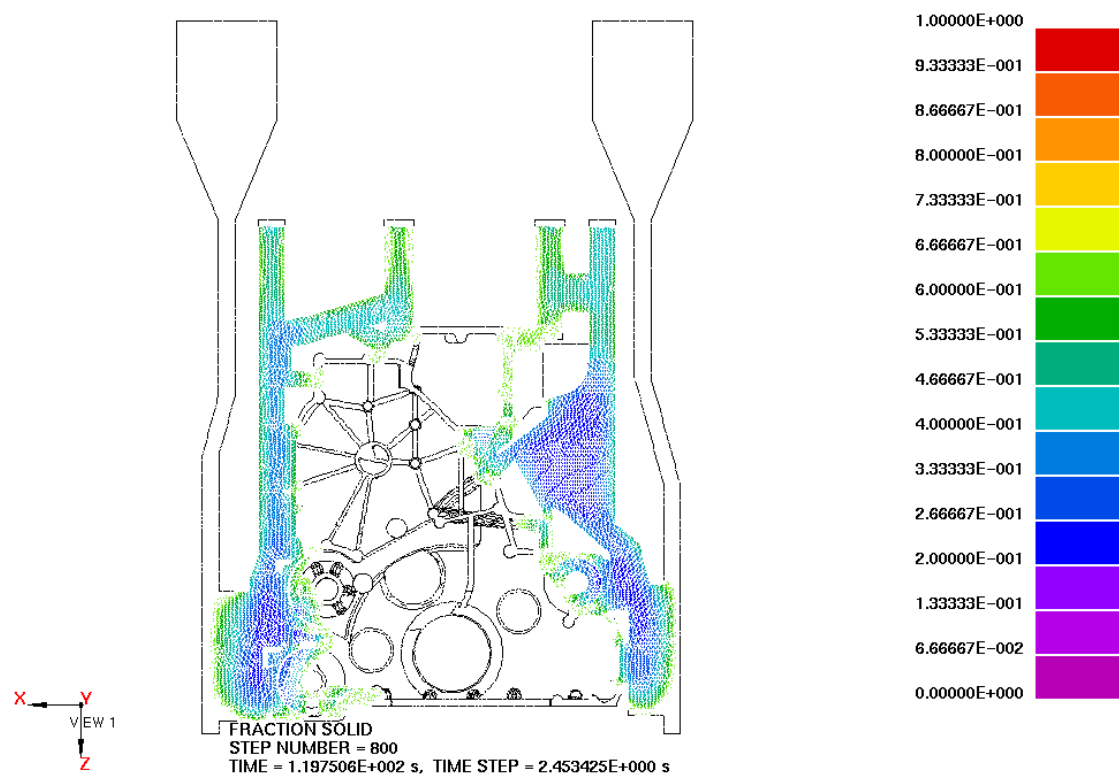


Figure A-16. Fraction Solid Plot with Cutoff = 65 Percent at 119.7 Seconds

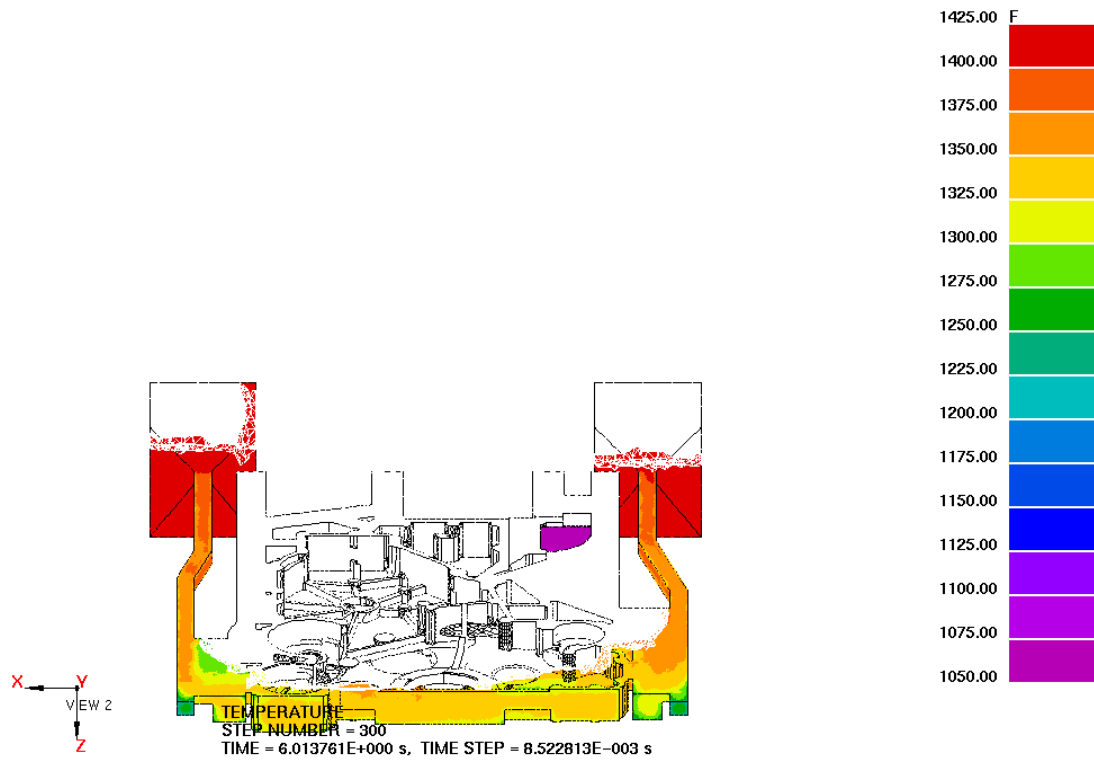


Figure A-17. Temperature Plot Showing Free Surface Front at 6.0 Seconds

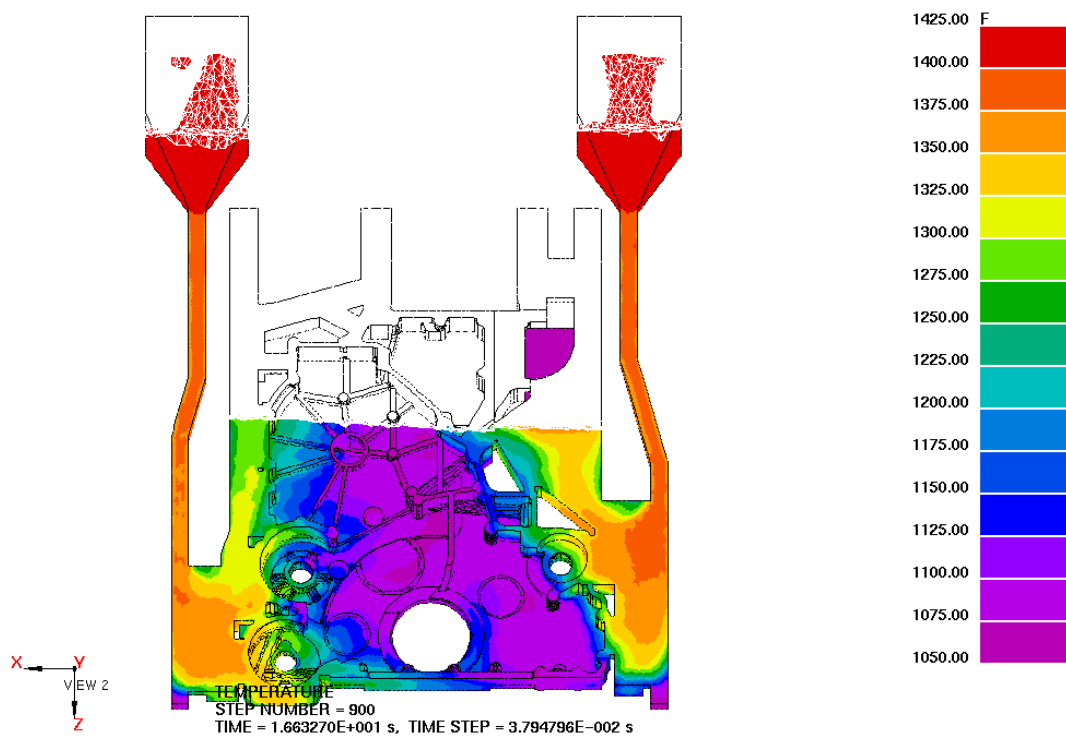


Figure A-18. Temperature Plot Showing Free Surface Front at 16.6 Seconds.

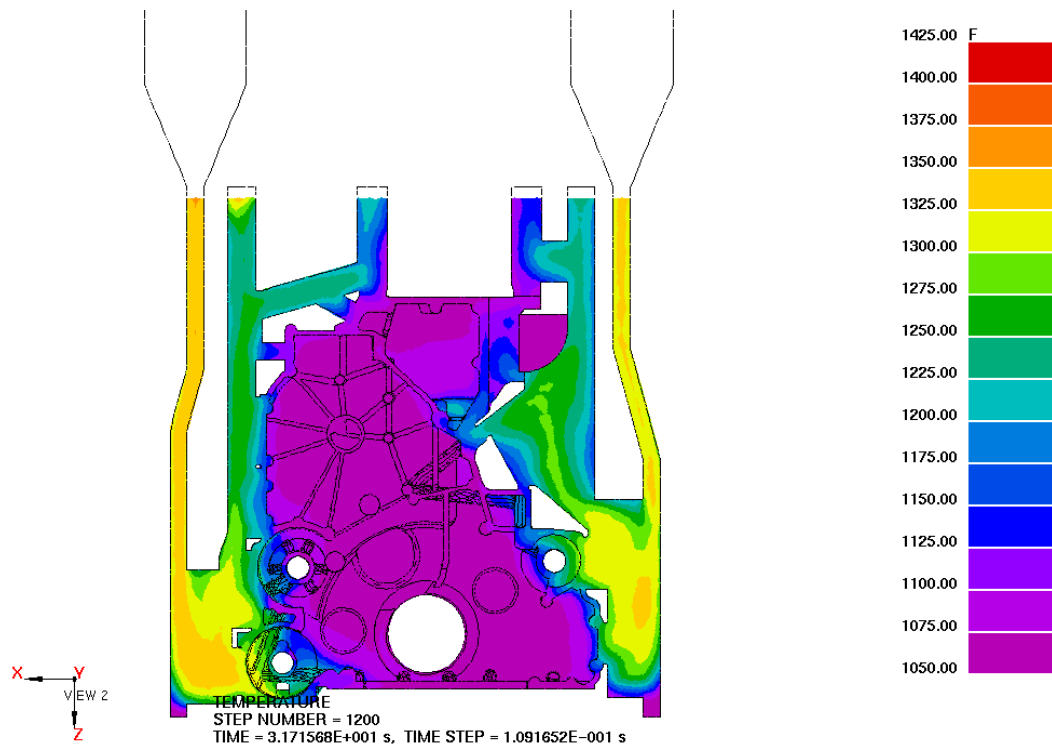


Figure A-19. Temperature Plot Showing Free Surface Front at 31.7 Seconds

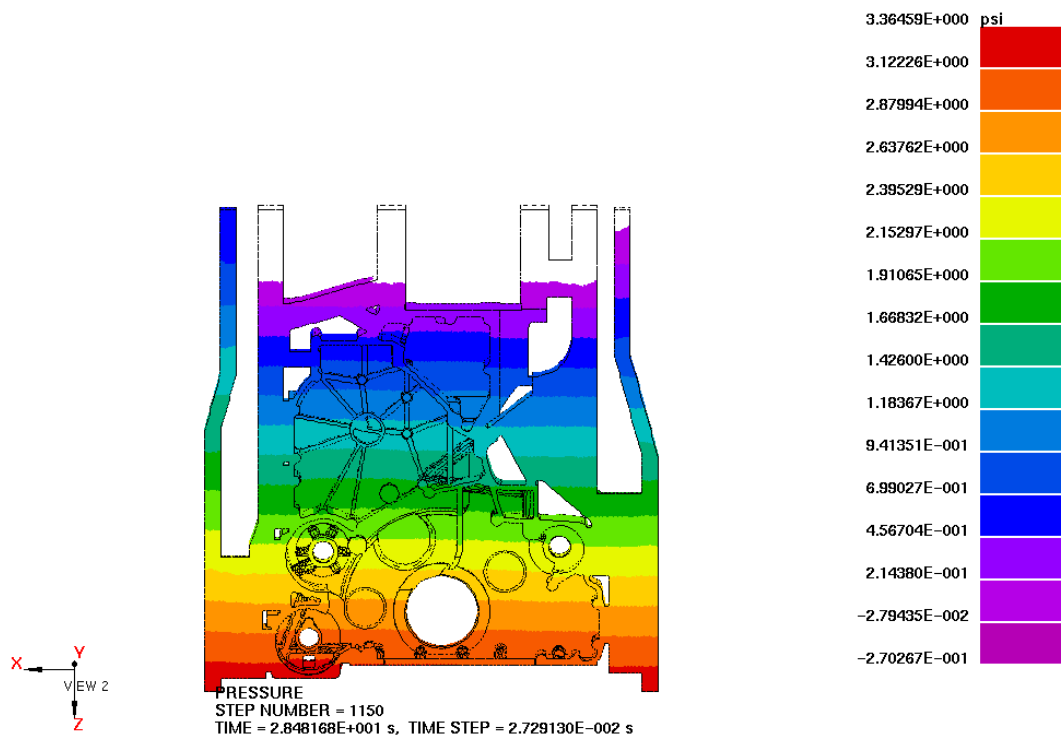


Figure A-20. Pressure Plot Showing Free Surface Front at 28.4 Seconds

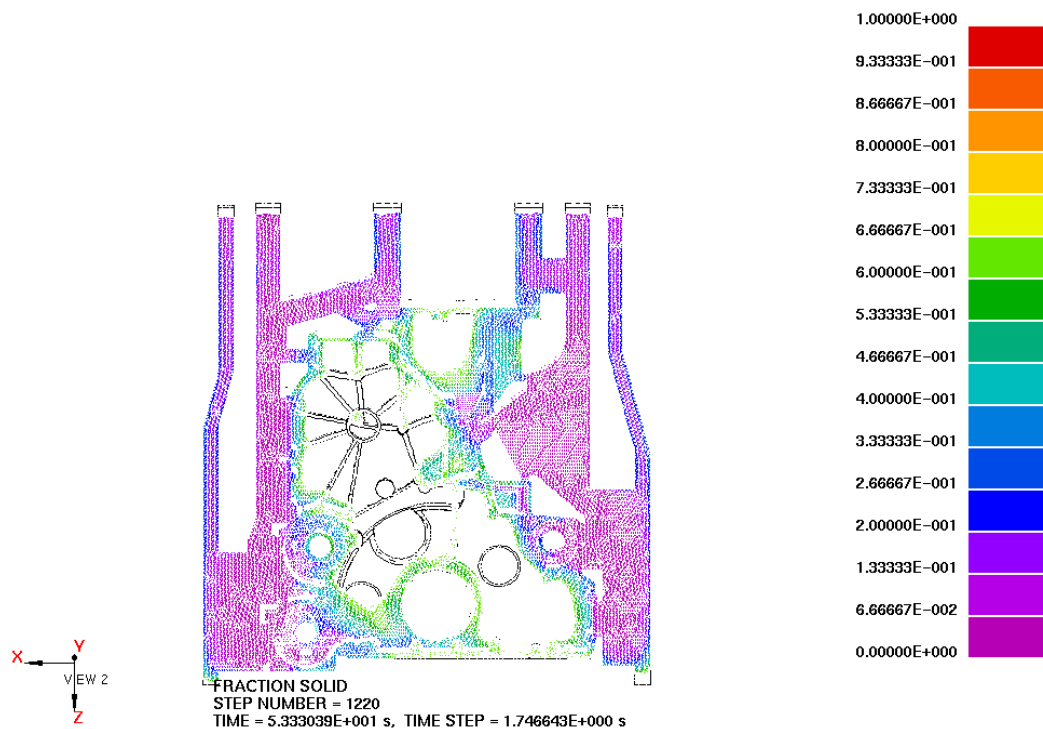


Figure A-21. Fraction Solid Plot with Cutoff = 65 Percent at 53.3 Seconds

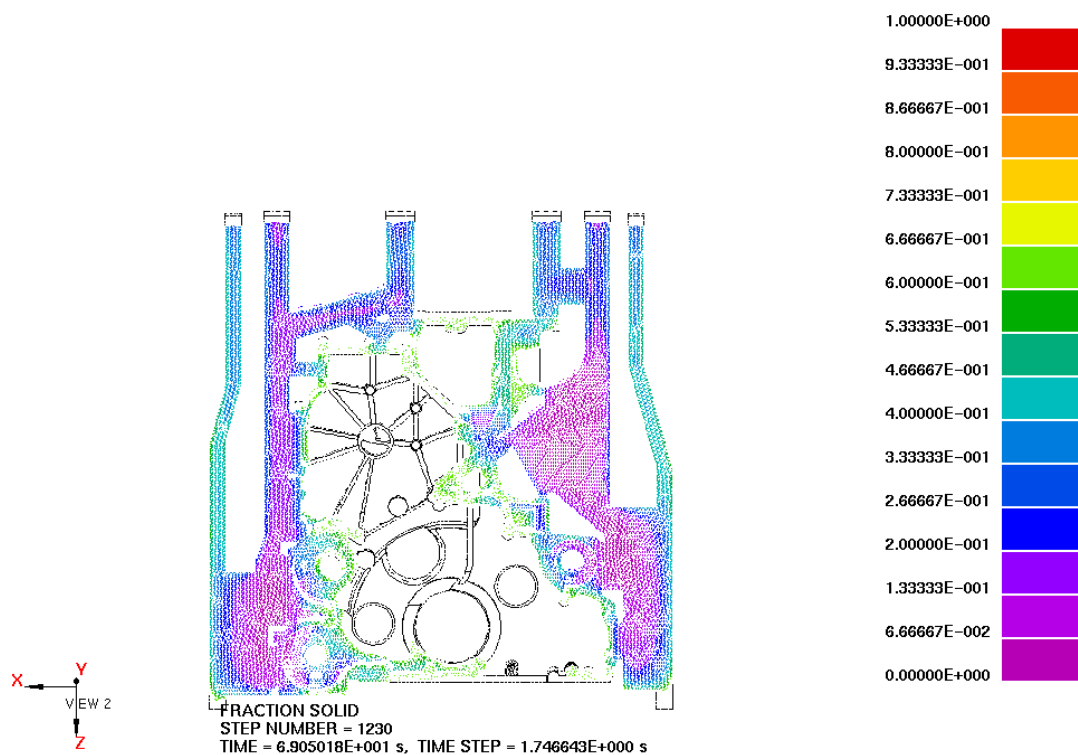


Figure A-22. Fraction Solid Plot with Cutoff = 65 Percent at 69.0 Seconds

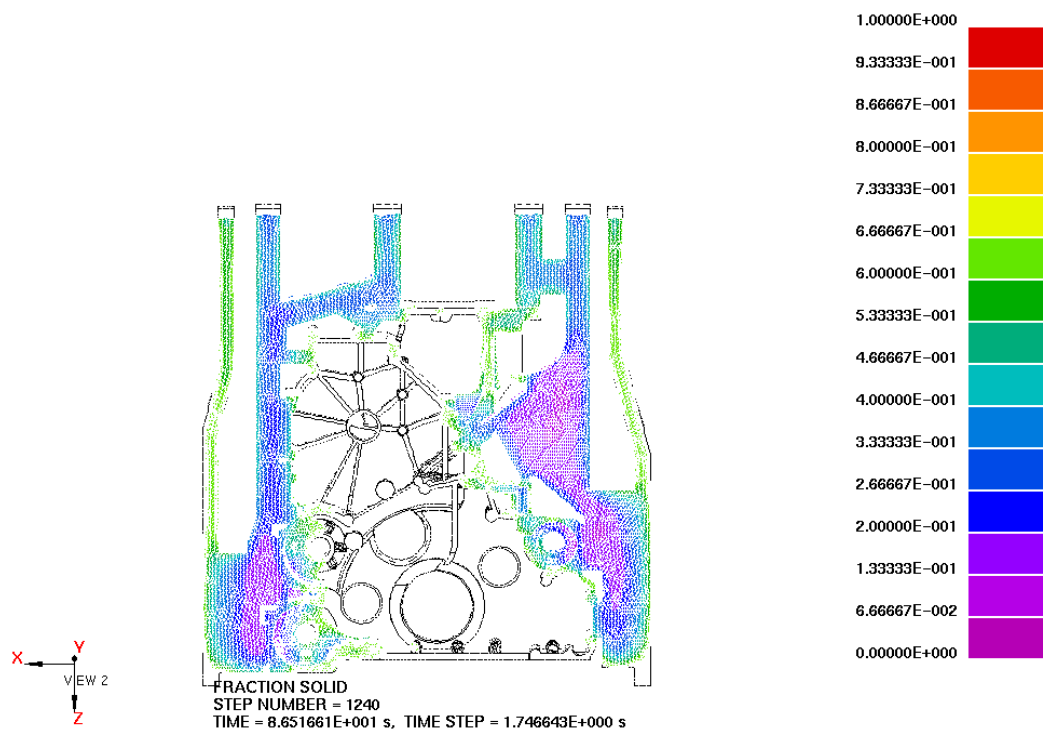


Figure A-23. Fraction Solid Plot with Cutoff = 65 Percent at 86.5 Seconds

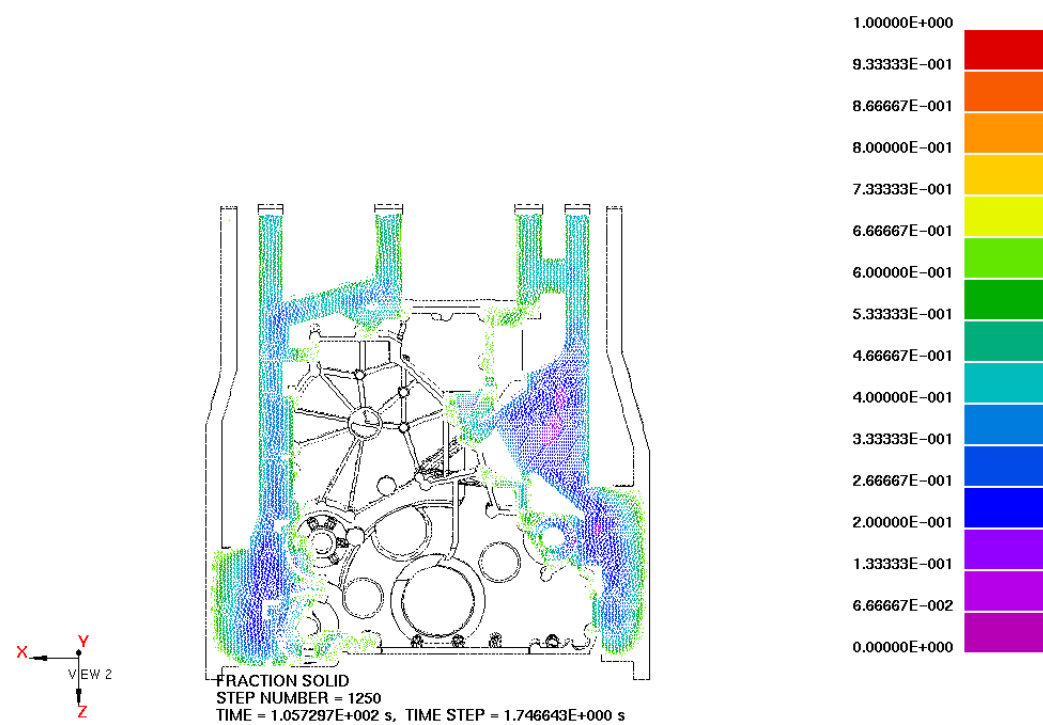


Figure A-24. Fraction Solid Plot with Cutoff = 65 Percent at 105.7 Seconds

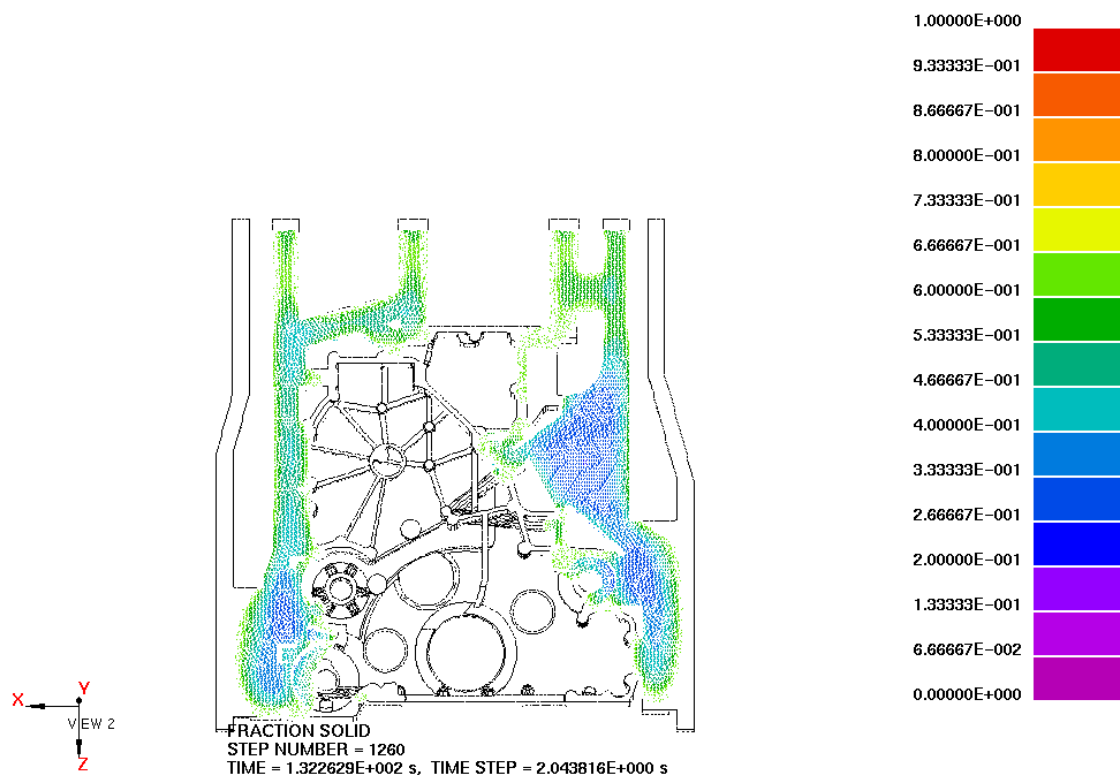


Figure A-25. Fraction Solid Plot with Cutoff = 65 Percent at 132.2 Seconds

A8. Steel Casting Heat Treatment Evaluation

A8.1 Participants and Facilities

Facilities Utilized:

100% MCF: Metallographic analysis
Electron optical analysis

AFRL Participants:

UES, Inc (Dayton, OH) on-site contractor

Cluster Members:

Sawbrook Steel Castings (Cincinnati, OH)
EMTEC (Dayton, OH) as facilitator.

A8.2 Objective

The objective of the microstructural evaluation is to determine if the thermal processing, time(s) at temperature(s), and severity of quench are adequate for the material to assure a uniform microstructure throughout the cross sections examined.

A8.3 Background

Sawbrook Steel Castings in conjunction with one of their customers is in the process of evaluating the homogeneous structure of the quenched and tempered cast steel castings. This evaluation will verify the current processing variables and allow for production of parts without excessively long and costly heat-treatment cycle times.

A8.4 Technical Task

UES provided metallography and microstructural evaluation of the samples submitted. A baseline analysis and subsequent runs allowed us to observe the effects of the thermal processing that the castings receive. The impact that any process changes might have on the integrity of the part was also studied.

A8.5 Benefits to the Cluster Members

The microstructure evaluation provided validation of the heat treatment. This enabled the two companies involved to meet market entry conditions and remain globally competitive. The results may be used in case studies to show how EMTEC is able to affect the competitiveness of Ohio companies and U.S. companies.

A8.6 Benefits to the Air Force

In the short term, the personnel at AFRL benefited from participating in and staying abreast of the development of steel casting heat treatment optimization. In the long term, the U.S. casting industry, which the Air Force depends upon for many system components, will be strengthened both economically and technically.

A8.7 Results

Two steel castings, shown in Figure A-26, were received for microstructural analysis and evaluation relative to each other. The larger of the two castings, the one pictured at the right of Figure A-26, was designated Casting #2, while the smaller casting at the left of Figure A-26 was labeled Casting #1. Both castings were sectioned as shown and the entire sections through the castings were prepared metallographically for microstructural characterization by optical microscopy. Additionally, hardness measurements were made vertically and horizontally across the short and long dimensions of the sections, respectively. These hardness values were then coordinated with the observed microstructures.

Side-by-side comparison via optical microscopy of the two castings from the outer edge (Figure A-27) to the center (Figure A-31) revealed nearly identical microstructures in each casting at equal distances from the outer surface. Examination at lower optical magnifications (100x in Figure A-32 and 6.3x in Figure A-33) disclosed nearly identical dendritic macrostructure, as well. When combined with the nearly identical through sections hardness values displayed in Figure A-34 (Casting #1) and Figure A-35 (Casting #2) the total weight of the evidence confirmed the comparable nature of the two castings relative to each other.



Figure A-26. Sectioned Castings

Note: Casting #1 left and Casting #2 right. Metallographically prepared sections on the right showing the positions of hardness tested done along vertical (short) direction and horizontal (long) direction.

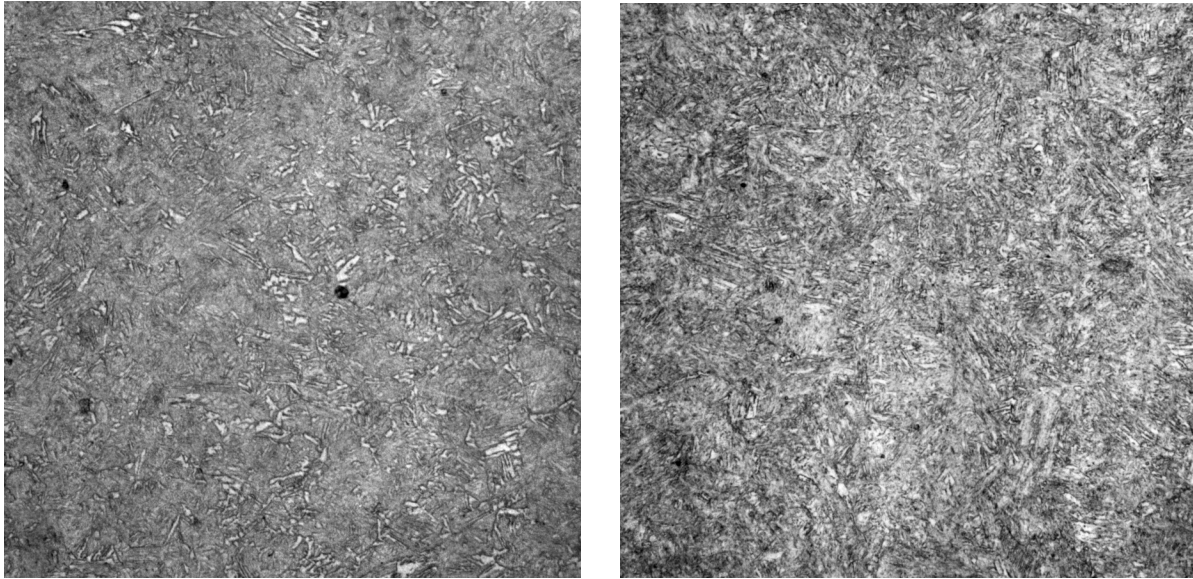


Figure A-27. Microstructure 5 mm from the Bottom Edge of Casting #1 (left) and Casting #2 (right)

Note: 400x, Nital 4%

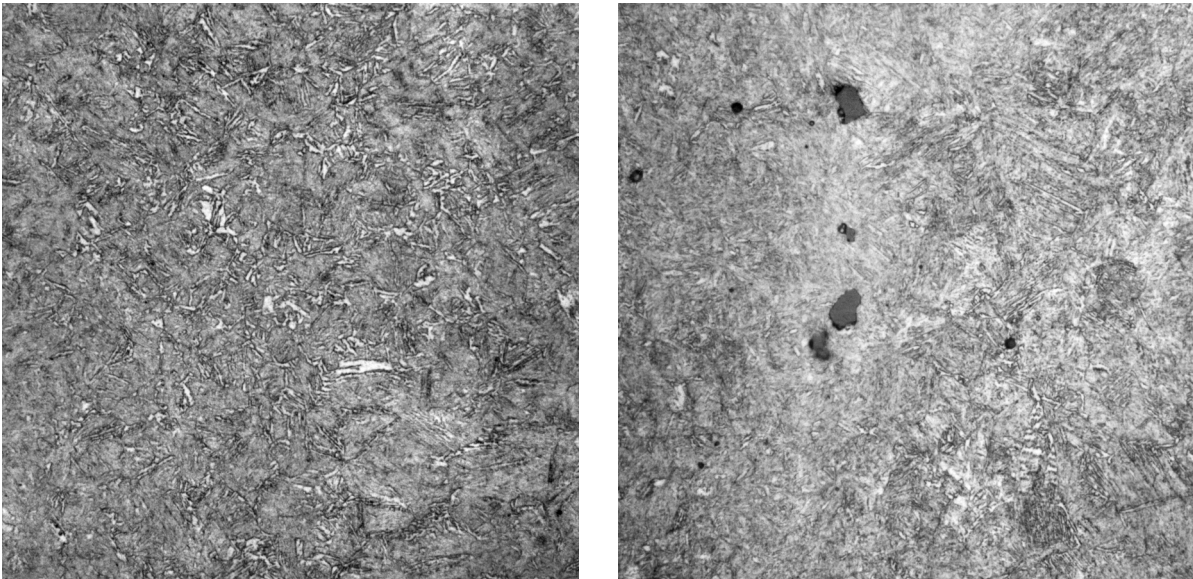


Figure A-28. Microstructure 10 mm from the Bottom Edge of Casting #1 (left) and Casting #2 (right)

Note: 400x, Nital 4%

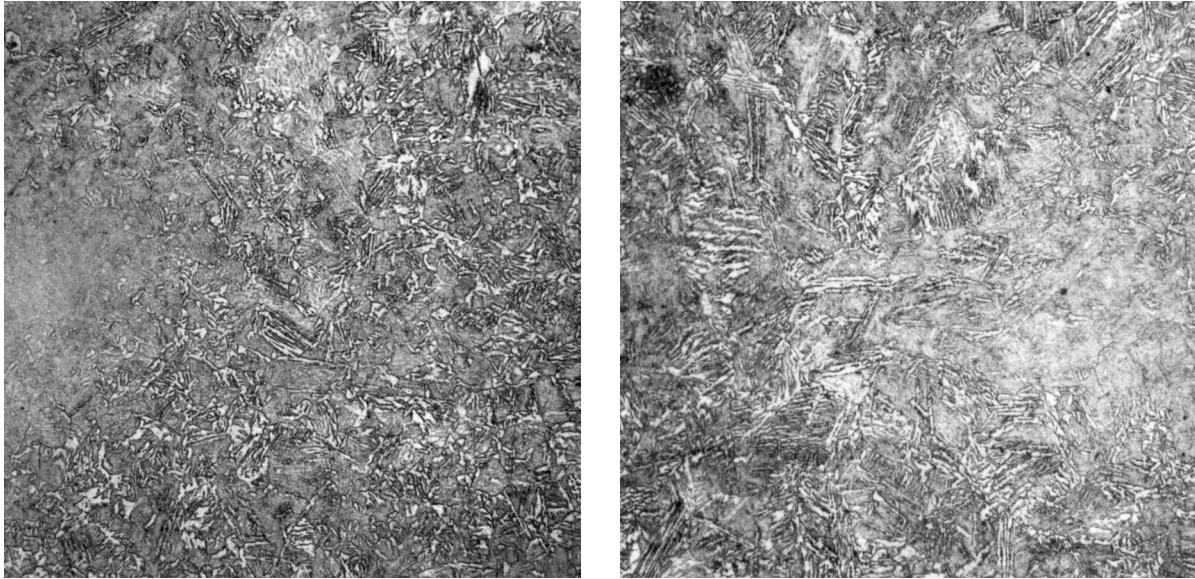


Figure A-29. Microstructure 20 mm from the Bottom Edge of Casting #1 (left) and Casting #2 (right)

Note: 400x, Nital 4%

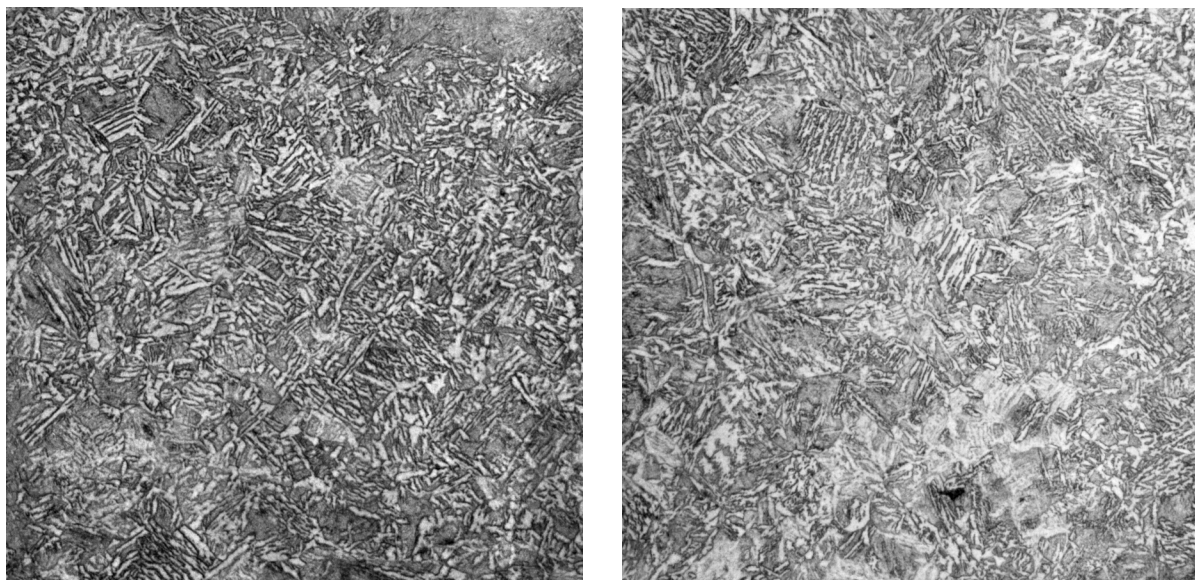


Figure A-30. Microstructure 30 mm from the Bottom Edge of Casting #1 (left) and Casting #2 (right)

Note: 400x, Nital 4%

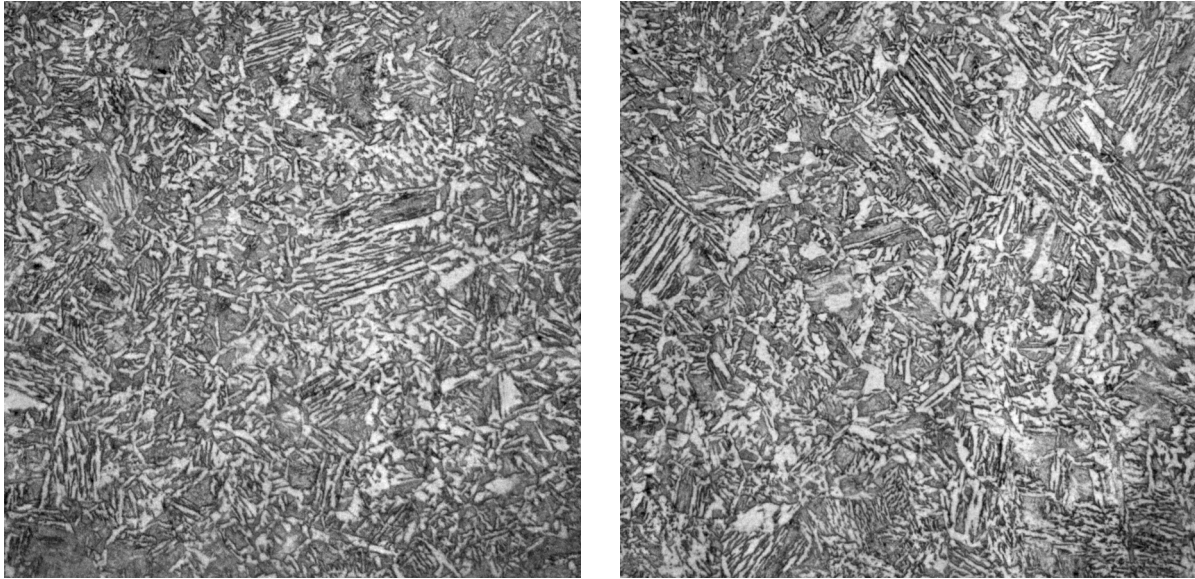


Figure A-31. Microstructure 35 mm from the Bottom Edge (near the center) of Casting #1 (left) and Casting #2 (right)

Note: 400x, Nital 4%

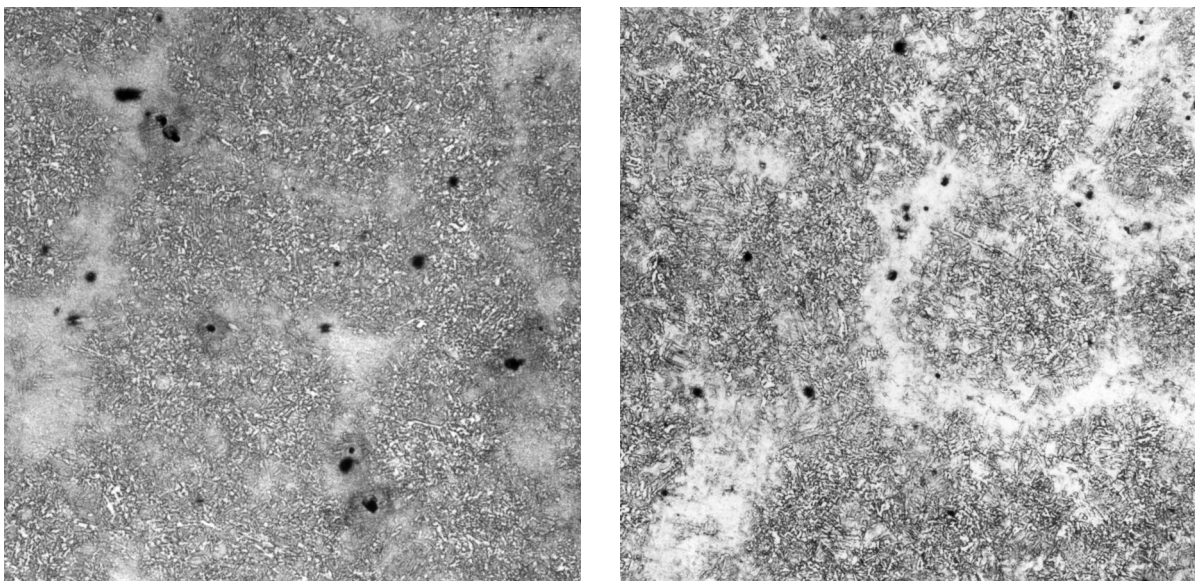


Figure A-32. 35mm (center) Casting #1 on (left), Casting #2 (right) Lower Mag

Note: 100x, Nital 4%

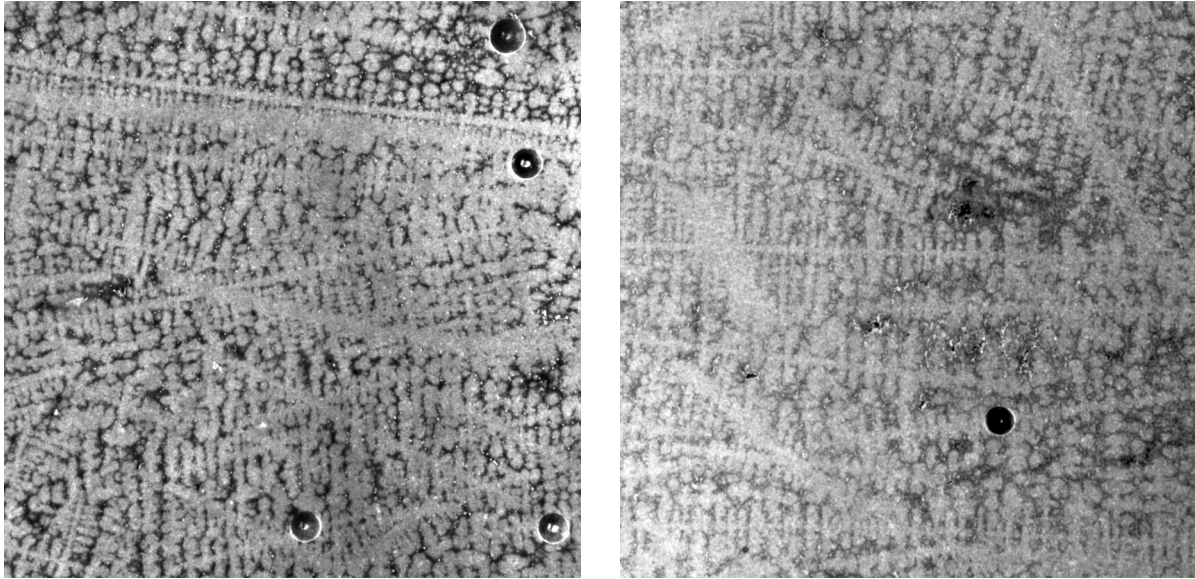


Figure A-33. 35mm (center) Casting #1 (left), Casting #2 (right) macro

Note: 6.3x, Nital 4%

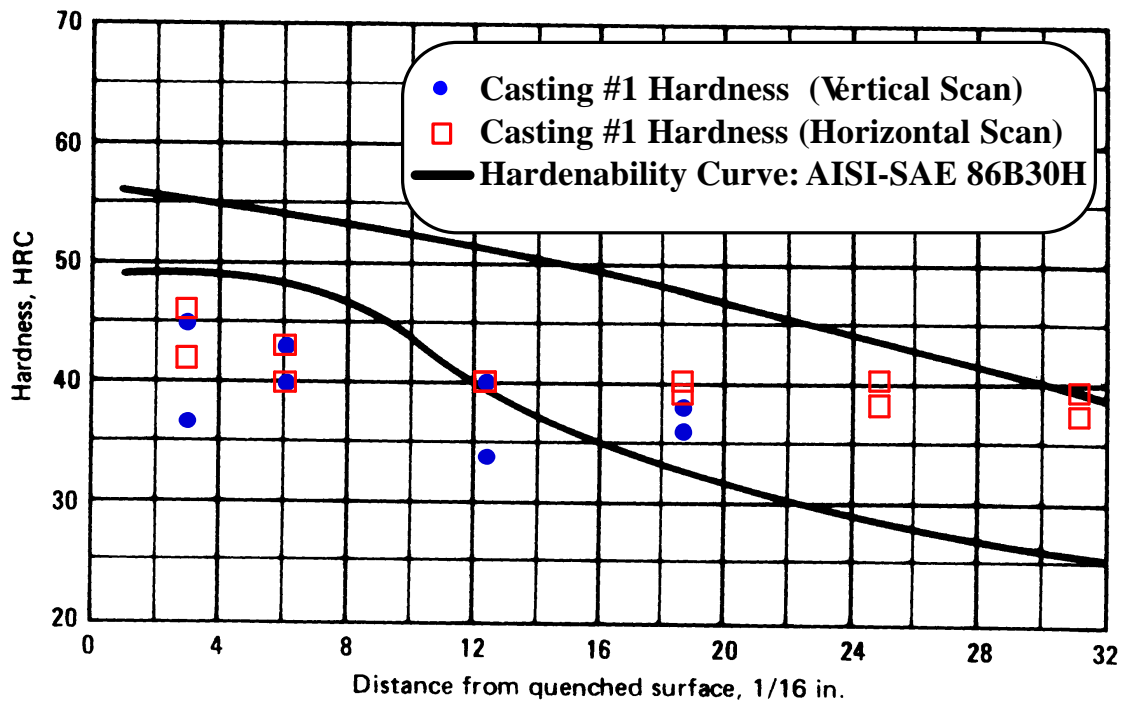
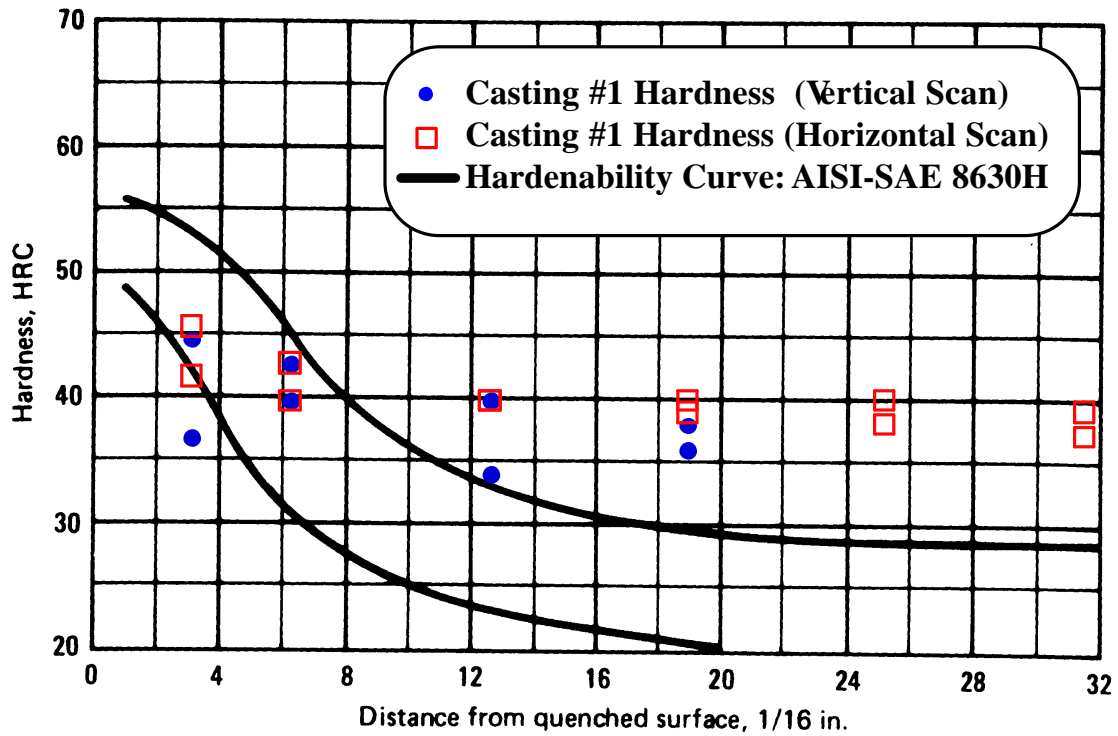


Figure A-34. Hardness Data for Casting #1 Plotted Against the Hardenability Curves for Two Different 8630 Alloys: AISI-SAE 8630H and AISI-SAE 86B30H

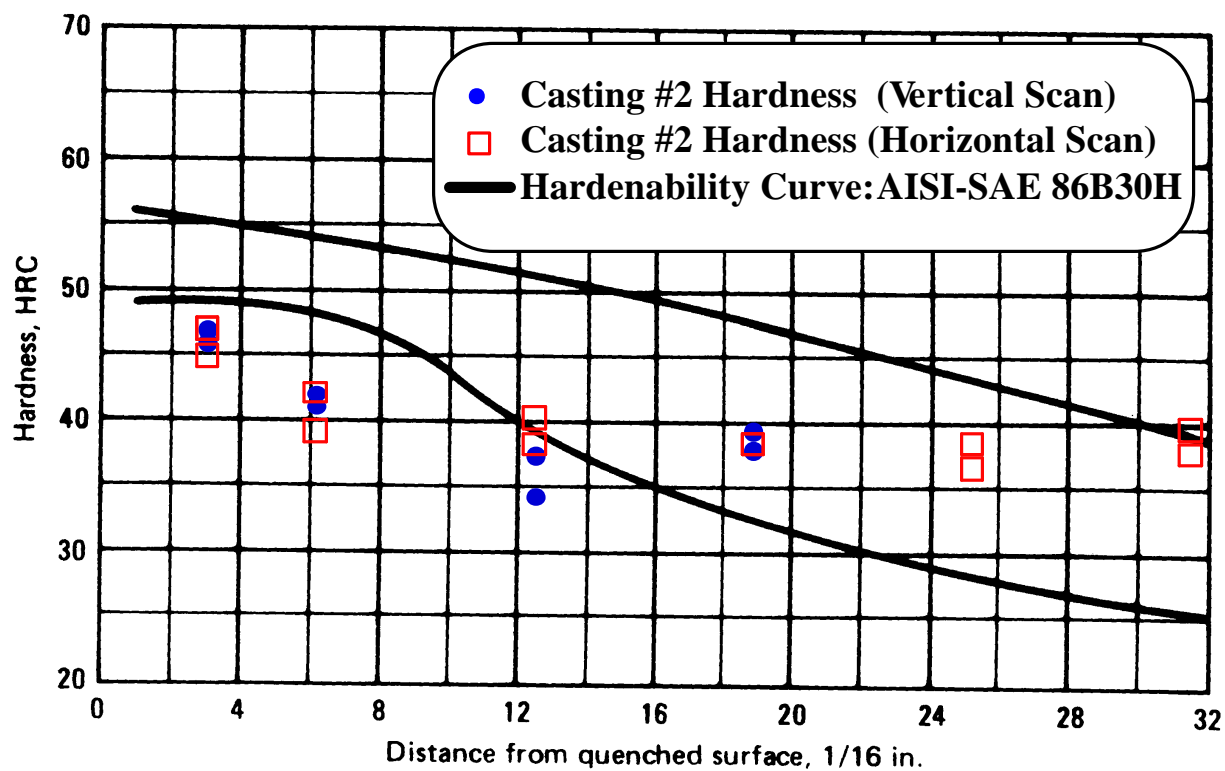
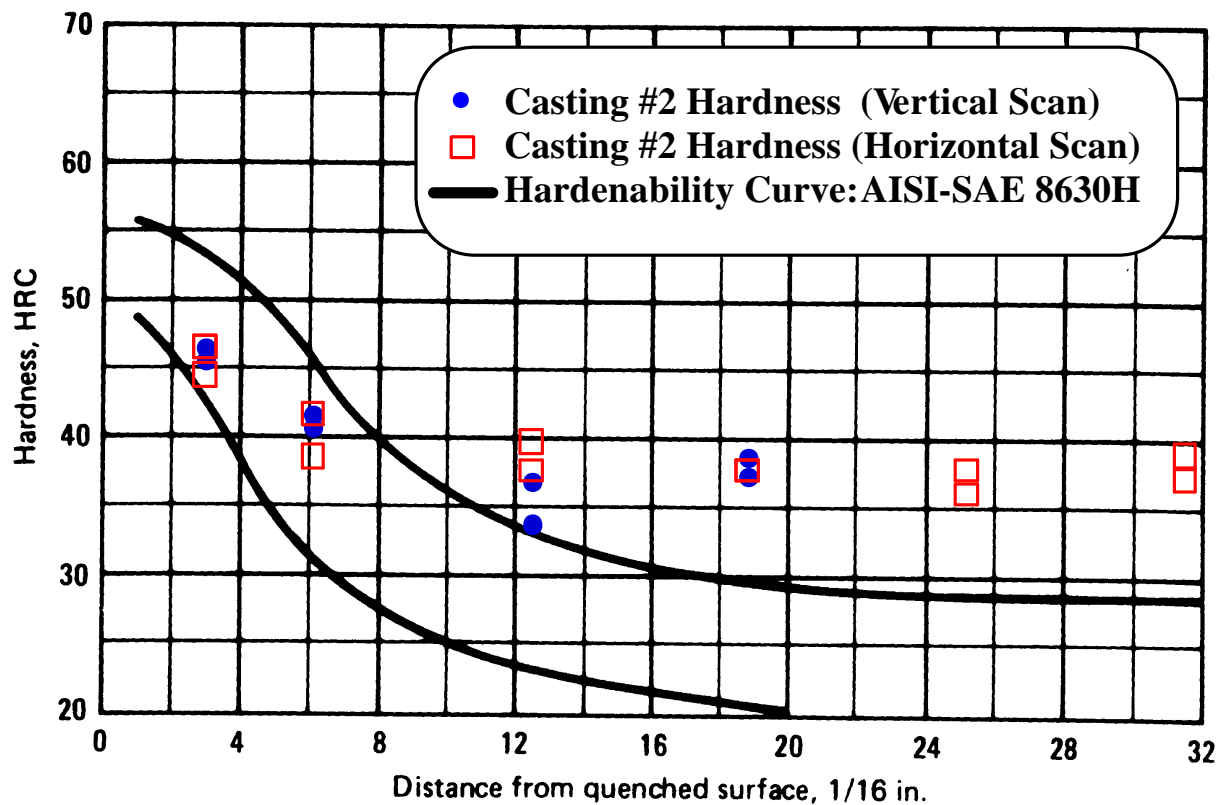


Figure A-35. Hardness Data for Casting #2 Plotted Against the Hardenability Curves for Two Different 8630 alloys: AISI-SAE 8630H and AISI-SAE 86B30H

A9. Aluminum Squeeze Casting Defects

A9.1 Participants and Facilities

Facilities Utilized:

100% MCF: Electron optical analysis

AFRL Participants:

UES, Inc (Dayton, OH) on-site contractor

Cluster Members:

Amcast (Dayton, OH)

A&B Foundry

Funk Finecast

Lester Precision Casting

Lodi Foundry

EMTEC (Dayton, OH) as facilitator.

A9.2 Objective

Optimization of squeeze casting process.

A9.3 Background

Squeeze casting is a process with a slow fill rate, minimum turbulence and high pressure throughout solidification to consistently produce high integrity castings capable of solution heat treatment. The squeeze casting process combines the advantages of traditional high-pressure die casting, gravity permanent mold casting, and forging.

A9.4 Technical Task

The scope of the effort on this program by the MCF was to help with the continued development of the squeeze casting process by providing material characterization, specifically SEM and EDS. This would help better understand the morphology, chemical makeup, and types of inclusions present in high volume castings.

A9.5 Benefits to the Cluster Members

A number of industries are in production with squeeze casting processes in such diverse commercial applications as commercial air conditioning, bicycles, control valves and pump housings. In development are projects, which may capitalize on the uniqueness of the squeeze casting process i.e., disposable coring, selective ceramic reinforcing of structural parts, and metal matrix composites. On the other hand, since squeeze casting is still a relatively new process in the industry, there are some issues, such as excessive centerline segregation, entrapped oxide films in castings, which need to be investigated and solved.

A9.6 Benefits to the Air Force

AFRL personnel benefited by staying abreast of the squeeze casting process developments that would result from this better understanding of the morphology, chemical make-up, and types of inclusions present in high volume castings. This understanding will benefit the Air Force by providing a high integrity casting process, which is capable of delivering superior mechanical properties.

A9.7 Results

A fractured wheel rim produced by the squeeze casting method was analyzed by SEM and EDS in order to characterize the morphology and chemical nature of an inclusion present on the fracture surface. SEM/EDS of a defect in the fracture surface, shown in Figure A-36, indicated oxygen and magnesium enrichment in the defect (A) relative to clean fracture surface (B). Examination of the defect and clean fracture surfaces at higher magnification (Figure A-37) showed the film-like nature of the defect surface as compared to the normal ductile fracture nature of the remainder of the fracture surface. Based on its oxygen content and surface appearance, this squeeze casting defect can be identified as an entrapped oxide film.

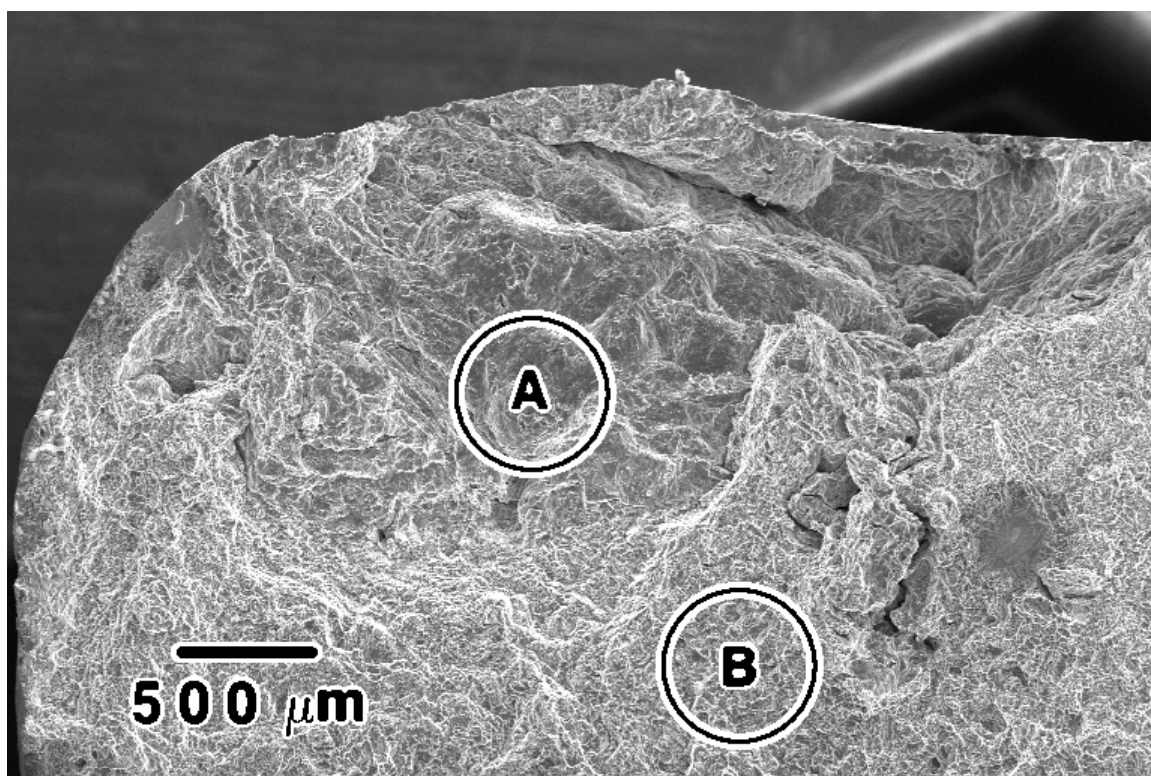


Figure A-36. SEM of Fractured Wheel Rim Produced by the Squeeze Casting Method

Note: EDS data indicate an enrichment of Oxygen and Magnesium in the defect area (A) relative to the clean fracture surface (B).

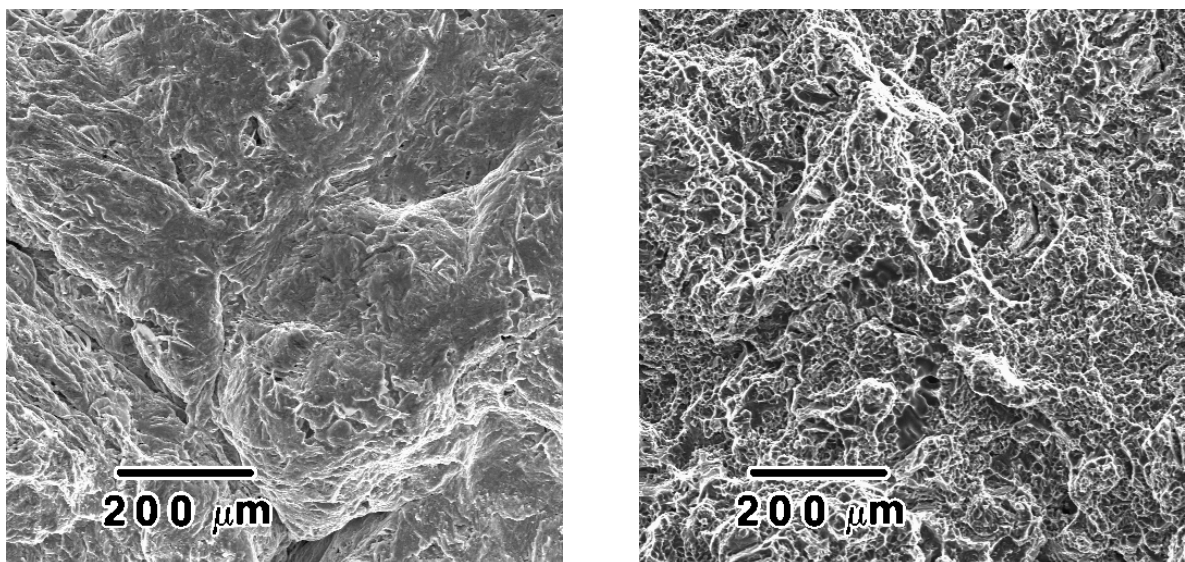


Figure A-37. SEMs of a Defect in the Fracture Surface (left side) and of the Clean Fracture Surface (right side)

A10. Forgeability of Al-flyash Composite Brake Rotor

A10.1 Participants and Facilities

Facilities Utilized:

100% MPL: 1000-ton forge press

AFRL Participants:

UES, Inc (Dayton, OH) on-site contractor

Cluster Members:

Thompson-Aluminum Casting Co. (Cleveland, OH)

ECK Industries, Inc. (Manitowoc, WI)

CHL Microspheres, Inc (Helenwood, TN)

Ohio Edison (Akron, OH)

Dayton Power and Light Corp. (Dayton, OH)

University of Wisconsin (Milwaukee, WI)

Oak Ridge National Laboratory (Oak Ridge, TN)

EMTEC (Dayton, OH) as facilitator.

A10.2 Objective

Determine the feasibility of direct forging of a brake rotor from Al-flyash composite.

A10.3 Background

Earlier flyash work using extrusion (see Section A-5) showed that this is a highly formable composite material. Brake rotors are a product that present a natural opportunity for the rapid insertion of this material due to the inherent advantages of the flyash composite in terms of wear resistance.

A10.4 Technical Task

Ingots of aluminum alloy and of flyash composition were cast by Thompson-Aluminum Castings. UES prepared and forged ingots of 3-inch diameter ingots on the 1000-ton forge press at AFRL. UES selected the process parameters of temperature and ram velocity based upon the earlier, and highly successful, extrusion of ingots of these same compositions.

A10.5 Benefits to the Cluster Members

Conducting evaluation tests at AFRL is a superior method of evaluating the forging behavior of Al-flyash alloys for two reasons. First, it was more cost effective to conduct trials on the AFRL pilot plant scale forge press than to immediately scaleup to commercial size. Second, it was more effective to conduct trials in the laboratory environment at AFRL, where the entire forging process can be closely monitored and expert personnel from multiple fields are only a few steps away.

A10.6 Benefits to the Air Force

In the short term, the personnel at AFRL benefited from participating in and staying abreast of the development of a low cost aluminum alloy. In the long term, the U.S. extrusion industry, which the Air Force depends upon for many system components, will be strengthened both economically and technically.

A10.7 Results

Ingots of 6061Al and of 6061Al + 15wt% 250- μ m flyash composite were upset forged from an initial diameter of 3 inches to a final diameter of 6 inches. This rather large degree of deformation ($\epsilon = 1.38$) was chosen in order to push the limit on defining just how formable the composite material was. The forged products are shown in Figure A-38. The straight aluminum alloy was forged as a control specimen. As expected, it showed uniform deformation with no outward appearance of cracking. The flyash billet, by contrast, showed considerable cracking on the outer diameter. This cracking is caused by the tensile stresses developed in this region during upset forging.

The conclusion drawn from these experiments is that the flyash ingots that were available at the time did not have sufficient formability to undertake any development effort for brake rotors. The ingot casting process that produced these ingots had not yet been optimized and had not yet been converted to a true pilot plant production process. Since that time, ingots of higher quality have been produced, and may be studied for forging formability in a future program.



Figure A-38. Upset Forgings of 6061Al and of 6061Al + 15wt% 250- μ m Flyash Composite

A11. Stainless Steel Casting Inclusions

A11.1 Participants and Facilities

AFRL Facilities Utilized:

100% MCF: Metallographic analysis
Electron optical analysis

AFRL Participants:

UES, Inc (Dayton, OH) on-site contractor

Cluster Members:

Kovatch Castings (Irontown, OH)
Lucas Industries (Jamestown, ND)
Remelt Corp. (Cleveland, OH)
Ransom & Randolph (Maumee, OH)
EMTEC (Dayton, OH) as facilitator.

A11.2 Objective

To determine the composition of inclusions in stainless steel investment castings. Once the composition is known, preventative measures can be directed to the origin of said material, whether it is due to the casting process or materials used.

A11.3 Background

Kovatch Castings is currently supplying Lucas with a specific stainless steel casting. There is a random occurrence of inclusions in the castings. Limited investigative work has been done to determine the source of the inclusion. Areas of concern are metal quality, shell materials, wax pattern removal, and casting techniques. Kovatch Castings and their suppliers are interested in determining the inclusion chemistry.

A11.4 Technical Task

Identify the composition of the inclusion found in production castings.

A11.5 Benefits to the Cluster Members

Once identified, Kovatch and their suppliers determined the cause of the problem. Kovatch saw increased yield from their casting process. Decreased scrap is increased profit. The suppliers concern for their respective products allowed them to investigate their materials and its interaction in the casting process. Understanding and correcting the problems with their product guaranteed a better product for their customers.

A11.6 Benefits to the Air Force

AFRL personnel benefited by staying abreast of the investment casting process for stainless steel developments that would result from this better understanding of the interaction of all the parameters that make up the investment casting process for stainless steel. Any future castings

produced or purchased by the Air Force that may exhibit inclusions can be analyzed using what was learned through this research.

A11.7 Results

The stainless steel investment casting shown in Figure A-39 was inspected for the presence of inclusions. The composition of the casting was analyzed by EDS and, as expected for a stainless steel, it was found to be composed principally of iron, chromium and nickel, with small additions of aluminum and silicon. The EDS compositional spectrum of this material is displayed in Figure A-40.

An inclusion visible on the surface of the casting was examined by SEM using secondary electron imaging (SEI) and backscattered electron imaging (BEI). Results of examining the surface of the as received casting are shown in Figure A-41 and Figure A-42. The low level of electron intensity of the BEI micrograph in Figure A-42 indicates that the inclusion is composed, on average, of lower atomic numbers elements than the stainless steel matrix surrounding it.

After initial examination in the as-received state, the casting was sectioned through the surface inclusion and the sectioned surface was prepared for examination by SEM and EDS. Inspection by SEI and BEI revealed a two-phase structure within the inclusion (Figure A-43 and Figure A-44) as well as a flake-like geometry – a thin plate of inclusion material floating on the surface of the casting. Closer scrutiny of the results (Figure A-45 and Figure A-46) unveiled the presence of both a low average atomic number dark phase and higher average atomic number light phase, designated by their relative backscatter electron intensities. Compositional analysis by EDS, shown in Figure A-47 and Figure A-48, indicates both phases contain titanium, silicon, aluminum and oxygen, along with minor additions of chromium and manganese. The light phase appears to be composed principally of titanium oxide while the “dark” phase is a mixture of mainly titanium oxide combined with substantial quantities of aluminum oxide and silicon oxide.

Along with the casting itself, samples of an iron-titanium alloying compound, in the form of millimeter-sized particles, were examined to determine if the alloying compound might be the source of the inclusion material. The alloying particles were mounted, ground and polished as required for examination by SEM. BEI examination (see Figure A-49) revealed that the particles were composed of a three phase structure: a low atomic number dark phase; a high atomic number light phase; and a third intermediate atomic number grey phase. As shown in Figure A-50, the dark phase of the iron-titanium alloying compound is composed of almost pure titanium with a very minor addition of aluminum. The chemistry of the light phase (Figure A-51) and the grey phase (Figure A-52) are similar to each other in that the both contain minor amount of iron and aluminum in addition to the major constituent of aluminum. The principle difference between them being that the light phase contains more iron relative to the dark phase which contains more aluminum. No oxygen was noted in the EDS data and no oxides were observed in the microstructure of the alloying compound.

The inclusion is basically a titanium-aluminum-silicon oxide. This fact, combined with the flake-like geometry of the inclusion and the lack of any oxides in the iron-titanium alloying compound, make it unlikely that the alloying compound itself is the direct source of the oxide inclusion. Due to titanium’s high affinity for oxygen, oxidation of the iron-titanium alloying compound during

addition to the melt is a possible source of the oxide inclusion. The source of the oxygen may be either excess oxygen in the melt due to inadequately killed steel or, possibly, atmospheric oxygen over the melt during iron-titanium alloying compound addition.



Figure A-39. Stainless Steel Investment Casting

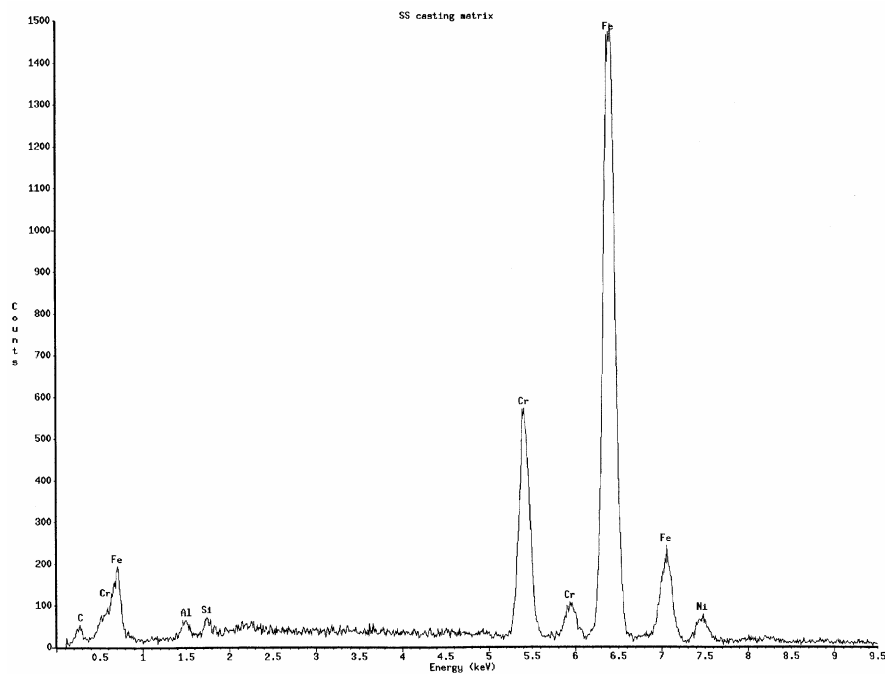


Figure A-40. EDS Compositional Data of Stainless Steel Casting Material

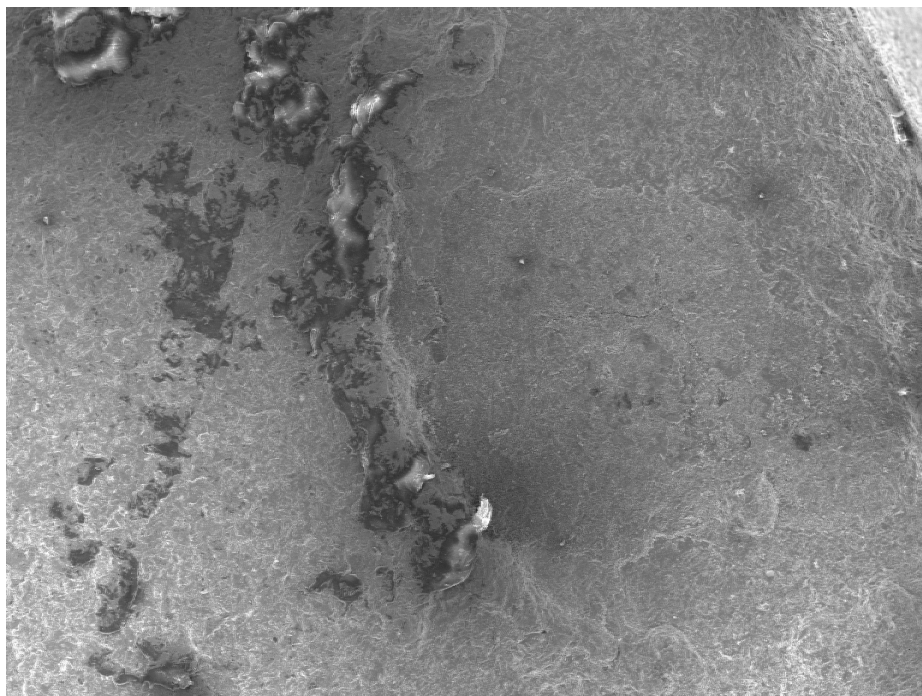


Figure A-41. SEI of Casting Inclusion, 30x

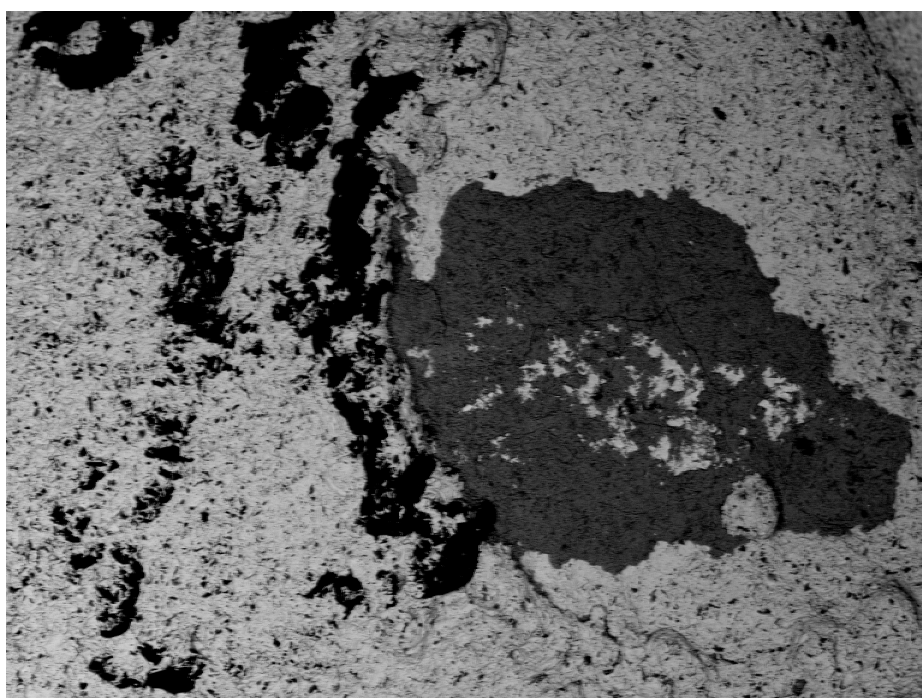


Figure A-42. BEI of Casting Inclusion, 30x

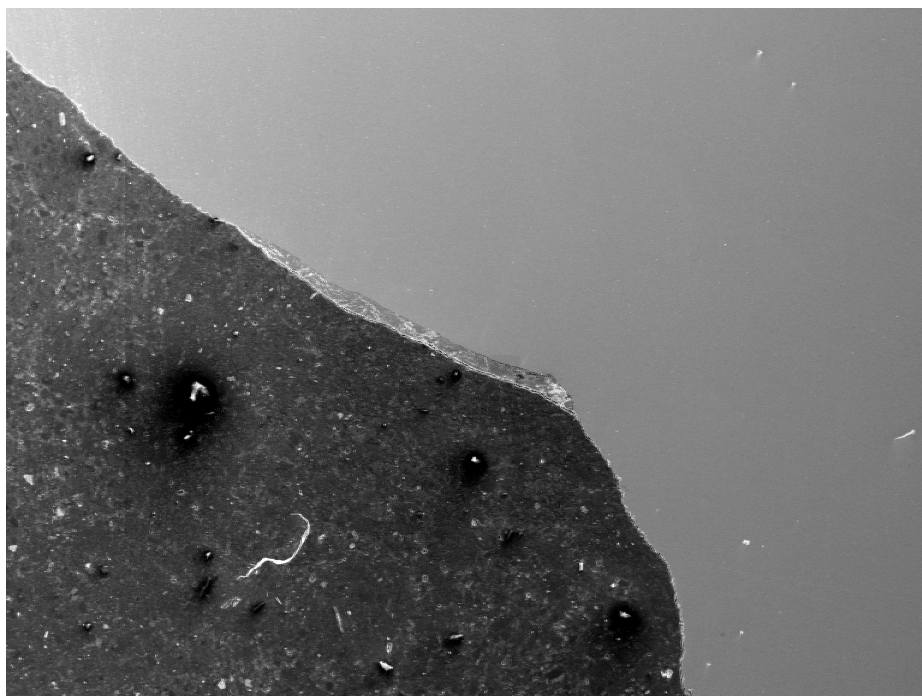


Figure A-43. SEI of the Sectioned Interface Between Casting (above) and Inclusion (below), 30x

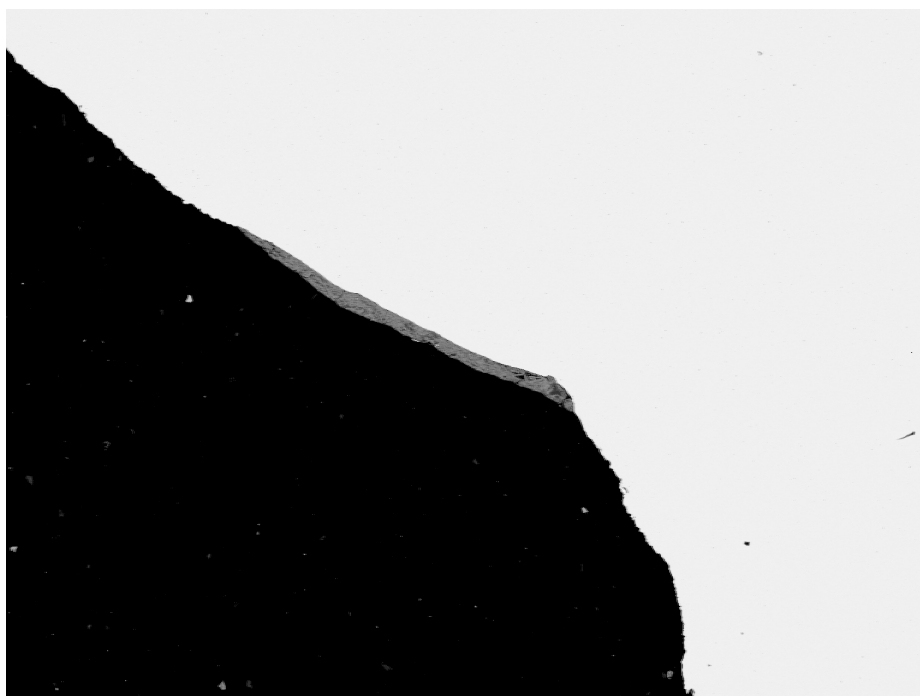


Figure A-44. BEI of the Sectioned Interface Between Casting (above) and Inclusion (below), 30x

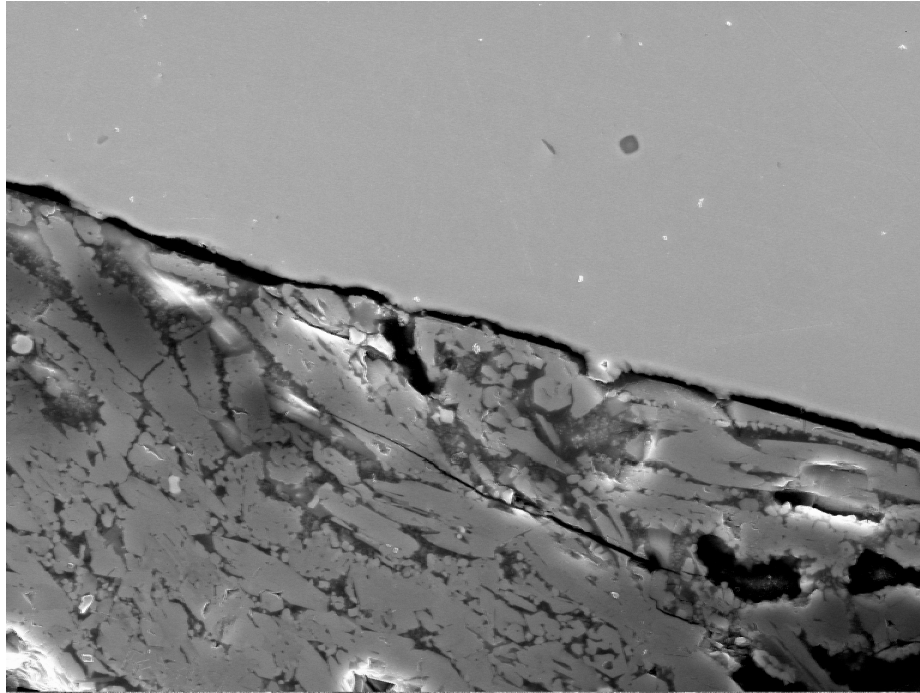


Figure A-45. SEI of Sectioned Casting Inclusion, 1000x

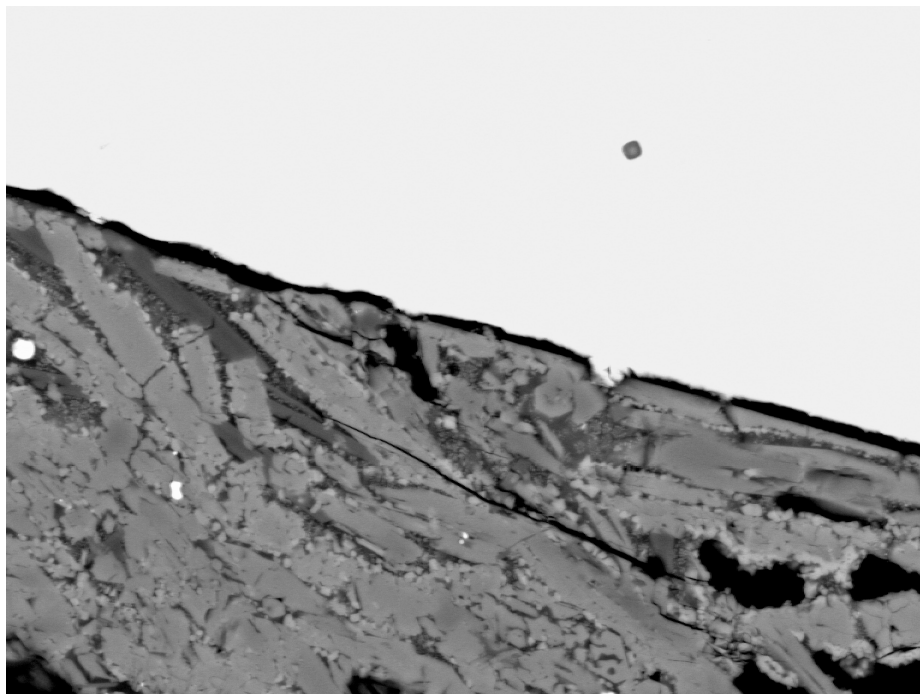


Figure A-46. BEI of Sectioned Casting Inclusion, 1000x

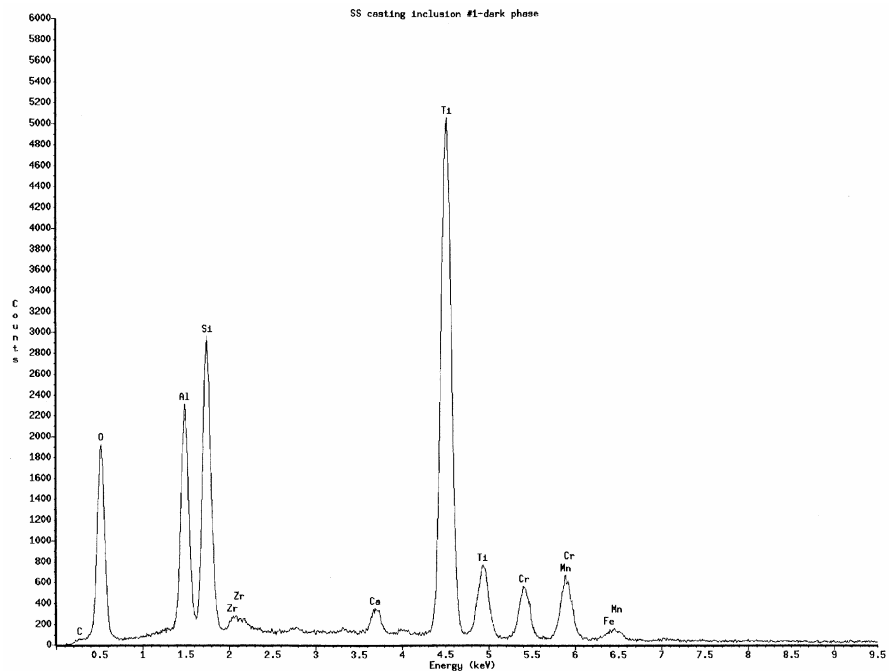


Figure A-47. EDS Compositional Data from the Dark Phase of the Sectioned Casting Inclusion

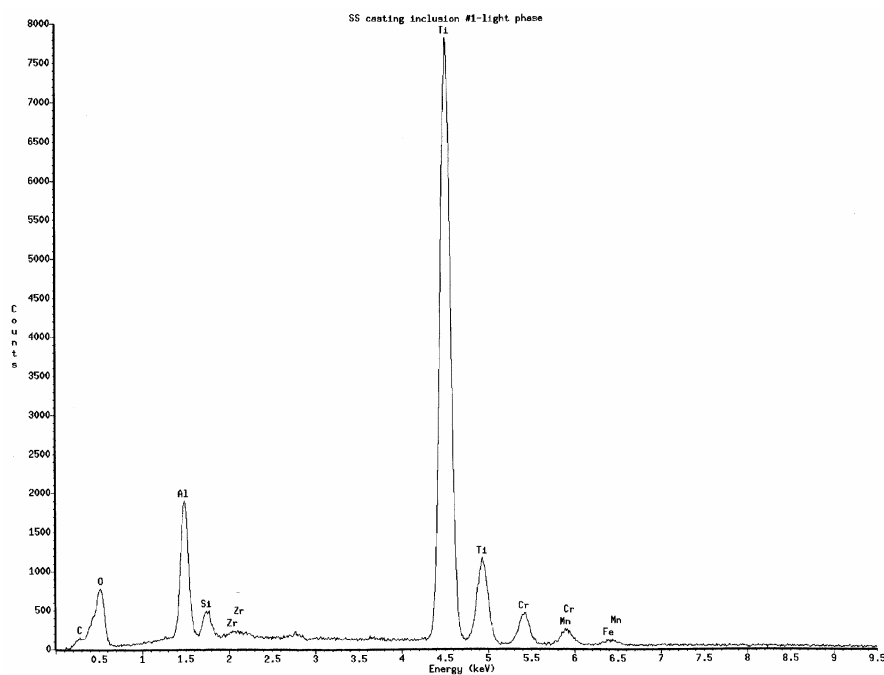


Figure A-48. EDS Compositional Data from the Light Phase of the Sectioned Casting Inclusion

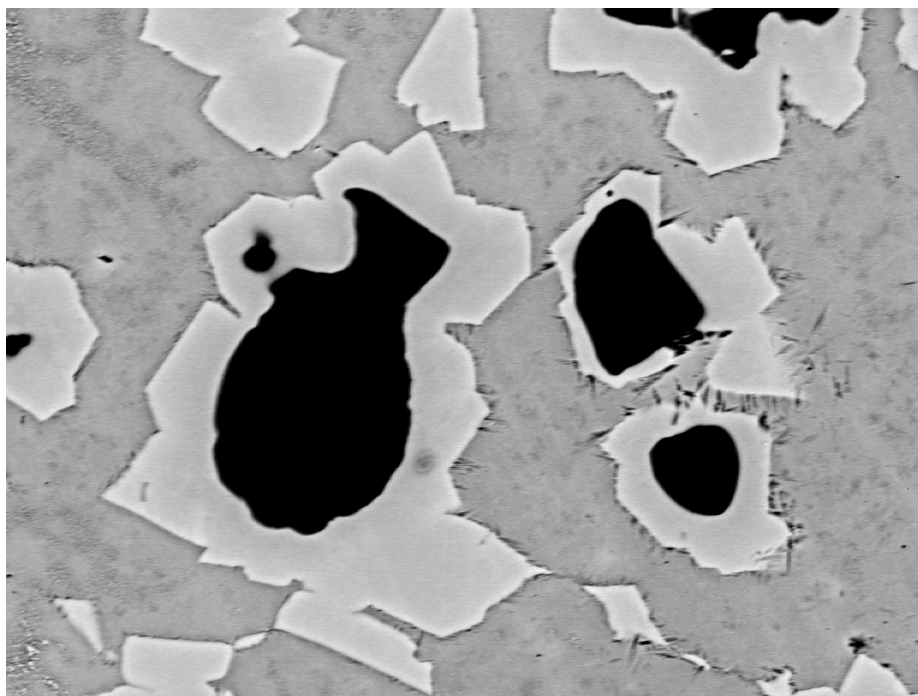


Figure A-49. BEI of FeTi Alloying Compound, 1000x

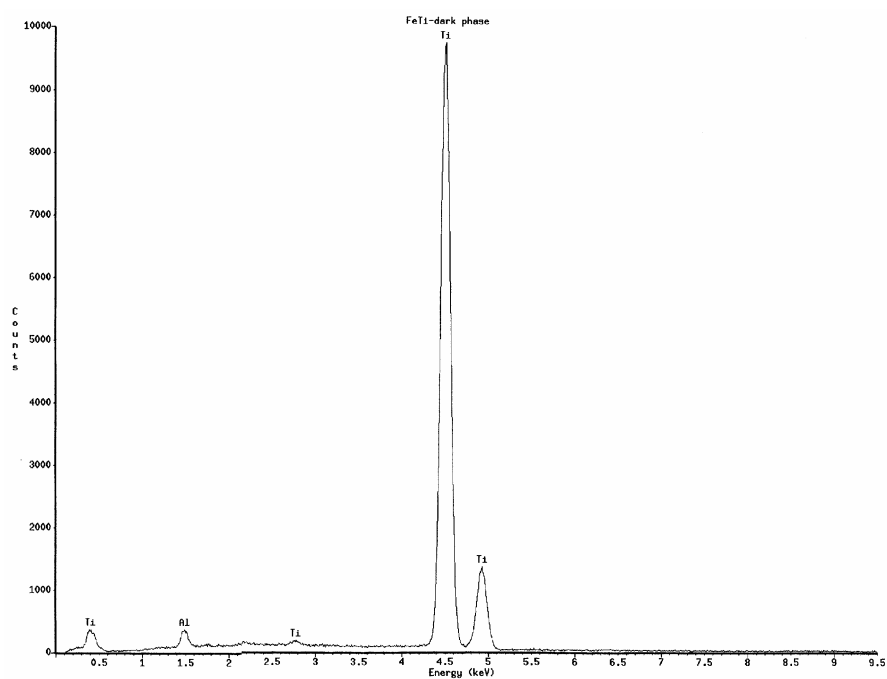


Figure A-50. EDS Compositional Data from the Dark Phase of the FeTi

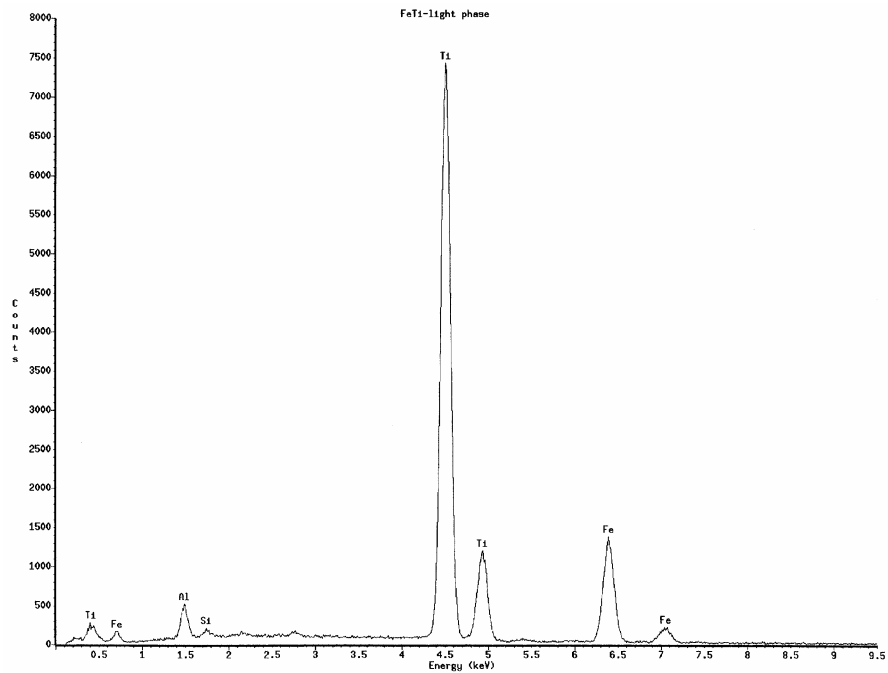


Figure A-51. EDS Compositional Data from the Light Phase of the FeTi

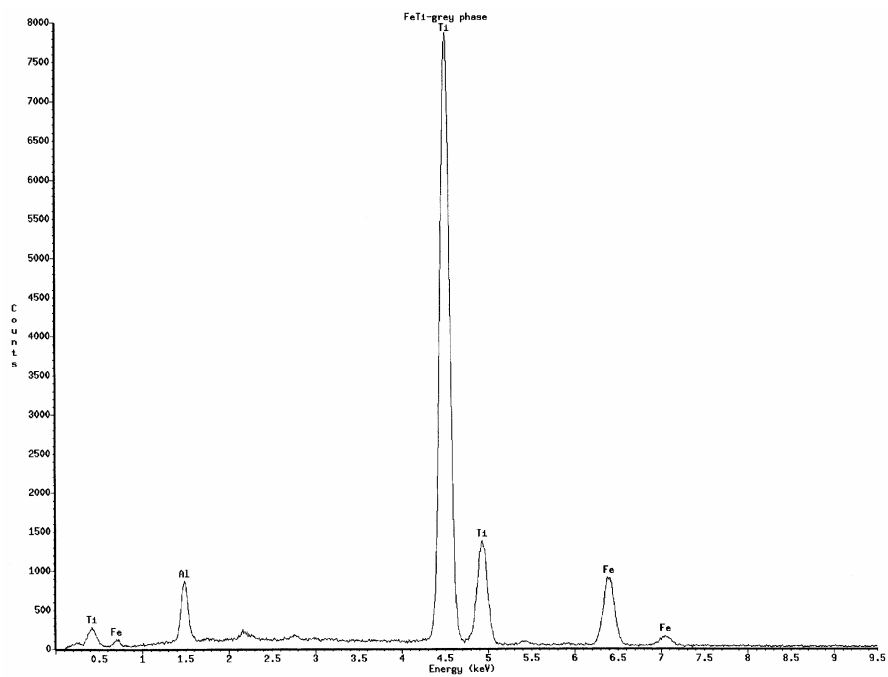


Figure A-52. EDS Compositional Data from the Grey phase of the FeTi

LIST OF ACRONYMS

ACRONYM	DESCRIPTION
2-D	Two-dimensional
3-D	Three-dimensional
AC	Alternating current
AFRL/MLLM	Air Force Research Laboratory, Materials and Manufacturing Directorate
Bcc	body-centered cubic
BEI	Backscattered electron imaging
Boeing	The Boeing Company
CA	Cellular automata
CRADA	Cooperative Research and Development Agreement
CTC	Concurrent Technologies Corporation
CTeC	Cooperative Technology Clusters
DB	Ductile-to-brittle
DoD	Department of Defense
DOE	Department of Energy
DR	Dynamic recovery
DRX	Dynamic recrystallization
DS	Directional solidification
ECAE	Equal channel angular extrusion
EDS	Energy dispersive spectroscopy
EMTEC	Edison Materials Technology Center
Fcc	Face-centered cubic
FEG TEM	Field emission gun transmission electron microscope
FEM	Finite element model (or modeling)

ACRONYM	DESCRIPTION
FSW	Friction stir welding
GE	General Electric
HIP	Hot isostatic press (or pressing)
HREM	High-resolution electron microscopy
HTC	Heat transfer coefficient
HTS	High-temperature superconductors
HVAPFSDS	High-Velocity, Armor-Piercing, Fin-Stabilized, Discarding-Sabot
INEEL	Idaho National Engineering and Environmental Laboratory
JMAK	Johnson and Mehl, Avrami and Kolmogorov
MAI	Metals Affordability Initiative
MC	Monte Carlo
MCF	Microstructural Characterization Facility
MPL	Materials Processing Laboratory
MTS	MTS Systems Corporation
OIM	Orientation imaging microscopy
PM	Powder metal
P&W	Pratt & Whitney
R&D	Research and development
Sc	Simple cubic
SEI	Scanning electron imaging
SEM	Scanning electron microscope
SS	Stainless steel
TEM	Transmission electron microscope
UDRI	University of Dayton Research Institute

ACRONYM	DESCRIPTION
UES	UES, Inc.
VIM	Vacuum induction melts (or melting)
WHA	Tungsten heavy alloy
WPAFB	Wright-Patterson Air Force Base
XRD	X-ray diffraction